Effect of Operating and Materials Parameters on Electrocaloric Device - A Simulation Study

MS (Research) Thesis

By
RABADIYA RIDHAMKUMAR ASHVINBHAI

DEPARTMENT OF MECHANICAL ENGINEERING
INDIAN INSTITUTE OF TECHNOLOGY INDORE
JUNE 2024

Effect of Operating and Materials Parameters on Electrocaloric Device - A Simulation Study

A THESIS

*Submitted in partial fulfilment of the
requirements for the award of the degree*
of
Master of Science (Research)

by
RABADIYA RIDHAMKUMAR ASHVINBHAI

DEPARTMENT OF MECHANICAL ENGINEERING
INDIAN INSTITUTE OF TECHNOLOGY INDORE
JUNE 2024

INDIAN INSTITUTE OF TECHNOLOGY INDORE

CANDIDATE'S DECLARATION

I hereby certify that the work which is being presented in the thesis entitled **Effect of Operating and Materials Parameters on Electrocaloric Device - A Simulation Study** in the partial fulfilment of the requirements for the award of the degree of **MASTER OF SCIENCE (RESEARCH)** and submitted in the **DEPARTMENT OF MECHANICAL ENGINEERING, Indian Institute of Technology Indore**, is an authentic record of my own work carried out during the time period from July 2022 to May 2024 under the supervision of Dr. Satyanarayan Patel, Associate Professor, Department of Mechanical Engineering, IIT Indore.

The matter presented in this thesis has not been submitted by me for the award of any other degree of this or any other institute.

10/05/2024

Signature of the student with date
(RABADIYA RIDHAMKUMAR ASHVINBHAI)

This is to certify that the above statement made by the candidate is correct to the best of my/our knowledge.

10/05/2024

Signature of the Supervisor of
MS (Research) thesis #1 (with date)
(Dr. Satyanarayan Patel)

RABADIYA RIDHAMKUMAR ASHVINBHAI has successfully given his MS (Research) Oral Examination held on **27th Jun 2024**.

Signature(s) of Supervisor(s) of MS (Research) thesis   Convener, DPGC
Date: 28/06/2024   Date: 28-06-2024

ACKNOWLEDGEMENTS

Dedicated to

My father

ABSTRACT

Our modern society increasingly relies on battery-driven products such as smartphones, tablets, computers, personal digital assistants (PDAs), iPods, solar modules, electric vehicles, etc. high temperatures impact the products, reliability and life span. In this direction, 55% of product failures are related to high-temperature operations. Hence, the present study discusses the electrocaloric (EC) as a viable device for battery cooling, considering variables like electric pulse waveform, electrode/substrate materials, and operating temperature. The analysis proceeds systematically to examine relevant parameters. Initially, modeling is conducted using the COMSOL Multiphysics software to explore the impact of various factors. Equation-based and built-in modeling estimate the electrocaloric effect (ECE). Initially, equation-based modeling analyzes the ECE and validates the model with the literature. The built-in electrocaloric module was unavailable in the COMSOL, but it was added in a later version. Thus, the inbuilt model is also discussed in detail.

The mesh-independent model is used to investigate the effect of different operating and material parameters on ECE. The electric pulse and holding time effect is analyzed on the EC cooling potential of polyvinylidene fluoride-trifluoro ethylene-chlorotrifluoroethylene terpolymer (P(VDF-TrFE-CFE). The square electric pulse provides maximum ECE because of the fast application of the electric field and keeping the same electric pulse; the holding time is varied, and it is found to depend on material thickness and material properties. The electric field square cycles with 0.3 second holding provide the maximum EC temperature change. The magnitude of the electric field also varied, and the maximum adiabatic temperature of (P(VDF-TrFE-CFE) was obtained at 5.41 K at 100 MV/m. It is found that types of electric pulse, magnitude, and holding time of electric pulse play a crucial role in obtaining maximum ECE at a given operating temperature. The effects of operating temperature, electrode, and substrate materials were also studied. The operating temperature is crucial since temperature changes substantially impact the performance of cooling systems. The simulation study also addresses the impact of electrode/substrate thickness and material on the ECE. Further, thermal contact resistance between various layers is considered, as it is vital to efficiently regulate heat flow between the electrode material and the device. Thermal contact resistance is considered based on data from experimental literature to analyze the ECE. The gold (0.1 μm thick) and aluminum (100

µm thick) are better electrode and substrate materials, respectively, at an optimal working temperature of 293.15 K.

Finally, a smartphone battery's surface (7 cm × 3 cm) is considered for cooling by the proposed EC device design. The same battery is also used to provide the necessary input voltage. The performance of an EC device is assessed by comparing the battery cooled by air, the battery and the EC device in contact (E=0, without ECE), and the battery and the EC device in contact cooling (E=100 MV/m, with ECE). The simulation study shows that the battery's surface/source temperature dropped from 313.15 K to ~298 K, ~297.5 K, and ~293.5 K when air cooling, the EC device in contact with the battery (no ECE, E=0) and EC device in contact with battery (with ECE, E =100 MV/m), respectively in ~6.5 seconds. The impact of the operating temperature source on the cooling process is also explored. The high-voltage application setup using the mobile battery is described thoroughly. The study shows that the battery cools quicker than air when using the ECE device. The proposed EC device design can provide new insight for mobile or other electronic cooling applications.

LIST OF PUBLICATIONS

Published Research Papers

1. **Ridhamkumar Rabadiya,** Nishchay Saurabh and Satyanarayan Patel, "Simulation Study on the Effect of Operating and Materials Parameters on Electrocaloric Device for Battery Cooling", Physica scripta, 99(4), 045915, 2024. https://doi.org/10.1088/1402-4896/ad2cd7

2. **Ridhamkumar Rabadiya**, Sai Eswar R.S, Surya Narayana Ch, Nishchay Saurabh, and Satyanarayan Patel, "P(VDF-TrFE-CFE) polymer Based Electrocaloric Device Design for Battery Cooling", Ferroelectrics, 618(1), 246-258, 2024. https://doi.org/10.1080/00150193.2023.2271330

TABLE OF CONTENTS

Chapter 1: Introduction

Chapter 2: Methodology & Modeling

Chapter 3: Effect of Electric Pulse and Holding time on Electrocaloric Potential

Chapter 4: Effect of Operating Temperature, Electrode, and Substrate Materials on Electrocaloric potential

Chapter 5: Battery Cooling by Electrocaloric Effect

Chapter 6: Conclusions and Future Outlook

LIST OF FIGURES

LIST OF TABLES

NOMENCLATURE

A	Surface Area	ΔS_{total}	Total Entropy Change
C_E	Heat Capacity Per Unit Volume Under Constant Electric Field	T	Temperature
C_p	Heat Capacity at Constant Pressure	ΔT	Temperature Change
c	Heat capacity	ΔT_{ad}	Adiabatic Temperature Change
D_i	Displacement Polarization	ΔT_{hys}	Temperature Loss Due to Hysteresis
E	Applied Electric Field	ΔT_{tc}	Temperature Drop Across The Thermal Contact
G	Gibbs Free Energy	t	Time
k	Thermal Conductivity	T_c	Curie Temperature
m	Mass	t_h	Holding Time
p	Pyroelectric Coefficient	t_r	Relaxation Time
P	Polarization	U	Internal Energy
P_a	Atmospheric Pressure	W	Work Done By The Outside
Q	Heat Absorbed From Outside	x	Thickness of The Material
Q	Heat Source or Heat Flux	ε_{ij}	Strain
Q_{ted}	Heat Generated due to Thermoelastic Damping	ρ	Density of An Electrocaloric Material
R	Material's Thermal Resistance	σ_{ij}	Stress
S	Entropy	τ_c	Cycle Period
ΔS	Entropy Change	τ_s	Viscous Heat Dissipation
$\Delta S_{dipolar}$	Dipolar Entropy Change	τ_{th}	Thermal Time Constant
$\Delta S_{lattice}$	Lattice Entropy Change		

ACRONYMS

AC	Alternating Current
BCE	Barocaloric Effect
CFD	Computational Fluid Dynamics
CNT	Carbon Nanotube
COP	Coefficient of Performance
DC	Direct Current
DPT	Diffuse Phase Transition
EC	Electrocaloric
ECE	Electrocaloric Effect
eCE	Elastocaloric Effect
EVs	Electric Vehicles
FE	Ferroelectric
HCFC	Hydrochlorofluorocarbons
LGD	Ginzburg-Landau-Devonshire
MCE	Magnetocaloric Effect
MD	Molecular Dynamics
MLCs	Multilayer Capacitors
P(VDF-TrFE)	Polyvinylidene Fluoride-Trifluoro Ethylene
P(VDF-TrFE-CFE)	Polyvinylidene Fluoride-Trifluoro Ethylene-Chlorotrifluoroethylene Terpolymer
PDMS	Polydimethylsiloxane
PE	Paraelectric
PET	Polyethylene Terephthalate
PVDF	Poly(Vinylidene-Difluoride)
VC	Vapor Compression

<div align="right">

Chapter 1
</div>

<div align="center">

Introduction
</div>

1.1 Introduction & motivation

Refrigeration serves multiple essential purposes across various sectors, making it a cornerstone of modern life. Firstly, preserving perishable food items by maintaining low temperatures is crucial, which slows down the growth of bacteria, yeast, and mold. This extends the shelf life of food, reducing waste and ensuring a steady food supply, particularly in urban areas where transportation and storage pose challenges. Secondly, refrigeration contributes significantly to food safety by preventing harmful microorganisms' growth, safeguarding public health, and ensuring consumers enjoy safe and nutritious food. Moreover, refrigeration facilitates the global distribution of food by allowing fresh produce and perishable goods to be transported over long distances from farms and food processing facilities to markets and consumers worldwide. This relies on a complex network of refrigerated transport, storage warehouses, and display units in retail establishments to maintain the quality and freshness of food products. In addition to its role in food preservation and distribution, refrigeration is essential for various industrial applications. It enables precise temperature control in pharmaceuticals, chemicals, and electronics industries, where maintaining specific conditions is critical for manufacturing and storage processes. Refrigeration systems cool equipment, control humidity, and create controlled environments necessary for ensuring product quality. Furthermore, refrigeration is crucial in comfort and climate control in residential, commercial, and institutional buildings. Air conditioning systems, based on refrigeration principles, regulate indoor temperatures and humidity levels, creating comfortable living and working environments.

Additionally, refrigeration preserves sensitive materials and equipment in museums, libraries, and research facilities, such as artwork, archives, and scientific specimens. Refrigeration is indispensable for preserving vaccines, medications, and biological samples in the medical and healthcare sectors. Cold storage ensures the efficacy and stability of pharmaceutical products, preventing degradation and maintaining potency. Refrigeration also supports critical medical procedures, such as organ transplantation and blood transfusions, by preserving donor organs and blood products. Overall, refrigeration plays a vital role across multiple domains, shaping the development of civilization and

improving quality of life. Cooling has significantly affected total energy uses, including residential (air conditioning and refrigeration), electronic, industrial process cooling, storage, and transportation of perishable items, food, and medication. The escalating concerns of environmental pollution and global warming are compounded by the rising demand for energy, leading to the depletion of fossil fuels. Vapor compression has long dominated cooling technology due to its high efficiency, compact size, and reliability. Hence, the effectiveness of vapor compression has hindered the development of alternative technologies. New refrigeration techniques are being developed to enhance the benefits of artificial cooling while simultaneously addressing the adverse effects on the environment [20, 21].

In the realm of modern electronics, effective heat management is crucial. Our modern society increasingly relies on battery-driven products such as smartphones, tablets, computers, personal digital assistants (PDAs), iPods, solar modules, electric vehicles, etc. high temperatures impact the products' reliability and life span. In this direction, 55% of product failures are related to high-temperature operations [22]. The inadequate thermal management, heat generation, and rise in temperature cause the failure of vital components and performance degradation [23]. The cooling of these systems has gotten more difficult as the amount of physical area available for thermal management is small [24]. Recent breakthroughs in electronics have enabled the creation of smaller, more efficient communication devices and computers. These devices are highly portable and rely on onboard energy sources like batteries or fuel cells.

However, the challenge lies in efficiently dissipating the heat generated by these compact systems. When multiple components are crammed into a confined space, heat can build up quickly, surpassing the system's ability to dissipate it. This accumulation of thermal energy can lead to overheating and physical damage to the components. To address this challenge, suitable refrigeration systems are needed to regulate temperatures efficiently and ensure electronic devices' optimal performance and longevity. A traditional cooling system such as vapor-compression (VC) cooling technology is noisy, needs coolants that release hazardous greenhouse gases and is difficult to scale down to satisfy the cooling requirements of small electronics such as mobile, wearable and flexible electronics [23]. Environmental concerns regarding using HCFC chemicals in vapor-compression refrigeration have led to significant investment and interest in developing alternative cooling technologies[25].

Liquids and solids are ideal for innovative refrigeration techniques due to their high energy density and lack of hazardous gas emissions[21]. The uses of solid materials as refrigerants have recently gained popularity. Solid refrigerants have larger mass and energy densities, which can lead to increased heat extraction. Solid-state refrigeration has static operation, restricted movement, high repeatability, and little maintenance, making it a cost-effective and environmentally friendly alternative to traditional vapor compression systems[26, 27]. Research suggests that ferroic materials with first or second-order entropy transitions are ideal for such uses. These materials can experience significant temperature changes when exposed to an adiabatic stimulus. This process, known as the solid-state caloric effect, has been extensively studied and reported for space cooling applications. When refrigerated, these caloric effects can achieve up to 60% of Carnot's efficiency at the same operating temperatures, more than even the most efficient vapor compression systems can achieve[21, 26, 27]. Solid-state cooling systems are more contemporary alternatives to compressors and traditional liquid or vapor refrigerants, whose increasing use, inappropriate handling, and disposal have significantly contributed to global warming[8]. The demand for innovative cooling technologies is fuelled by the above factors, such as size-adapted and portable cooling systems (electronics, batteries)[8].

1.2 Solid state cooling

Solid-state cooling is one of the alternatives that overcome the shortcomings of VC cooling technology [28]. Compared to vapor compression technology and other conventional methods employed for the bulk of cooling, solid-state cooling has the advantage of minimal moving parts, low noise performance, and the absence of refrigerant [29]. Solid-state cooling systems based on caloric effects are becoming increasingly popular. These calorific effects primarily consist of magnetocaloric, electrocaloric, barocaloric, and electrocaloric effects (ECE) [30]. They refer to the change in isothermal entropy or adiabatic temperature caused by applying or removing a magnetic field, an electric field, hydrostatic pressure, and uniaxial stress, respectively[30]. Gough discovered the caloric effect in natural rubber, which Joule examined further [30]. Solid-state cooling systems are more contemporary options that eliminate the need for compressors and conventional liquid or vapor refrigerants[30]. Thermoelectric coolers are widely studied for electronic cooling[31]. Despite years of research, the low efficiency of these coolers has been a significant source of concern.

Further, magnetocaloric coolers require a large magnetic field to induce material entropy changes, which limits their miniaturization[32]. The current generation's cooling process is relatively small, and the energy consumption needs to be improved due to material insulation. The external fields can be mechanical, magnetic, or electric to produce the cooling, correspondingly known as mechanocaloric [33], magnetocaloric [34], and electrocaloric (EC)[35]. Strong magnetic fields and mechanical load are needed to cool by magnetocaloric and elastocaloric, which restricts their miniaturization [32]. Magnetocaloric refrigerators rely on expensive superconducting magnets or heavy permanent magnet arrays to generate strong magnetic fields, limiting their global market viability[36]. Magnetocaloric materials, which consist of rare-earth and transitional metals, including Gadolinium (Gd), Lanthanum (La), and Rhodium (Rh), are more expensive[37]. MCE (Magnetocaloric effect) and ECE are more promising for producing considerable cooling power than eCE (Elastocaloric effect) and BCE (Barocaloric effect), which rely on mechanical triggers and operate at lower frequencies[38]. This is due to their ability to switch between magnetic and electric fields at high frequencies[38]. The comparison between the solid-state cooling methods and the vapor compression cooling is discussed in Table 1.1. As described in Table 1.1, vapor compression refrigeration technology has medium cooling power density having a cop in the medium range and is currently used in commercial applications.

Table 1.1. comparison between different refrigeration methods.[36-38]

Technology	Cooling power Density	COP	Scalability	Current state
VC Refrigeration	Medium	Medium	Low	Commercial(developed)
Elastocaloric	Low	High	Low	Prototype
Barocaloric	Low	High	Low	Prototype
Thermoelectric	High	Low	High	Commercial
Magnetocaloric	Medium	High	Low	Prototype
Electrocaloric	High	High	High	prototype

Other solid-state cooling technologies such as electrocaloric, barocaloric, magnetocaloric, and elastocaloric are currently in prototype state but are comparable with conventional cooling technology. The electrocaloric cooling technology has the highest cooling power density, COP, and scalability compared to other cooling technologies. The comparison of

existing technology based on its efficiency is discussed in Table 1.2. In Table 1.2, electrocaloric cooling technology is compared with the other existing technologies.

Table 1.2. Energy conversion efficiency of various cooling technologies[39, 40]

Novel or existing technology	Efficiency	Comments
Electrocaloric cooler/Pyroelectric power generator	60 - 70	Small effects in bulk materials and large effects in thin films
Thermoelectric cooler or power generator	10	More than 60 years of extensive research has not yet delivered a practical and efficient device
Conventional fridge (VC cycle)	40 - 50	Everything is optimized, and there is no growth in this market
Magnetocaloric cooler	60 - 70	Requires large magnetic field and, therefore, large magnets

Electrocaloric cooling technology has a small effect on bulk materials but a large effect on thin films, with an efficiency of 60 – 70. On the other hand, vapor compression refrigeration technology and thermoelectric coolers have an efficiency of 40 -50 and 10, respectively. Magnetocaloric coolers require a large magnetic field, necessitating using more giant magnets. Regarding ease of use and energy efficiency, ECE surpasses MCE by far because it is much simpler to apply an electrical field to dielectric and ECE materials[38]. A strong magnetic field can be challenging, especially with limited device size.

However, the electric field for ECE is not restricted[41]. ECE offers a highly efficient cooling solution for many applications, including on-chip cooling and temperature regulators[38]. ECE-based refrigeration is an environmentally beneficial alternative to traditional vapor-compression methods. Electrocaloric materials in cooling devices can provide high cooling power, energy efficiency, and a wide temperature range[42]. The ECE allows for the development of small refrigerators, electronics cooling, temperature regulations for sensors, on-chip cooling and medical specimens, with high efficiency [43, 44]. Unlike magnetocaloric materials, electrocaloric thin films can exhibit a strong ECE with lower voltages, making them a viable option for low-cost operating devices[21]. As

a result, EC cooling is more efficient and ecologically benign than other solid-state cooling technologies. It has a promising future for use in controlling the temperature of microelectronic devices[45]. Furthermore, what electrocaloric cooling is and how it works are explored in detail.

1.3 Electrocaloric working principle and cycle

The ECE is a reversible temperature change under adiabatic conditions or isothermal change in entropy when an electric field is applied or removed from a dielectric medium, as shown in Figure 1.1. In processes A–B, when the electric field is applied adiabatically, the dipoles get aligned and EC material comes to the state of least entropy; as a result, temperature increases.
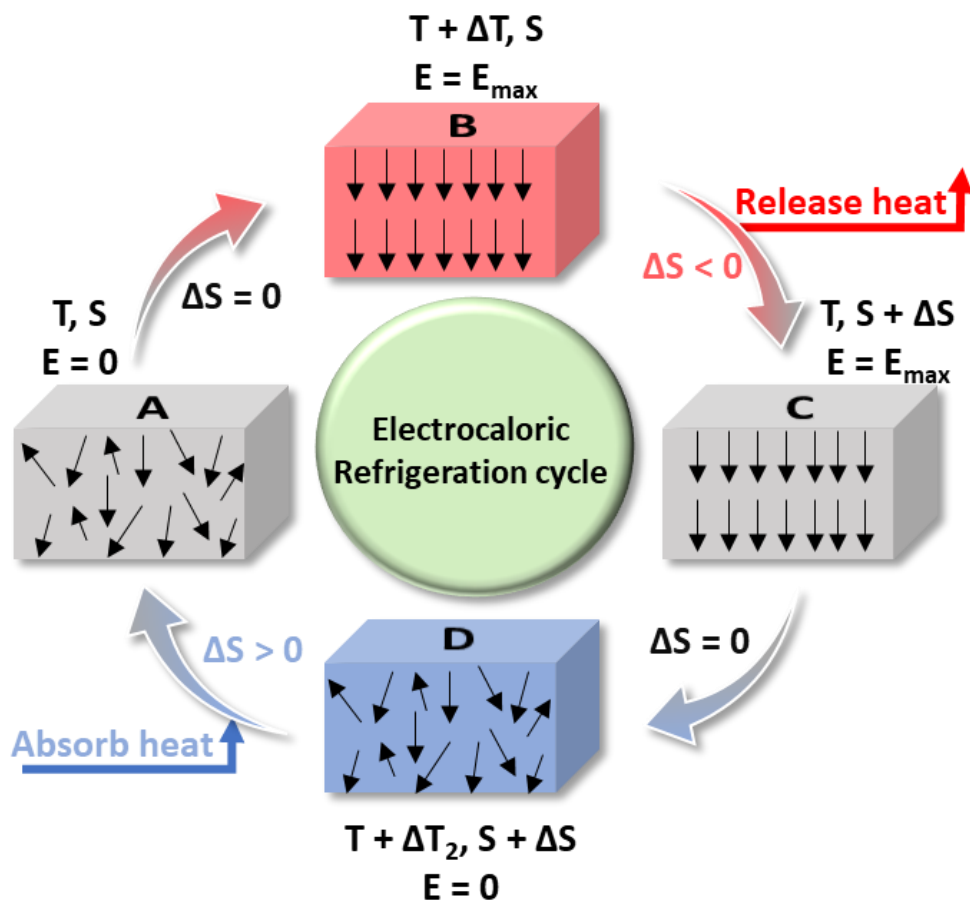
Figure 1.1. Schematic diagram showing the working of EC material upon application of the electric field.

When an EC material is left on hold at a constant electric field under the same conditions, the dipolar entropy does not change. The generated heat is released to the surroundings through B–C. Under adiabatic conditions, when the electric field is withdrawn (E = 0),

the dipolar entropy increases, the lattice entropy lowers, and the EC material temperature decreases below the initial temperature process C–D. The EC material can absorb heat process D–A and return to its initial temperature if held for some time ($E = 0$). In this way, the EC cycle is completed and repeated, as shown in Figure 1.1.

Here, it is essential to note that various thermodynamic cycles, such as Carnot, Ericsson, Stirling, Brayton, etc., can be used for electrocaloric cooling[46]. Although the efficiency of the Carnot cycle is higher, the application of an electric field at adiabatic conditions (Brayton cycle) is more practical than the isothermal process (Carnot cycle) [47]. In this direction, Schwartz *et al*. [47] have done a detailed analysis of various electrocaloric cooling cycles and suggest that the Brayton cycle is more suitable from a practical application point of view. Hence, the present work considers the Brayton cycle for the simulation. Applying an adiabatically electric field to a material causes a significant change in its entropy, known as the electrocaloric effect. Based on Maxwell's relation for entropy change in ferroic materials, such estimations can be measured. Maxwell's relation describes how entropy changes in a substance when temperature changes[48].

$$\left(\frac{\partial D_i}{\partial T}\right)_{\sigma,E} = \left(\frac{\partial S}{\partial E_i}\right)_{T,\sigma} = p_i^{\sigma,E} = p_i^{T,\sigma} \tag{1.1}$$

The equations (1.1) show the derivation process using the set of independent variables (T, σ_{ij}, and E_i) to describe the adiabatic temperature changing; the other set of independent variables (S, σ_{ij} (or ε_{ij}) and E_i) can also be used. The heat capacity of dielectric material, C_E (per unit volume under constant electric field), can be calculated by $C_E = T(\partial S/\partial T)$ (detailed procedure is ignored). However, the corresponding Maxwell relation under constant stress or strain is expressed as,

$$-\left(\frac{\partial T}{\partial E_i}\right)_S = \left(\frac{\partial D_i}{\partial S}\right)_E = \left(\frac{\partial D_i}{\partial T} \cdot \frac{\partial T}{\partial S}\right)_E = \left(\frac{\partial D_i}{\partial T}\right)_E \cdot \frac{T}{C_E} = \frac{T p_i^E}{C_E} \tag{1.2}$$

Under stress-free conditions, the isothermal entropy (ΔS) varies when the differential form is transformed into the integral form during a quasi-static process[43, 49].

$$\Delta S = \int_{E_1}^{E_2} \left(\frac{\partial D_i}{\partial T}\right)_E dE_i \tag{1.3}$$

The adiabatic temperature change (ΔT_{ad}) in stress-free conditions can be calculated using an applied electric field E_i and displacement polarization D_i[45],

$$\Delta T_{ad} = -\int_{E_1}^{E_2} \frac{T}{C_E(T)} \left(\frac{\partial D_i}{\partial T}\right)_E dE_i \tag{1.4}$$

The electric displacement can be defined as $D_i = \varepsilon_0 E_i + P_i$, where ε_0 is the permittivity of the vacuum. $\varepsilon_0 E_i$ is temperature independent; hence $\partial D_i/\partial T \cong \partial P_i/\partial T$. Equation (1.4) gives that temperature change in EC materials results from entropy change and is directly connected to displacement under given electric fields [50]. Equation (1.4) rewritten as:

$$\Delta T_{ad} = -\int_{E_1}^{E_2} \frac{T}{C_E(T)} \left(\frac{\partial P_i}{\partial T}\right)_E dE_i \tag{1.5}$$

Equation (1.5) clarifies that a material needs to have a high pyroelectric constant $(\frac{\partial P_i}{\partial T})$ throughout a broad range of temperature and electric field values to exhibit a significant EC impact.

Electrocaloric materials can create more efficient and environmentally friendly refrigeration and air conditioning systems than traditional vapor-compression methods. They offer the potential for quieter operation, reduced energy consumption, and eliminating environmentally harmful refrigerants. With the increasing miniaturization and power density of electronic devices, efficient cooling becomes crucial to maintain optimal performance and reliability. Electrocaloric cooling can provide compact and efficient cooling solutions for microelectronics, such as computer chips and LED lighting. Aerospace applications often require lightweight and efficient thermal management systems. Electrocaloric cooling can be integrated into spacecraft, satellites, and other aerospace equipment to regulate temperatures, dissipate heat, and maintain optimal operating conditions. Electrocaloric cooling systems could find application in automotive climate control systems, providing efficient cooling for electric vehicles (EVs) or hybrid vehicles while reducing energy consumption and greenhouse gas emissions associated with traditional air conditioning systems. Moreover, numerous materials have been examined to discover the best material for the ECE and see which one had the maximum ECE.

1.4 Electrocaloric materials

To comprehend the caloric effects of ferroelectric materials, it's essential to evaluate their functional hierarchy and characteristics. Ferroelectric materials are a sub-class of pyroelectric materials, a subset of piezoelectric materials, as shown in Figure 1.2. They are all functional dielectrics. Except for ferroelectric polymers, all materials are crystalline ceramics with high polarity. Dielectric materials with high band gaps act as

electrical insulators around room temperature. Hopping conduction may occur in highly doped ceramics or those containing mobile elements like lithium, sodium, and potassium. Exceptions can be overlooked for a more general approach that applies to a broader range of materials. All dielectric materials contain polarizable species, contributing to their high dielectric constant. Non-centrosymmetric lattices in materials provide electrical functionality. Eleven of thirty-two crystal classes lack electronic functioning due to their centrosymmetric structure. Twenty out of the remaining 21 symmetries can display direct piezoelectricity. Ten piezoelectric point groups exhibit spontaneous polarization without an electric field, resulting in pyroelectricity. Only a few pyroelectric crystals exhibit reversible polarization and are classed accordingly. Ferroelectricity is a substance that exhibits spontaneous polarization and is reversible when exposed to external electric fields [51]. The feature was first found in Rochelle salt and is termed by its resemblance to ferromagnetism, a magnetic property of materials with a permanent magnetic moment [52, 53]. Dielectric polarization occurs when an external electric field polarizes a material and the induced polarization (P) is proportional to the magnitude of the applied field (E). Ferroelectric materials are in a paraelectric condition above the Curie temperature T_C. Here, there is a nonlinear polarization in an external electric field. The slope of the polarization curve determines electric permittivity, which is not constant. The ferroelectric state has nonlinearity and spontaneous nonzero polarization due to the zero applied field. The hysteresis loop exists because spontaneous polarization can be reversed by a strong electric field, making it dependent on both the current electric field and its history. Variations in a ferroelectric material's crystal lattice can affect the strength of its electric dipoles, leading to spontaneous polarization. When a ferroelectric material is turned into a capacitor without introducing an external field, the change in spontaneous polarization results in a change in the surface charge, generating current flow. Ferroelectric materials can modify their lattice structure through two stimuli: mechanical force and temperature.

Figure 1.2 depicts the relationship among the ferroelectric, pyroelectric, piezoelectric, and dielectric materials. This relationship implies that ferroelectric materials have the highest piezoelectric performance compared to non-ferroelectric materials. Piezoelectricity refers to the generation of surface charge caused by external stress, while pyroelectricity refers to the change in spontaneous polarization due to temperature changes. The response is known as pyroelectricity because of the temperature-dependent nature of this

polarization. Pyroelectric materials are those with a 10-point symmetry and spontaneous polarization. Spontaneous polarization causes materials to produce surface charges along the bulk polar vector, maintaining electrical neutrality. Thermal flux affects the strength of bulk polar vectors, causing surface charges to rearrange and a transitory electric potential to arise across surfaces. This electrical potential can generate a signal when connected to an external circuit. This is known as the pyroelectric effect, and the materials are identified as pyroelectric materials. Different mechanisms can be used to generate pyroelectricity. For example, ceramics contain ionically bonded species, and polarization can result from the crystal structure.
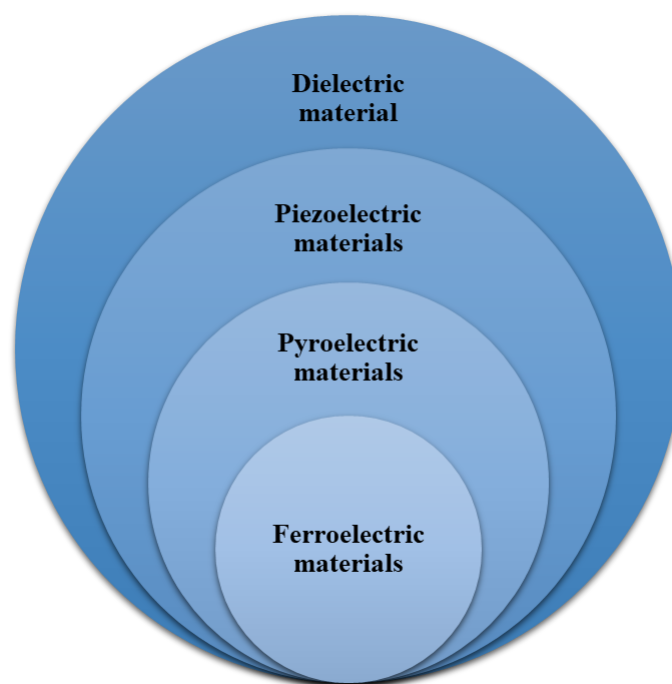
Figure 1.2. Interrelationship among ferroelectric, pyroelectric, piezoelectric, and dielectric materials[1].

Similarly, the alignment of polarized covalent bonds can yield the same effect for crystalline polymers with aligned molecular chains. Pyroelectric behavior is an external phenomenon that is best understood by examining the changes produced in surface charges. See Figure 1.3 for an example of how thermal excitation disrupts the no centrosymmetric structure of a heated (dT/dt >0) pyroelectric material, resulting in a loss of bulk polar vector intensity. Temperature-dependent polarization and pyroelectric coefficient changes are seen for first-order phase transition, second-order phase transition, and relaxor materials.
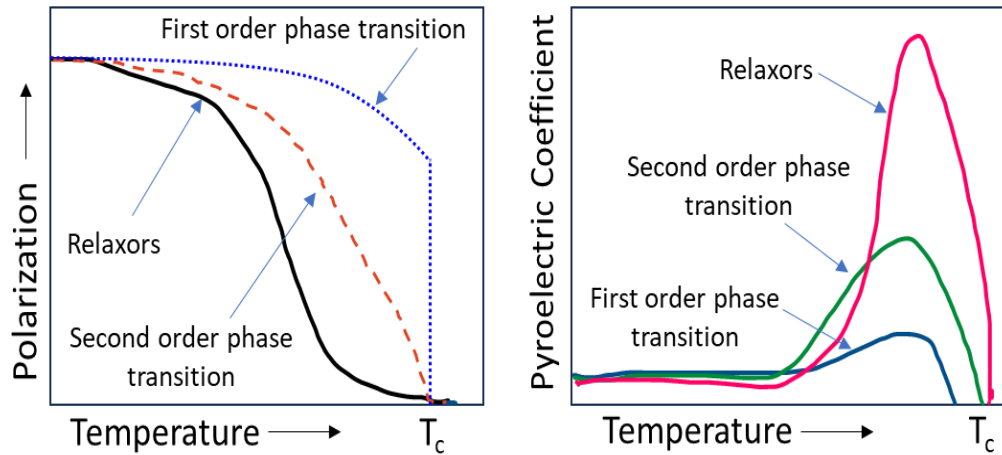
Figure 1.3. Schematic diagram of temperature dependence (a) polarization, (b) pyroelectric coefficient for first-order phase transition, second-order phase transition, and relaxors material[2].

The pyroelectric coefficient varies depending on phase transitions. Relaxor-based materials could be suitable for pyroelectric applications. Loss of spontaneous polarization affects free charges on material surfaces. Open circuit conditions cause an electrical imbalance, producing an electric potential across the material. Short circuit conditions cause an electric current to pass between the material's two polar surfaces, resulting in charge neutrality. Cooling the pyroelectric material (dT/dt <0) causes dipoles to reorient, increasing spontaneous polarization and reversing electric current flow under short circuit circumstances. Free charges are attracted to the polar surfaces. Ferroelectric materials are a subgroup of the pyroelectric group that exhibit spontaneous polarization. A ferroelectric material exhibits similar polarization to a pyroelectric one. Ferroelectric polarization, reversible with an external electric field, differs from the other polarizations. Ferroelectricity is characterized as spontaneous polarization that can be reversed by an external electric field [54].

Relaxor ferroelectrics feature nano-domains, frequency-dependent dielectric response, and diffuse phase transition (DPT). Nano-domains lack long-range dipolar interactions, inhibiting the creation of ferroelectric domains. Relaxor ferroelectrics with DPT exhibit a large transition peak from non-centrosymmetric to centrosymmetric structures, as illustrated in Figures 1.4 (a) and (b). Traditional ferroelectrics, on the other hand, exhibit a prominent transition peak at T_c. This enables fascinating traits to develop. The absence of long-range dipolar order and domains results in insignificant properties. Figures 1.4 (c)

and (d) demonstrate the polarization-electric field (P-E) hysteresis behavior of ferroelectric and relaxor ferroelectrics. Relaxor ferroelectrics are commonly referred to as dipolar glasses. DPT permits relaxors to operate throughout a wide temperature range, improving dielectric constant and temperature invariant performance.
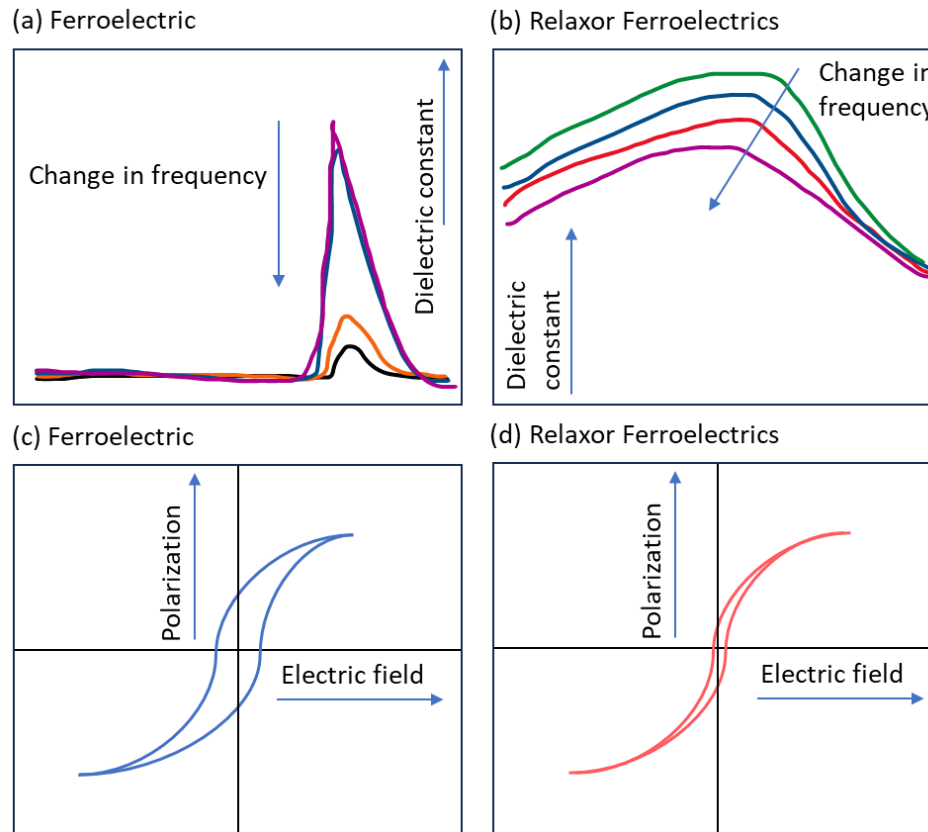
Figure 1.4. Frequency dependence of dielectric response for (a) ferroelectric[3] (b) relaxor ferroelectric[3], and polarization-electric field (P-E) hysteresis behavior of (c) ferroelectric[4] and (d) relaxor ferroelectrics[4].

Relaxor ferroelectrics are usually considered ideal for solid-state refrigeration. Due to significant polarization changes, traditional ferroelectric materials have a peak adiabatic temperature shift at the ferroelectric-paraelectric transition (Curie temperature). Figures 1.5(a) and (b) depict temperature-entropy (T-S) diagrams for electrocaloric materials undergoing first and second-order phase transitions, respectively. During the first-order ferroelectric to paraelectric phase transition, the electrocaloric material's entropy increases around its Curie temperature, resulting in a higher electrocaloric effect than the second-order phase transition. To achieve high ΔT and ΔS, electrocaloric materials must have a significant gradient of polarization change $(\partial P/\partial T)_E$ over their operating temperature range. However, deviation from the transition temperature causes a quick decrease in EC

and heat extraction capacity. However, deviation from the transition temperature causes a quick reduction in EC and heat extraction capacity. This restricts the use of such materials to a limited temperature range[35, 55]. Relaxor ferroelectrics could provide a solution to this challenge. Unlike normal ferroelectric materials, Relaxor ferroelectrics exhibit diffuse phase transitions across a wide temperature range. As a result, these materials would give temperature-invariant performance over a large temperature range of operation[35].
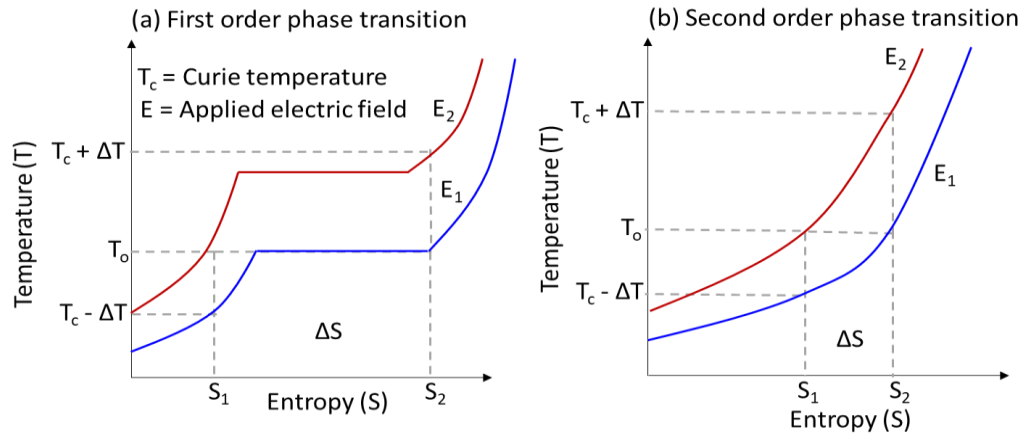
Figure 1.5. The temperature-entropy (T-S) diagram for electrocaloric materials with first and second-order ferroelectric-paraelectric phase transitions. Redrawn from Ref[5]

Since ferroelectric materials have the highest performances in terms of piezoelectric and pyroelectric properties and have very interesting ECE, they can be used in refrigeration applications. Electrocaloric refrigeration is a promising environmentally friendly cooling technique that does not emit gasses into the atmosphere[38]. The material must undergo a significant entropy change due to polarization to achieve a significant ECE. Furthermore, the dielectric material should be capable of producing substantial polarization changes that can be made effectively by an external field. The ECE has been studied since 1930 when it was measured in Rochelle salt and found to be minimal[56]. However, it was in the 1960s that significant research into electrocaloric materials was conducted.

However, the modest ECE recorded in the last half-century of the 20th century, with an adiabatic temperature change ΔT of less than 2°C, makes it unsuitable for practical uses[57]. The maximum adiabatic temperature change (ΔT_{ad}) of EC materials is obtained near the Curie temperature (T_c) in ferroelectric materials, where the ferroelectric (FE)-paraelectric (PE) phase transition occurs[58]. In 2006, Mischenko *et al.*[45] reported a giant ECE in ceramic thin films with a ΔT of 12 K at 499 K, and Neese *et al.*[50]

discovered a giant ECE near room temperature in a class of ferroelectric polymer with a large ΔT (>12 K) and isothermal entropy change ΔS (>50 Jkg^{-1}K^{-1}). The ECE is a reversible change in the temperature of a material caused by a changing electrical field. It has been known for over a century but gained little attention until the discovery of the so-called giant ECE in 2006 [59]. Electrocaloric materials with large ECE are promising to realize compact cooling devices for next-generation refrigeration, temperature regulation and air-conditioning, with high efficiency and environmental friendliness[41]. Economic sustainability and environmental impact should be considered in addition to fundamental factors like ECE and efficiency when evaluating a material's suitability as an electrocaloric refrigerant[46].

Thin films, ceramics, and multilayer capacitors based on PZT or Pb(Mg,Nb)O$_3$ (PMN) have demonstrated exceptional electrocaloric performance, with a higher coefficient of performance, and a maximum ΔT within the 1-8 K range[45, 60]. Most electrocaloric materials have been processed using traditional solid-state reactions (ceramics) or sol-gel or tap casting methods for thin films and polymers[41]. There are certain materials available that show the ECE, like ceramics, thin and thick films, etc. These can be discussed further to determine which material is best and gives high ECE. Table 1.3 lists ECE parameters for BaTiO$_3$-based ceramics and thick films as described in the literature.

Table 1.3. Comparison of observed electrocaloric parameters with the reported literature

Material	Material type	thin/bulk/thick	Operating temperature (K)	Voltage (MV/m)	ΔT_{ad} (K)	Ref.
SrTiO$_3$	Ceramic	Thin	17	0.8	0.06	[61]
PbZr$_{0.52}$Ti$_{0.48}$O$_3$	Ceramic	Thin	660	57.7	11.1	[62]
0.9PMN-0.1Pt	Ceramics	-	323	2.91	0.55	[63]
PZT-5	Ceramic	Thick	298.15	1.8	0.28	[64]
Ba(Zr$_{0.05}$Ti$_{0.95}$)O$_3$	Ceramic	-	386	30	2.4	[65]
PbZr$_{0.455}$Sn$_{0.455}$Ti$_{0.09}$O$_3$	Ceramics	Thin	317-328	3	1.4	[66]
PbZr$_{0.75}$Sn$_{0.20}$Ti$_{0.05}$O$_3$	Ceramics	-	434	3	2.6	[67]
PMN	Ceramics	-	289-340	9	2.5	[68]
PZT-5	Ceramic	Thick	298.15	2.8	0.15	[64]
P(VDF-TrFE) (68/32)	Polymer	Thin	343	50	2	[69]
BaTiO$_3$	Ceramic	Thick	-	2.8	0.4	[70]

$Na_{0.5}Bi_{0.5}TiO_3$	Ceramics	-	413	5	0.33	[71]
P(VDF-TrFE) 55/45 mol %	Polymer	Thin	340.15	120	12	[72]
P(VDF–TrFE–CFE) 56.2/36.3/7.6 annealed	Polymer	Thin	318	300	9	[73]
BCZT	Ceramic	Thick	363	30	1.32	[74]
P(VDF–TrFE–CFE)0.9–P(VDF-TrFE–CTFE) 0.1	Polymer	Thin	318	120	6	[75]
$BaTiO_3$	Ceramic	Thick	-	2.8	0.45	[70]
P(VDF–TrFE–CFE) 56.2/36.3/7.6 quenched	Polymer	Thin	318	300	5	[73]
PMN-13% PT ceramic	Ceramic	Bulk	303.15	2.4	0.3	[76]
P(VDF–TrFE) 55/45	Polymer	Thin	353	209	12.6	[50]
PMN	Ceramic	Bulk	289	9	2.5	[68]
0.65 PMN 0.35 PT	Ceramic	Thin	413.15	75	31	[77]
P(VDF-TrFE-CFE) + 5 wt % of P(VDF-CTFE)	Polymer	Thin	-	170	12	[72]
5CB	Liquid crystal	-	312	-	3.35~5.26	[78]
$KTaO_3$	Single crystal	-	13	1.56	0.25	[79]

Table 1.3 outlines the ECE characteristics of typical electrocaloric materials. Some ECE studies have been chosen from the literature on ferroelectric single crystal, polycrystalline, thin/thick films, and polymers. Where high voltages can be applied, and significant ECE reactions have been observed. Relaxor ferroelectric polymers provide the best ECE properties for practical cooling device applications due to their high ΔT and ΔS, wide operating temperature range, and ease of scaling up for different device sizes. In this direction, relaxor ferroelectrics have a strong EC response at ambient temperature in a broad temperature span due to polar nano regions [80]. In this context, $PbMg_{1/3}Nb_{2/3}O_3$ (PMN) film having a thickness of 43 µm in the cantilever exhibits an EC temperature

change of 0.07 K at 10 kV/cm, comparable with bulk PMN form (0.09 K) [81]. However, the bulk PMN shows an EC of 1.09 K when an electric field is increased to 60 kV/cm [81]. Further, multilayer capacitors (MLCs) film of doped $BaTiO_3$ ceramic with a thickness of 11 μm with Ni inner electrodes (2.0 μm thick) show an EC of 1.5 K. However, MLCs with thinner (about 1 μm) EC layers withstand significant temperature changes of up to 7.2 K at 333 K in an ultrahigh electric field of 800 kV/cm [82, 83]. Mischenko *et al*. [45] reported the large ECE response of 12 K in $Pb(Zr_{0.95}Ti_{0.05})O_3$ (PZT) ceramic thin films near and above the F-P phase transition (~495 K). Ceramic thin films of $PbMg_{1/3}Nb_{2/3}O_3$-$PbTiO_3$ also show a ΔT_{ad} of 5 K[59]. However, $PbSc_{0.5}Ta_{0.5}O_3$ (PST) ceramics have recently attracted more attention due to their fast first-order phase transition at room temperature. In PST bulk ceramic [84] and MLCs [85], large EC ΔT_{ad} of 3.7 K and 5.5 K were found. Most electrocaloric materials explored so far are lead-based. Handling lead, a hazardous element, requires extra precautions to reduce health and environmental risks[86]. Moreover, PVDF-based EC materials offer much potential for usage in micro equipment because of their low cost, lightweight, environmentally friendliness, and flexibility[87]. P(VDF-TrFE)--based ferroelectric polymers are the most promising material for achieving large electrocaloric (EC) reactions due to their ability to withstand substantial temperature changes and scalability in size and shape[88]. Moreover, compared with ferroelectric ceramics, polymers' lightweight and fracture tolerance make them very attractive for practical cooling devices[89]. PVDF (poly(vinylidene-difluoride)) is widely utilized in piezoelectric and pyroelectric applications due to its superior processability, dielectric and mechanical properties, and resistance to chemicals and electricity[90-93]. Lu *et al*. [94, 95] found a ΔT_{ad} of 12 K at 209 V/μm in P(VDF-TrFE) 55%/45% (in mole) by Maxwell relations.

Furthermore, the P(VDF-TrFE) copolymer's large hysteresis loss reduces its efficiency since it produces heat, which is undesirable in a cooling device[57]. To enhance material performance, flaws in the P(VDF-TrFE) copolymer were modified to convert it into a relaxor ferroelectric, lowering the transition temperature and eliminating hysteresis[44]. The ferroelectric relaxor polymers based on P(VDF-TrFE) demonstrate a wide dielectric peak range and a significant dielectric constant at ambient temperature[57]. A very large ΔT ~ 16 °C was induced in a 160 MVm^{-1} electric field, as demonstrated by the ECE of the P(VDF-TrFE-CFE) 59.2/33.6/7.2 mol% terpolymer directly measured at 30 °C; in addition to the significant ECE, some relaxor ferroelectric polymers also exhibit a near

temperature independent ECE[57]. Simultaneously, EC polymers have been extensively explored because they are environmentally friendly compared to lead-based EC compounds like PMN, PZT, and PST [43]. They are gaining popularity due to their scalability, large ΔT_{ad}, and capacity to produce high cooling power [8, 42, 96]. The high isothermal entropy change (large EC), low weight, flexibility and low-temperature production poly(vinylidene fluoride) (PVDF) is an attractive material compared to other ferroelectric materials[73]. Other caloric materials, such as PVDF-based polymers, are environmentally safe and have great caloric performance but are expensive[50]. Further, polyvinylidene fluoride-trifluoro ethylene-chlorotrifluoroethylene terpolymer P(VDF-TrFE-CFE) consists of an even more giant ECE and electrostrictive effect than PVDF[10]. P(VDF-TrFE-CFE) is a suitable EC material due to its higher room temperature dielectric constant, polarization (0.1 C/m^2) and electric breakdown field (> 400 MV/m)[10]. By IR imaging, Sebald *et al.* [97] observed a 2.7 K temperature change in 50 μm thick freestanding P(VDF-TrFE-CFE) at 303 K. Further, Neese *et al.* [50, 95] reported a large EC adiabatic temperature and entropy change of 12 K and 55 J/(kg·K) in ferroelectric PVDF-TrFE and relaxor ferroelectric PVDF-TrFE-CFE at the above phase transition temperature. The P(VDF-TrFE-CFE) consists of high entropy and ΔT_{ad} near room temperature [50]. The EC materials should have a high ΔT_{ad} and a low operating temperature, near 298 K, for practical applications[98]. Thus, it has been selected as an EC material for analysis. EC devices are frequently considered the best chip-scale and compact active thermal control option. It manifests as an EC substance being heated or cooled when an electric field is applied in adiabatic conditions[44]. In the past decade, ECE has been determined in various materials, and proposals for EC cooling devices have been suggested [38]. In this direction, a finite element analysis has been used for EC cooling, considering the outer surface of the battery to be at a temperature of 320 K. Additionally, the impact of the electric field and frequency on the cooling is studied. These all are discussed in subsequent chapters 2, 3, 4, and 5.

1.5 Research objectives

This work focuses on electrocaloric effect-based electrocaloric devices to solve the problem of high-temperature-based battery-powered devices. The performance of the ECE device is investigated with the following objectives:

1. To find out the optimum electric field and its pulse

2. To investigate suitable electrode and substrate materials as well as thickness effect on ECE

3. Effect of battery/source thickness on electrocaloric cooling

4. Performance of an EC device for an effective heat transfer

1.6 Thesis Structure

In this work, the P(VDF-TrFE-CFE) terpolymer is chosen as an EC material due to its higher EC temperature change, flexibility, scalability, and environmental friendliness. Chapter 1 introduces the reader to the motivation behind improving cooling technology for effective thermal management for different types of devices with limited space. The conventional cooling methods are compared to solid-state cooling approaches to determine the most effective cooling technique. The workings of ECE and comparing the best EC materials have been discussed. The COMSOL Multiphysics simulation is used for the EC analysis, considering P(VDF-TrFE-CFE) as an EC material. Chapter 2 discusses the methodology of ECE. Equation-based modeling and the built module in COMSOL are compared for EC estimation, and the built pyroelectricity module is recommended for a more accurate analysis. The model is validated to ensure its accuracy.

Chapter 3 investigates the influence of an electric pulse and its holding time on ECE. The impact of various electrical pulses is investigated. To achieve the maximum ECE, the electric field's magnitude and an EC cycle's holding time are altered as needed. Chapter 4 describes P(VDF-TrFE-CFE) (63.2/29.7/7.1 mol%) as an EC material supported by a substrate and electrodes on both sides. This simulation study investigates the effect of electrode/substrate material and thickness and the operating temperature of the battery (source) on the EC material. A design for an electrocaloric device for battery cooling is proposed. Chapter 5 investigates the battery/source cooling in air and uses an EC device to assess efficient heat transfer. Further, analysis is conducted to identify the time necessary for the battery (source) to cool down and the effect of the operating temperature of the battery (source) on ECE. The primary goal of the proposed study is to achieve adequate cooling of the battery (source) via the EC device. The suggested EC device design may offer fresh perspectives for electronic cooling applications like mobile ones.

<div align="right">

Chapter 2

</div>

Methodology & Modeling

This chapter describes the equation-based and inbuilt modeling to estimate the electrocaloric effect (ECE). Equation-based modeling uses heat accumulation-based relations, whereas the built-in model uses maxwell relations. Initially, equation-based modeling analyzes the ECE and validates the model with the literature. The built-in electrocaloric module was unavailable in the COMSOL, but it was added in a later version. Thus, the inbuilt model is also discussed in detail. The model has been checked for mesh sensitivity analysis. Then, ECE and electric strain validation were done to verify the modeling. The results suggest that any equation-based modeling or an inbuilt model can be used for electrocaloric analysis.

2.1 Introduction

Several simulation methods are available to predict electrocaloric (EC) potential in the material. However, these simulations do not provide heat transfer modeling with a heat source or sink. In the literature, most research focused on the adiabatic temperature change due to the applied electric field at a given temperature rather than actual heat transfer analysis with a heat source/sink. In this direction, Ponomareva *et al.*[99] have investigated the ECE in $Ba_{0.5}Sr_{0.5}TiO_3$ using Monte Carlo methods. However, Rose *et al.*[100] have used molecular dynamics (MD) simulations and core-shell interatomic potentials to model the ECE in bulk $LiNbO_3$. Similarly, Chen *et al.*[101] considered the atomic potential to model ECE in $BaTiO_3$ nanoparticles. Further, atomistic first principles-based simulations reveal that both direct and indirect approaches yield the same qualitative and quantitative predictions for the ECE[99].

They used simulation and experimentation to examine the relationship between the ECE and the relaxor state transition of $BaZr_xTi_{1-x}O_3$[102]. Furthermore, the ECE is shown in ferroelectric nanowires from atomistic simulation.[6][103] Moreover, the monolayer germanium sulfide (GeS) ECE is investigated using molecular dynamics (MD) simulations and thermodynamic analysis[104]. The ECEs in $BaTiO_3$ single crystals are also investigated using molecular dynamics simulation of a first principles-based effective Hamiltonian[105]. The literature suggests that most studies have utilized first principles-based analysis, Monte Carlo simulation, or molecular dynamics methods to estimate the ECE. However, these studies need to have the scope to include the effect of electrode

material, the effect of substrate material/thickness, and heat transfer with source/sink. Recently, a few studies have used COMSOL Multiphysics software to model ECE. In this direction, utilizing COMSOL modeling, the study optimizes high-performance electrocaloric devices with ferroelectric polymer nanocomposites (BN_f + BCZT@$BaTiO_{3(f)}$ + PVDF), achieving remarkable cooling power density (162.2 W/cm^3 at 4 Hz) and energy storage density (33.4 J/cm^3 at 500 MV/m)[106]. Ursic *et al.*[107] identified thick films of (1-x)PMN-xPT as potential candidates for prototyping devices using a COMSOL Multiphysics analysis.

The thick films, manufactured as cantilevers, exhibit considerable EC characteristics (up to 2 K) and high bending displacements (up to 600 μm) at modest electric fields[107, 108]. This study presents a micro-scale refrigeration system leveraging the ECE, evaluated through finite element simulations. Notably, system performance peaks at 15 Hz, achieving a cooling power density of 3 W/cm^2 and a COP of 31% of Carnot at a 15 K temperature span, with potential for enhancements through increased electric field magnitude[109]. This study develops a two-dimensional (2-D) mathematical model of an active electrocaloric refrigerator using COMSOL Multiphysics 5.2 with a computational fluid dynamics (CFD) module, accurately estimating heat flux and cooling power. However, these COMSOL-based studies did not consider the effect of material parameters and heat transfer. It can be incorporated into the COMSOL due to the user-friendly Multiphysics interface, which facilitates a detailed analysis of the ECE.

This chapter investigates the ECE using computational modeling, specifically employing equation-based mathematical modeling within the COMSOL Multiphysics software. A detailed equation-based mathematical formulation is described to assess the ECE. Initially, the COMSOL software did not have a module for the ECE, but eventually, it was added in the latest version. Thus, the in-build pyroelectricity module of the COMSOL software is used for electrocaloric analysis, which is described step-by-step in detail. The mesh-independent analysis and model validation ensure that the simulated results align with experimental observations or previously published literature.

2.2 Equation-based modeling

The ECE is a reversible temperature change under adiabatic conditions or isothermal change in entropy when an electric field is applied or removed from a dielectric medium, as shown in Figure 1.1. For example, an electric field is applied on a polar dielectric (E =

E_{max}), the dipoles are aligned along the direction of the electric field, and electric polarization develops (process A–B, see Figure 1.1). The dipole orientation change affects the material's entropy (S), and total entropy (S_{total}) is written by[44],

$$\Delta S_{total} = \Delta S_{dipolar}(T, \boldsymbol{E}) + \Delta S_{lattice}(T) \tag{2.1}$$

The material's dipolar entropy (a function of temperature (T) and electric field (E)) decreases when the dipoles are ordered. The lattice entropy (a function of temperature only) has no change since it is independent of the applied electric field. Equation 2.1 suggests that a change in temperature affects all entropies in the system, whereas a change in the applied electric field affects only the polarization entropy.

The EC material is now applied/removed in an external electric field, transferring heat from the thermal load to the heat sink or surroundings. The internal energy change (first law of thermodynamics) per unit volume of a thermodynamic system is given by [48],

$$dU = dQ + dW \tag{2.2}$$

where U denotes the system's internal energy, Q represents the heat absorbed from the outside, and W is the work done by the outside on the system. According to the second law of thermodynamics, for a reversible process, the heat absorbed by the system can be computed using the product of absolute temperature (T) and entropy (S) [48]:

$$dQ = TdS \tag{2.3}$$

In the case of a homogeneous dielectric medium, the outside work consists of two contributions: mechanical work (dW_M) and electrical work (dW_E). In the case of a homogeneous elastic material, when the electric field is applied, the outside work of the dielectric system subjected to an infinitesimal change in strain and electric displacement can be stated as [48]

$$dW = dW_M + dW_E = \boldsymbol{\sigma_{ij}}d\boldsymbol{\varepsilon_{ij}} + \boldsymbol{E_i}d\boldsymbol{D_i} \tag{2.4}$$

where σ_{ij} is stress, ε_{ij} is strain, E_i is the applied electric field and D_i is the displacement polarization in tensor form. Substituting the value of dQ and dW from equations (2.3) and (2.4) in equation (2.2), the equation becomes,

$$dU = TdS + \boldsymbol{\sigma_{ij}}d\boldsymbol{\varepsilon_{ij}} + \boldsymbol{E_i}d\boldsymbol{D_i} \tag{2.5}$$

Based on equation (2.5), the Gibbs free energy (G) is represented by [51, 110]:

$$G = U - TS - \boldsymbol{\sigma_{ij}}\boldsymbol{\varepsilon_{ij}} - \boldsymbol{E_i}\boldsymbol{D_i} \tag{2.6}$$

Taking the differential of G and substituting equation (2.5) into equation (2.6):

$$dG = - SdT - \boldsymbol{\varepsilon_{ij}}d\boldsymbol{\sigma_{ij}} - \mathbf{D_i}d\mathbf{E_i} \tag{2.7}$$

The exact differential can be written as [51, 110]:

$$dG = \left(\frac{\partial G}{\partial T}\right)_{\boldsymbol{\sigma,E}} dT + \left(\frac{\partial G}{\partial \sigma_{ij}}\right)_{T,\boldsymbol{E}} d\boldsymbol{\sigma_{ij}} + \left(\frac{\partial G}{\partial E_i}\right)_{T,\boldsymbol{\sigma}} d\boldsymbol{E_i} \tag{2.8}$$

Here and onwards, the subscript (outside bracket) represents that quantity is measured considering these variable constants. Consequently, the definitions of the other three unconstrained variables in terms of T, $\sigma_{ij,}$ and E_i are [51, 110]:

$$-S = \left(\frac{\partial G}{\partial T}\right)_{\boldsymbol{\sigma,E}}, -\boldsymbol{\varepsilon_{ij}} = \left(\frac{\partial G}{\partial \sigma_{ij}}\right)_{T,\boldsymbol{E}}, -\boldsymbol{D_i} = \left(\frac{\partial G}{\partial E_i}\right)_{T,\boldsymbol{\sigma}} \tag{2.9}$$

S, $\varepsilon_{ij,}$ and D_i are unconstrained variables, and their linear differential form is considered as follows[51, 110]:

$$dS = \left(\frac{\partial S}{\partial T}\right)_{\boldsymbol{\sigma,E}} dT + \left(\frac{\partial S}{\partial \sigma_{kl}}\right)_{T,\boldsymbol{E}} d\boldsymbol{\sigma_{kl}} + \left(\frac{\partial G}{\partial E_n}\right)_{T,\boldsymbol{\sigma}} d\boldsymbol{E_n} \tag{2.10}$$

$$d\boldsymbol{\varepsilon_{ij}} = \left(\frac{\partial \varepsilon_{ij}}{\partial T}\right)_{\boldsymbol{\sigma,E}} dT + \left(\frac{\partial \varepsilon_{ij}}{\partial \sigma_{kl}}\right)_{T,\boldsymbol{E}} d\boldsymbol{\sigma_{kl}} + \left(\frac{\partial \varepsilon_{ij}}{\partial E_n}\right)_{T,\boldsymbol{\sigma}} d\boldsymbol{E_n} \tag{2.11}$$

$$d\boldsymbol{D_m} = \left(\frac{\partial D_m}{\partial T}\right)_{\boldsymbol{\sigma,E}} dT + \left(\frac{\partial D_m}{\partial \sigma_{kl}}\right)_{T,\boldsymbol{E}} d\boldsymbol{\sigma_{kl}} + \left(\frac{\partial D_m}{\partial E_n}\right)_{T,\boldsymbol{\sigma}} d\boldsymbol{E_n} \tag{2.12}$$

Or

$$d\boldsymbol{D_m} = \boldsymbol{p_m^{\sigma,E}}dT + \boldsymbol{d_{mkl}^{T,E}} d\boldsymbol{\sigma_{kl}} + \in_{mn}^{T,\sigma} d\boldsymbol{E_n} \tag{2.13}$$

The compliances in equation 2.13 relate the pyroelectric coefficient $(\mathbf{p_m})$ $= \left(\frac{\partial D_m}{\partial T}\right)_{\boldsymbol{\sigma,E}}$, piezoelectric coefficients $(\mathbf{d_{mkl}})$ $= \left(\frac{\partial D_m}{\partial \sigma_{kl}}\right)_{T,\boldsymbol{E}}$, dielectric constants $(\in_{\mathbf{mn}})$ $= \left(\frac{\partial D_m}{\partial E_n}\right)_{T,\boldsymbol{\sigma}}$. Based on Eqs. (2.8) – (2.12), the relationship between temperature T (entropy S) and electric field E_m (electric displacement D_i) for a stress-free system is expressed by [48]

$$-\left(\frac{\partial^2 G}{\partial E_i \partial T}\right)_{\boldsymbol{\sigma}} = \left(\frac{\partial D_i}{\partial T}\right)_{\boldsymbol{\sigma,E}} = \boldsymbol{p_i}^{\sigma,E} \tag{2.14}$$

$$-\left(\frac{\partial^2 G}{\partial T \partial E_i}\right)_{\boldsymbol{\sigma}} = \left(\frac{\partial S}{\partial E_i}\right)_{T,\boldsymbol{\sigma}} \tag{2.15}$$

The ECE coefficient under isothermal conditions is given by [48]:

$$\left(\frac{\partial D_i}{\partial T}\right)_{\boldsymbol{\sigma,E}} = \left(\frac{\partial S}{\partial E_i}\right)_{T,\boldsymbol{\sigma}} = \boldsymbol{p_i^{\sigma,E}} = \boldsymbol{p_i^{T,\sigma}} \tag{2.16}$$

The equations (2.16) show the derivation process using the set of independent variables (T, σ_{ij}, and E_i) to describe the adiabatic temperature changing; the other set of independent variables (S, σ_{ij} (or ε_{ij}) and E_i) can also be used and repeat the procedure from equations (2.6) to (2.16). A dielectric material's heat capacity, C_E (per unit volume under constant electric field), can be calculated by $C_E = T(\partial S/\partial T)$ (detailed procedure is ignored). However, the corresponding Maxwell relation under constant stress or strain is expressed as [48]:

$$-\left(\frac{\partial T}{\partial E_i}\right)_S = \left(\frac{\partial D_i}{\partial S}\right)_E = \left(\frac{\partial D_i}{\partial T}\cdot\frac{\partial T}{\partial S}\right)_E = \left(\frac{\partial D_i}{\partial T}\right)_E \cdot \frac{T}{C_E} = \frac{Tp_i^E}{C_E} \tag{2.17}$$

When the differential form is converted into the integral form during a quasi-static process, the isothermal entropy (ΔS) changes under stress-free conditions [43, 49]:

$$\Delta S = \int_{E_1}^{E_2}\left(\frac{\partial D_i}{\partial T}\right)_E dE_i \tag{2.18}$$

Under an applied electric field E_i and displacement polarization D_i, the adiabatic temperature change (ΔT_{ad}) under stress-free conditions is given by [45]:

$$\Delta T_{ad} = -\int_{E_1}^{E_2}\frac{T}{C_E(T)}\left(\frac{\partial D_i}{\partial T}\right)_E dE_i \tag{2.19}$$

The electric displacement can be defined as $D_i = \varepsilon_0 E_i + P_i$, where ε_0 is the permittivity of the vacuum. $\varepsilon_0 E_i$ is temperature independent; hence $\partial D_i/\partial T \cong \partial P_i/\partial T$. Equation 2.19 gives that temperature change in EC materials results from entropy change and is directly connected to displacement under given electric fields [50]. The properties of P(VDF-TrFE-CFE) material are provided in Table 2.1. However, ferroelectric polymers consist of a significant contribution by a secondary pyroelectric coefficient (i.e., 25-50 %) as reported by Neese *et al.*[50]. Moreover, ECE in P(VDF-TrFE-CFE) has other parameter contributions such as nonlinearity in polarization with an electric field, presence of polar polymers[50] and relaxor ferroelectric behavior[111], etc., which affect the $\Delta T_{ad.}$ Thus, the pyroelectric coefficient is enhanced so that it shows ΔT_{ad} of 4.9 K at 100 MV/m, and the same is used throughout the simulation instead of 60 $\mu C/m^2 K$. The heat stored and accumulated in the solid medium is represented by $\rho C_p \frac{\partial T}{\partial t}$, the conduction heat is $\nabla \cdot (-k\nabla T)$, the heat source is $Q + q_s T$, the convective heat is $\rho C_p u \cdot \nabla T$, the viscous heat dissipation is τ_s, and pressure work is given by $\frac{T}{\rho}\left(\frac{\partial \rho}{\partial T}\right)_P\left(\frac{\partial P_a}{\partial t} + u \cdot \nabla P_a\right)$ where P_a is the atmospheric pressure.

Table 2.1. The properties of P(VDF-TrFE-CFE) material used in the present study. [10, 112]

Property	P(VDF-TrFE-CFE)
Density (kg/m³)	1800
Young's modulus (GPa)	2.17
Poisson's ratio	0.37
Heat capacity (C_p) (J/Kg·K)	1600
Thermal conductivity (k) (W/m·K)	0.2

For simulation, the fundamental heat transfer equation in differential form is described as follows [106],

$$\rho C_p \left(\frac{\partial T}{\partial t}\right) + \rho C_p u \cdot \nabla T + \nabla \cdot \boldsymbol{q} = Q + Q_{ted} \tag{2.20}$$

The generalized in-built governing equation in COMSOL Multiphysics is given as,

$$\rho C_p \frac{\partial T}{\partial t} + \nabla \cdot (-k\nabla T) = Q + q_s T - \rho C_p u \cdot \nabla T + \tau_S + \frac{T}{\rho}\left(\frac{\partial \rho}{\partial T}\right)_P \left(\frac{\partial P_a}{\partial t} + u \cdot \nabla P_a\right) \tag{2.21}$$

where ρ is the density, C_p is the material's heat capacity at constant pressure, $\nabla \cdot (-k\nabla T)$ corresponds to conductive heat transfer, τ_s is viscous heat dissipation, and k is the material's thermal conductivity. The heat transfer is assumed only through conduction, and other terms will be neglected. Thus, $(\rho C_p u \cdot \nabla) = 0$, and $Q_{ted} = 0$ where Q_{ted} is thermoelastic damping; the equation (20) is rewritten as [106],

$$\rho C_p \left(\frac{\partial T}{\partial t}\right) - \nabla^2 T = Q \tag{2.22}$$

Further, the work done by Gu *et al*.[113] and Hassan *et al*.[106] describes the governing equation for EC module as,

$$\rho C_p \frac{\partial T_{(x,y,z)}}{\partial t} = k\Delta^2 T_{(x,y,z)} - \rho T \frac{\partial S_{(E,T)}}{\partial \boldsymbol{E}} \frac{\partial \boldsymbol{E}}{\partial t} \tag{2.23}$$

where ρ, C_p and k are considered at constant electric field (E). The temperature change by ECE results from S due to E obtained by [96],

$$S = C_1 \boldsymbol{E}^2 + C_2 \boldsymbol{E} \tag{2.24}$$

C_1 and C_2 are constants. The above equation is used for P(VDF-TrFE-CFE) to fit the entropy as a function of the electric field [51]. By comparing equations (2.22) and (2.23), heat source(Q) is obtained to be,

$$Q = -\rho T \frac{\partial S}{\partial \mathbf{E}} \frac{\partial \mathbf{E}}{\partial t} \text{ (W/m}^3) \tag{2.25}$$

where $\frac{\partial \mathbf{E}}{\partial t}$ is the change in the electric field with time. The equation (2.25) is rewritten as [106]

$$\rho C_p \left(\frac{\partial T}{\partial t}\right) - \nabla^2 T = -\rho T \frac{\partial S}{\partial \mathbf{E}} \frac{\partial \mathbf{E}}{\partial t} \text{ or Q} \tag{2.26}$$

Further, by solving equation (2.26), the ECE $\left(\frac{\partial T}{\partial t}\right)$ can be obtained. However, the entropy obtained from equation (2.24) depends on coefficients C_1 and C_2, which further depends upon entropy electric field variation. Hence, the above equation concerning the material used and the applied–electric field is limited. Therefore, an alternate modeling approach with a pyroelectric coefficient (p_i) can be derived from Maxwell's relation [51, 114].

$$\left(\frac{\partial D}{\partial T}\right)_{\mathbf{E}} = \left(\frac{\partial S}{\partial \mathbf{E}}\right)_T \tag{2.27}$$

Now, by putting the value of equation (2.27) in equation (2.25),

$$Q = -\rho T \cdot \boldsymbol{p_i} \cdot \frac{\partial \mathbf{E}}{\partial t} \tag{2.28}$$

Additionally, equation (2.28) gets divided by ρ to match the unit (W/m^3) as of equation (2.25). Hence, the equation of the alternate modeling approach is as follows,

$$Q = -T \cdot \boldsymbol{p_i} \cdot \left(\frac{\partial \mathbf{E}}{\partial t}\right) \tag{2.29}$$

The equation (2.26) can be rewritten with the help of equation (2.29) as follows,

$$\rho C_p \left(\frac{\partial T}{\partial t}\right) - \nabla^2 T = -T \cdot \boldsymbol{p_i} \cdot \left(\frac{\partial \mathbf{E}}{\partial t}\right) \tag{2.30}$$

This equation (2.30) can be used to obtain the $\Delta T_{\text{ad}} = \left(\frac{\partial T}{\partial t}\right)$. However, ΔT_{ad} is accompanied by losses due to thermal contact resistance, hysteresis, loss due to electric waveforms, heat losses in the environment, etc. In this regard, the effective electrocaloric temperature change $(\Delta T_{\text{ad}})_{\text{effective}}$ considering losses is written as

$$(\Delta T_{\text{ad}})_{\text{effective}} = \Delta T_{\text{ad}} - \Delta T_{hys} - \Delta T_{tc} - \Delta T_{other} \tag{2.31}$$

where ΔT_{hys} is the hysteresis loss (under different electric pulse forms), ΔT_{tc} is thermal contact loss between various layers of the ECE device and source/sink, and ΔT_{other} is other losses. The P(VDF-TrFE-CFE) has a small hysteresis loss due to its relaxor ferroelectric characteristics. Bauer *et al.*[10] have reported thin polarization-electric field

(P-E) hysteresis loops and small dielectric loss. Moreover, it is shown that a higher electric field in thin films above 150 MV/m enhances hysteresis loss[115]. However, the present work is limited to applying only 100 MV/m. Thus, small hysteresis loss can be expected. A previous study on PZT ($PbZr_{0.95}Ti_{0.05}O_3$) thin films estimated the hysteresis loss to be, at worst, 5% of cooling power [116]. The hysteresis loss of ferroelectric ceramics is affected by microlevel compositional fluctuations and their impact on relaxation time distributions [117]. However, a reduction in hysteresis is possible through improved control of synthesis conditions, substituents, and types of electric pulse. Hence, the hysteresis loss due to various electric field pulses can be a maximum of 5%. To simplify the simulation, the present work assumed that 5% of losses occur due to hysteresis ($\Delta T_{hys} = 5\%$) in the reported EC ΔT_{ad}.

The ΔT_{tc} is temperature losses due to thermal contact resistance at various interfaces (electrocaloric material-electrode ($\Delta T_{ec\text{-}electro}$), electrode-substrate ($\Delta T_{electro\text{-}sub}$), substrate-heat source/sink ($\Delta T_{sub\text{-}source}$), or electrode-source/sink ($\Delta T_{electro\text{-}sink}$). The experimental thermal contact resistance taken from the literature is 1×10^{-4} m^2K/W [118], 1.2×10^{-8} m^2K/W [119, 120] and 4×10^{-5} m^2K/W [121, 122] for P(VDF-TrFE-CFE)-Au (ec-electro), Au-Al (electro-sub) and Al(substrate)-Al (heat source) (sub-source/sink), respectively for estimation of losses. The experiment data for thermal contact resistance between P(VDF-TrFE-CFE)-Au and Au-Al are unavailable; hence, polymer-metal [118] and metal-metal [119, 120] are considered. Here, it should be noted that the thicknesses of polymer-metal and metal-metal layers are thin in references [118-122] compared to the present work. The total ΔT_{tc} can be written as

$$\Delta T_{tc} = \Delta T_{ec-electro} + \Delta T_{electro-sub} + \Delta T_{sub-source/sink} \text{ } or \text{ } \Delta T_{electro-source/sink}.$$ The ΔT_{TC} is expressed as the product of heat flux (Q) and thermal contact resistance (R_{th}), given by

$$\Delta T_{tc} = Q \times R_{th} \tag{2.32}$$

The ΔT_{tc} obtained from the experimental thermal contact resistance is 11-13.5% of the total EC ΔT_{ad}. However, other losses ΔT_{other}, such as joule heating, eddy current, thermal hysteresis, and thermal contact resistance from the electrode to sink ($\Delta T_{electro\text{-}sink}$), are assumed to be negligible[5, 49, 123]. Various researchers have previously considered a similar assumption[5, 49, 123]. A time-dependent simulation is carried out in COMSOL Multiphysics. The detailed explanation of the modeling in COMSOL is discussed further

for better understanding. The theory behind the ECE, as proposed by Maxwell, requires the implementation of its equations in software for equation-based modeling to predict this phenomenon. However, with the release of COMSOL's in-built pyroelectricity module, which offers simplicity in interpretation and ease of understanding results, it became the preferred tool for further analysis. The step-by-step inbuilt model for analysis is described in section 2.3.

2.3 COMSOL Modeling

The ECE is investigated in COMSOL Multiphysics utilizing three modules: electrostatics, heat transfer in solids, and pyroelectricity. These modules are chosen from the COMSOL Multiphysics software's initial interface for time-dependent investigations. Figure 2.1 provides detailed information regarding COMSOL modeling. To begin understanding the modeling, the global definition has defined the parameters tab, which includes all relevant material constants such as E0, thermal conductivity, density, and specific heat. All this information is derived from the literature (Table 2.1). Figure 2.1 shows Component 1, which contains a definition tab with various functions. The electric field varies with time. As a result, the phrase E(t) is defined in the variable tab because the electric field cycle affects the electrode material, which changes over time. There are various electric pulses available for applying an electric field.

However, after a thorough examination of the effect of the electric pulse on the ECE, it was shown that the square pulse causes a significant adiabatic temperature change. The function for applying a square electric pulse was created manually using the line equation. The trial-and-error method optimizes the cycle time, with holding time considered. The final square electric pulse cycle is created, which may be converted into a function by applying the points value to the equation of the line formula. A piecewise function is employed when the start and end locations and the function are dependent on time.

Furthermore, any function can be produced simply by entering the starting and ending points' values into the piecewise function. The parameter is set to t (time); extrapolation is periodic since the cycle must be repeated to run continuously. Smoothing is typically used to smooth the endpoints where there is a sharp leap or change in direction; this is required since the solution may fail to converge at that point. As a result, it is recommended to smooth the curved points using the relative size of the transition zone, which is 0.001. The size of the transition zone is set to 0.001. The smaller the transition zone size, the

smoother the curved points will be, but this will require more computing time. As a result, in the present investigation, the transition zone size is 0.001, which is more than adequate. Now, the cycle is provided as a piecewise function (see Figure 2.1). However, the essential requirement is to use the electric pulse cycle, which has a voltage unit for a time in seconds. Initially, the electric field magnitude was set at approximately 100 MV/m. This electric field magnitude is multiplied by the piecewise function (pw1(t)), i.e., (pw1(t)*E0), where E0 equals 100 MV/m. The Analytic 1 function's value is E(t). The unit of the phrase (pw1(t)*E0) is MV/m; however, the electric potential can only take equations using voltage as the unit. In addition, another analytic function is added to address this problem. When converting from MV/m to MV, multiply by the electrode potential thickness. The thickness of the polymer substance is set at 100 μm. As a result, the analytic 2 (an2(t)) function is defined as E(t) multiplied by polymer thickness. Now, the an2(t) function applies directly to the electric potential tab, which will be explained further. Furthermore, the probe plot is configured to display the resulting metrics, including temperature, stress, strain, and deformation. There are several probe selection points, including domain, point, boundary, edge, domain point, boundary point, and global variable. The probe can be chosen from the probe tab based on the requirements.

In this investigation, the temperature of the polymer and source materials must be monitored. For this reason, the domain prob is chosen, which displays the temperature(K) vs. time(s) graph, allowing the change in adiabatic temperature to be viewed. All representation-related options can be configured in the display tab, including geometry labels, grid, axis orientation, axis units, and so on. The detailed discussion related to component 1 is finished up to this point. Figure 2.1 shows the geometry 1 tab, where the problem's needed geometry can be built using various shapes and geometrical constraints. The shape required for this investigation is rectangular, with layers of air, a top electrode, P(VDF-TrFE-CFE), a bottom electrode, a substrate, and a battery supply. Before constructing the geometry, the length unit is set as μm, which can be changed to any unit for convenience. The rest of the geometry tab's options are solely used by default. Rectangular layers in the current investigation are $70000 \times 30000 \ (\mu m)^2$. Air, P(VDF-TrFE-CFE), gold electrode, substrate, and source have 100, 0.1, 100, and 100 μm thicknesses, respectively (see Figure 2.1). All this length, width, and height information is entered into the size and shape section, which can also be adjusted based on the analysis requirements.
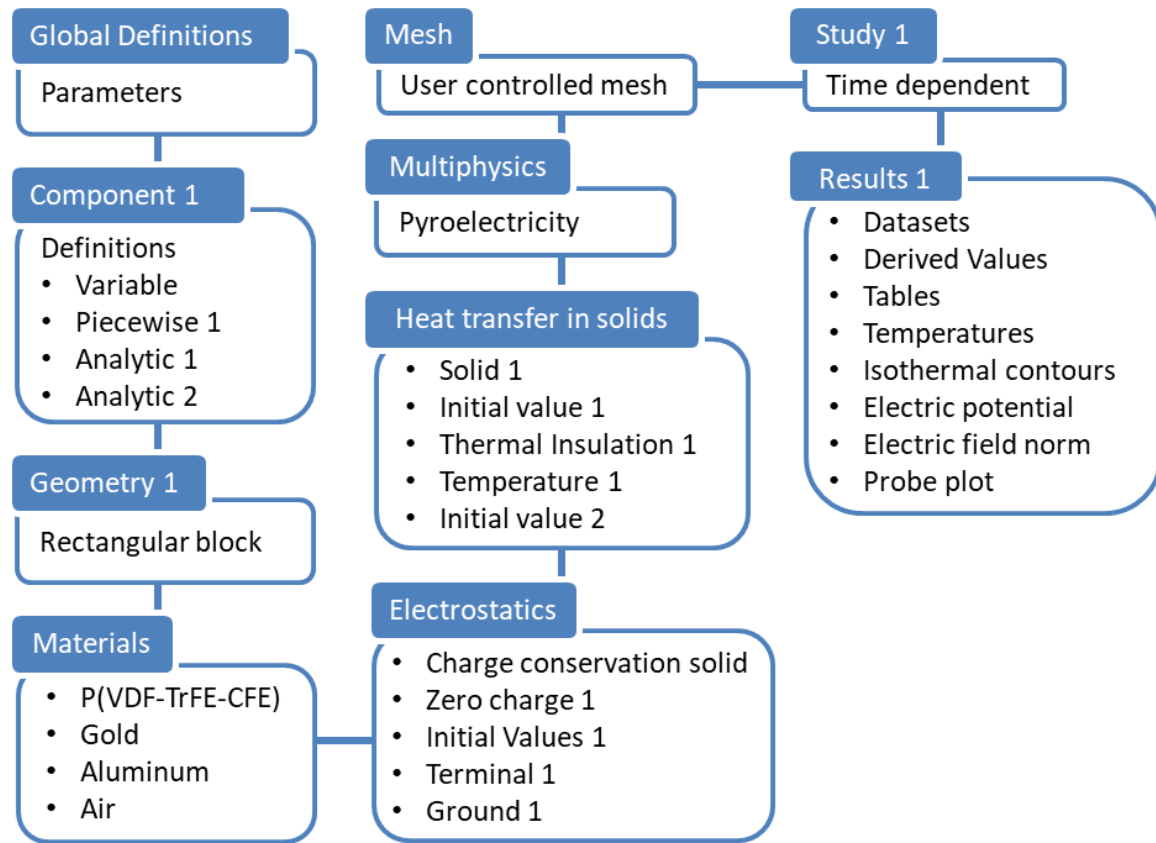
Figure 2.1. Detailed information about COMSOL modeling.

The block's position can change based on the geometrical structure at the corner or the center, with changing values of x, y, and z directions. The axis type tab also lets you specify the geometry's normal direction. Coordinate systems can also be specified in work planes, such as xy or yz. Aside from these settings, the rest are left as is. Figure 2.1's material section requires each block constructed in the geometry section to be assigned a material. The COMSOL Multiphysics software contains an in-built material library. In general, it includes all the necessary material properties. Nonetheless, if it is not available, the material property can be found in relevant literature data. The same information can be manually entered into the material property list. Assigning a material to each geometric part is necessary; otherwise, errors will occur. The ECE is based on the idea that providing an electric field with pulses can change adiabatic temperature. When an electric pulse is supplied to an electrode coated with the electrocaloric material, it absorbs and releases heat. In this example, two fundamental principles are used: electrostatics and heat transfer in solids, which are the modules for applying an electric pulse and analysing heat transfer. The discussion of these modules is further explained.

Figure 2.1 depicts the electrostatics section, which applies to all blocks, with the volt as the dependent variable. Electrostatics calculates the electric field, electric displacement field, and potential distributions within dielectrics where the electric charge distribution is explicitly described. It remains stationary in its basic form but can incorporate other physical interactions. It is compatible with eigenfrequency, frequency-domain, small-signal analysis, and time-domain modeling in all spatial dimensions. The physics interface solves for the electric field using the scalar electric potential as the dependent variable, as per Gauss' law. The charge conservation solid tab includes the electric potential equation. It consists of a Settings window for specifying the constitutive relation of the electric displacement field, along with its related properties such as relative permittivity. In the terminal 1 tab, it applies to the top gold electrode layer. Voltage is set as terminal type analytic 2 function applies to voltage tab as an2(t).

Moreover, ground 1 is applicable to the bottom gold electrode layer. That means electric potential will be there across the thickness of P(VDF-TrFE-CFE) terpolymer material as it is all about the electrostatics module. In this module, the electric potential is applied because the dipoles are arranged in the direction of the electric field, ultimately leading to a change in temperature. Heat transfer in the solid's module is discussed in detail to analyze the temperature. As depicted in Figure 2.1, In heat transfer in solids, whichever geometrical parts or block applies to heat transfer may be selected under the domain selection tab. The governing equation of this module is given equation 20. Reference temperature (T_{ref}) can be set as room temperature as 293.15 K, and the dependent variable is T. In the solid 1 tab, all the rectangular blocks are included except the air block. Since air is fluid, it can be included under the fluid tab. The initial value of all the domains is at room temperature, i.e., 293.15 K. The direction of the heat transfer is done only in the z-direction. So, rest all the sides except the top and bottom layers of an EC device are insulated, which can be provided by thermal insulation 1 tab. The top air layer is also at room temperature, i.e., 293.15 K. Now, the initial temperature of the battery/source is 313.15 K. This can apply to the battery/source block given by initial value values 2 tab. The battery/source temperature slowly decreases as the cycle progresses, and it cools down to room temperature.

Pyroelectricity is selected in the Multiphysics section, as shown in Figure 2.1, and is governed by equation 2.29. This module has coupled electrostatics and heat transfer interfaces in solids. The coupling type is set to electrocaloric, and the material's

pyroelectric coefficient is used. A user-controlled standard mesh can generate the mesh. Moreover, the supplied electric pulse is dependent on time and heat transfer also depends on time is considered. The time unit is taken as seconds in study settings, and the output time range should be set accordingly. The solution may not converge at a time slot, so the time slot needs to be set with smaller time steps. Tolerance can be set as user control with a relative tolerance limit of 0.1, and the rest of the settings should be physics-controlled. The return solution is not converged if the relative error exceeds the relative tolerance. In this case, the value of the relative tolerance should be increased to converge the solution. As depicted in Figure 2.1, In the results section, all data points have been stored in the dataset's node. Derived value has the option to observe the temperature of the selected domain probe. The table section contains related data that can be exported. The temperature and electric potential tab show the contour profile of the temperature and electric field. Any parameter, such as temperature, stress, displacement, etc., can be analysed by setting the prob plot expression. Following the modeling process, the model should go through sensitivity analysis, which is required in finite element analysis, to assure the reliability and correctness of simulation findings. By conducting mesh independence studies, we can ascertain that the solution obtained is not heavily dependent on the mesh density. As a result, the topic is further discussed.

2.4 Mesh-independent analysis and validation of the ECE

A mesh independence study is conducted to ensure that numerical simulations produce consistent results regardless of mesh size. It helps identify the optimal mesh resolution, balance accuracy and computational cost, ensure solution stability, and validate computational model reliability. In the first step, a mesh sensitivity analysis is carried out to find the optimum number of elements and to ensure the independence of results from the mesh elements. Figure 2.2(a) shows the electrocaloric material model with a side length (l) of 1 mm. The electrocaloric material substrate has a length, width, and height of 1.3, 1.3, and 0.05 mm, respectively. The geometry of the same dimensions was made using FEA software to validate the results. Equation-based modeling is used to validate this analysis. Here, the inner fiber of the cylinder is made of $BaTiO_3$, and the rest is PVDF. This model is used only for the validation of equation-based simulation results. Tetrahedral elements are used because the mesh can cover any 3D volume, regardless of shape or topology. Hence, it is used in the present analysis. The order of elements is quadratic, having 10 nodes per element, and the total degree of freedom is 498758. The

total elements are 183762 domain elements, 27540 boundary elements, and 3760 edge elements. The heat flux (Q) was calculated at a different number of mesh elements, and the Q was found to be converged at 200000 mesh elements, as shown in Figure 2.2. As a result, the model is independent of mesh density; however, validation must be performed to compare the model outputs to literature data.
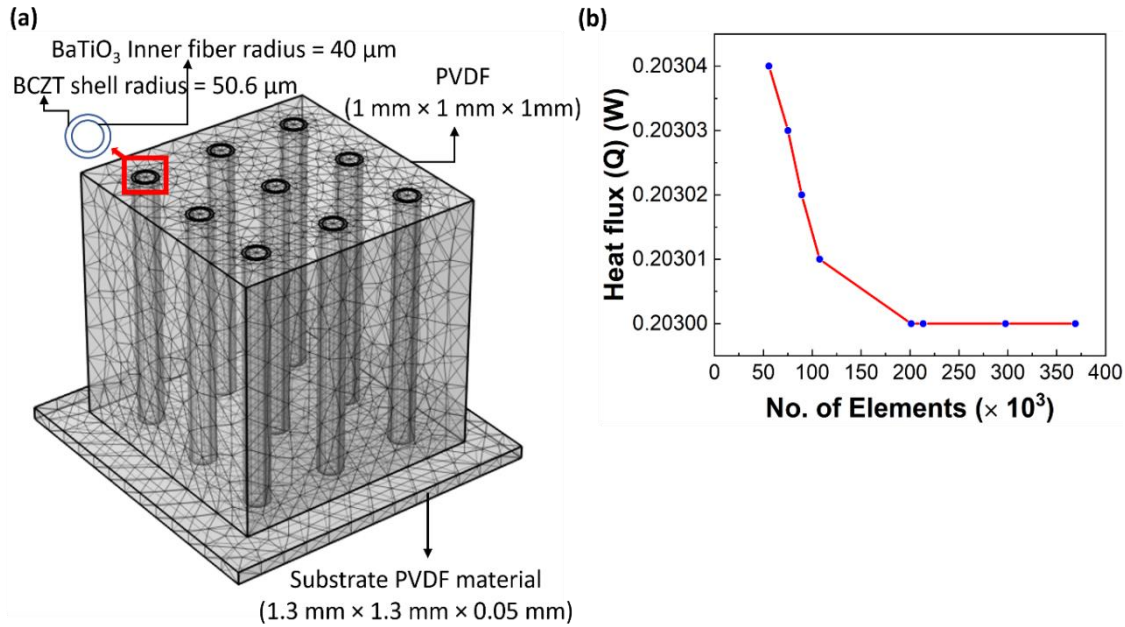
Figure 2.2. (a) Meshed geometry with dimension and materials used for equation-based model validation and grid-independent study. (b) Mesh-independent analysis for heat flux.

Figure 2.2(a) geometry and material validate the heat transfer module as specified in the literature[106]. Moreover, it assigns a specific material, such as PVDF, $BaTiO_3$, BCZT or BN. Equation-based modeling was done with an initial temperature of 298 K to investigate the heat transfer effect. The user-controlled mesh is generated with maximum/minimum element size, maximum element growth, curvature factor, and resolution of narrow regions at 0.15/0.024, 1.5, 0.6 and 0.5, respectively. A time-dependent study was carried out using physics-controlled tolerance. The main parameter to look for is the heat absorbed by electrocaloric material. Literature[106] has calculated the model's total heat absorption Qc, including all significant electrocaloric material properties such as thermal conductivity, density, specific heat, and coefficients C_1 and C_2. Figure 2.3 (a) depicts the electric field variation with time at the constant frequency of 1 Hz. In the first stage (i): 0-0.25 s, the applied electric field is 0. In the second stage (ii): 0.25-0.5 s, the applied electric field increases linearly till 100 MV/m; this increased

electric field leads to a change in entropy and thus produces the heat at this state, and the disordered dipoles get ordered. In the third stage, (iii): 0.5-0.75 s, the applied electric field remains constant at 100 MV/m. In the fourth stage, (iv): 0.75-1 s, the electric field decreases until zero. As the electric field falls, the dipoles become disordered again, thus changing the entropy and lowering the temperature.
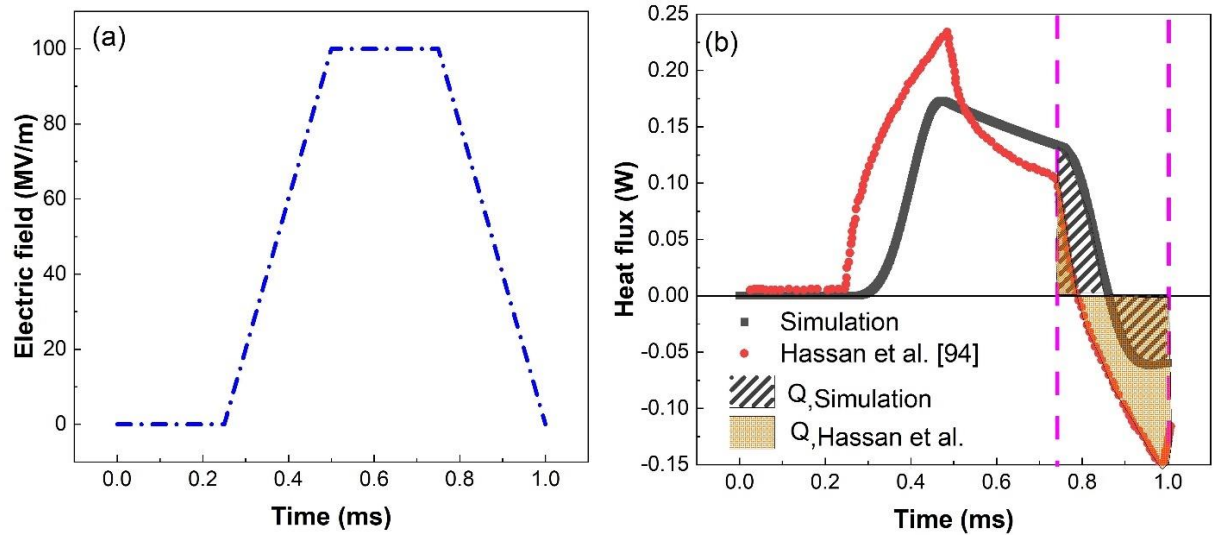
Figure 2.3. (a) ECE variation with time at the constant frequency of 1 Hz, (b) Heat flux (Q_c) is the total heat absorption of the electrocaloric material at 1 Hz.

The associated change in total heat flux is shown in Figure 2.3(b). The simulation model results align with those obtained by Hassan *et al*[106]. Thus, the present model equations can be used for further analysis of the ECE. In the process depicted in Figure 2.3(a), stage (iv), electrocaloric material absorbs heat (Q_c) from the substrate. Therefore, Figure 2.3(b) shows the electrocaloric material's output between 0.75 and 1 ms. The area under the graph depicted by the hatched area is approximately the same for both. This indicates that the equation-based modeling is successfully incorporated into the software and can be used to investigate the electrocaloric analysis. However, the inbuilt model validation is also performed considering the same geometry and parameter, providing a similar Q_c. Here, the comparison is made among three methods: S.G Lu *et al*[72], equation-based modeling, and in-built pyroelectricity module as described in Figure 2.4, and the corresponding ΔT_{ad} is 1.4, 1.78, and 1.9 K, respectively. The S.G Lu *et al*[72] ΔT_{ad} values consist of slight discrepancy with equation-based modeling and in-built pyroelectricity because S.G Lu *et al*[72] have insufficient geometrical dimensions of the film. The ΔT_{ad} of equation-based modeling and in-built pyroelectricity module is deviating because the

governing equation used in both models as equation-based modeling and in-built are governed by equations 2.26 and 2.30, respectively.
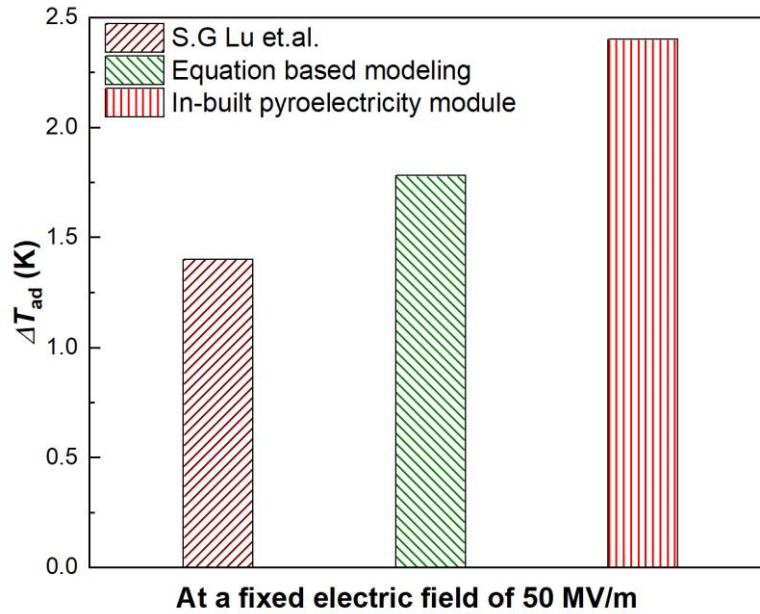
Figure 2.4. Comparison of adiabatic temperature change of an electrocaloric material among literature Lu *et al.* [72] equation-based modelling and built pyroelectricity module.

Equation 2.26 depends on coefficients C_1 and C_2, which further depends on entropy electric field variation, material, and its properties, which is difficult to find in the literature data for each material composition. Hence, the above equation concerning the material used and the applied–electric field is limited. Therefore, an alternate modeling approach with a pyroelectric coefficient (p_i) can be derived from Maxwell's relation, which is nothing but an inbuilt pyroelectricity module. As a result, there is little difference between the simulation modeling results and the literature data. The analysis also utilizes COMSOL Multiphysics software with its in-built pyroelectricity module. It is chosen for the rest of the analysis study (Chapters 3, 4, and 5) due to its user-friendly interface and controllable features, which offer a simpler alternative to manually inputting complex equations for investigating ECE. The model was checked with various mesh sizes and validated. One such validation of the in-built model is given in Chapter 3 (Figure 3.1).

2.5 Electric displacement validation

Now, the electrostriction effect can be used to move the ECE element between the heat source and sink. Thus, the material's electrostriction effect also needs to be validated. In

this direction, a large electric displacement is evaluated experimentally in 65Pb(Mg$_{1/3}$Nb$_{2/3}$)O$_3$-35PbTiO$_3$/Pt (65/35 PMN-PT/Pt) bimorph actuators[107]. The geometrical model dimensions are taken the same as given in the literature Figure 2.5(a) [107]: 18000 μm × 2500 μm × 60 μm. The 65/35 PMN-PT and platinum layer thickness are 50 μm and 10 μm, respectively. Rectangular blocks are used to build the geometry, as shown in Figure 2.5(b), and assigned materials such as PMN, gold, and platinum. The electrostriction and solid mechanics modules were used for analysis. The coupled interfaces in the module are solid mechanics and electrostatics, and the coupling type is polarization contribution to strain.
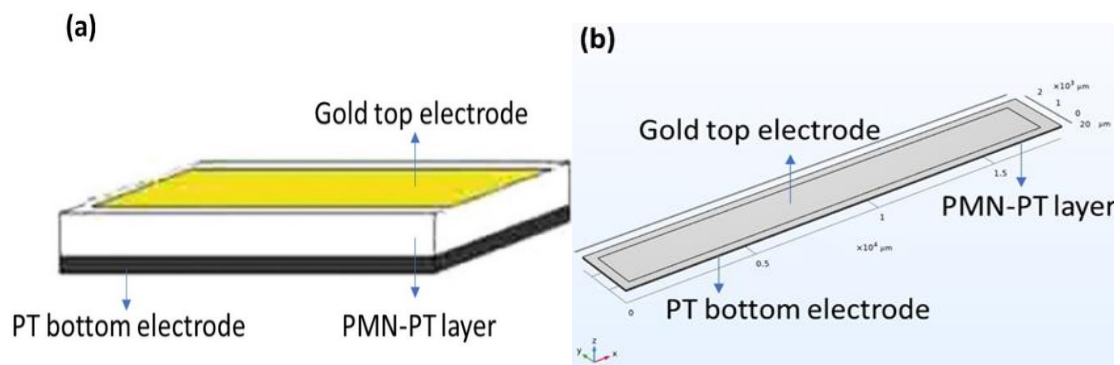
Figure 2.5. (a) Schematic diagram of 65/35 PMN-PT structure[107], (b) Geometry model of 65/35 PMN-PT structure used in analysis

An Electric Terminal in the range of 2.5 to 18 V is provided to the platinum strip and a gold electrode acts as a ground terminal. Material properties used to validate the model are given in Table 2.2. Additionally, a user-controlled mesh is generated to compute the results. The comparison of simulation modeling results and literature data on the displacement of the cantilever beam is discussed. The PMN-PT/Pt simulation study used the same geometry model and boundary conditions.

Table 2.2. Material properties used to validate the model.

Property	Platinum	Gold	65/35 PMN-PT
Density (kg/m^3)	21450	19300	7950
Relative permittivity	1	1.03	6000
Young modulas (GPa)	172	70	90
Poisson ratio	0.39	0.44	0.3

The validation graph of the 65/35 PMN–PT/Pt actuator's displacements versus the applied DC electric is shown in Figure 2.6. The shape of the displacement curve versus the

applied field indicates that two contributions from the electromechanical coupling are present, i.e., the piezoelectric linear effect and the electro strictive effect. The displacements were achieved ~100 μm at 18 V with dimensions of 1.8 cm × 2.5 mm × 50 μm for the 65/35 PMN–PT layer. When the voltage level is low, simulation data agrees with the literature. However, when the voltage increases, the simulation modeling data deviates from the literature data because the geometrical dimensions of the electrode layer and some material attributes are not specified in the literature.
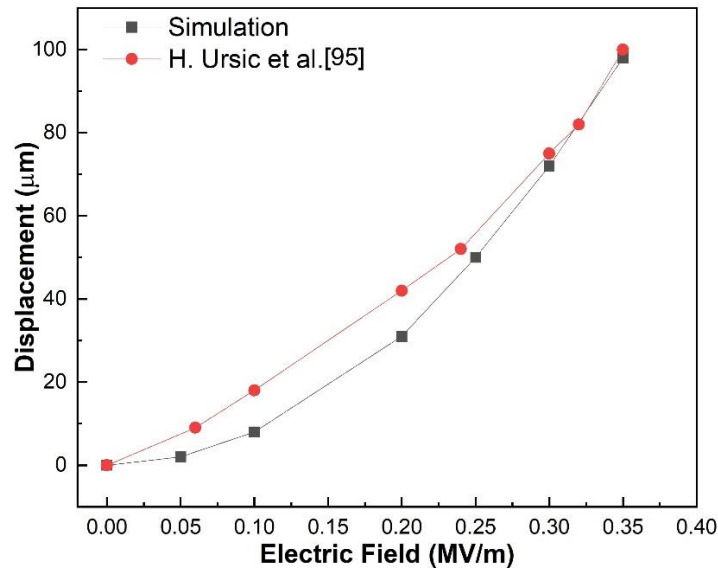
Figure 2.6. Comparison of the simulation modeling results and literature data.

2.6 Conclusions

This chapter used mathematical methodology to describe ECE modeling. Equation-based modeling mathematically depicts the ECE, which compares three methods for predicting the pyroelectric effect (ECE). It discusses the advantages of using the in-built pyroelectricity module in COMSOL Multiphysics, highlighting its straightforward interface and quick prediction of ECE. Model validation is conducted through mesh-independent analysis, revealing slight discrepancies compared to literature values due to unspecified electrode dimensions and material parameters. Equation-based modeling and the in-built module are compared, with the latter offering an alternative approach by deriving the pyroelectric coefficient from Maxwell's relation. Utilizing the in-built pyroelectricity module is recommended for more accurate analysis. This implies that the COMSOL Multiphysics modeling provides a solid foundation for further investigation into the ECE (details given in chapters 3, 4, and 5).

<div align="right">

Chapter 3

</div>

Effect of electric pulse and holding time on electrocaloric potential

In this chapter, the effect of electric pulse and holding time is analysed on the electrocaloric (EC) cooling potential of polyvinylidene fluoride-trifluoro ethylene-chlorofluoroethylene terpolymer (P(VDF-TrFE-CFE). The electrocaloric effect (ECE) depends on the electric pulse cycle, magnitude, and holding time. Thus, the impact of various electric pulses on ECE is studied. Similarly, the holding time also varied when investigating the ECE. The square electric pulse provides maximum ECE because of the fast application of the electric field and keeping the same electric pulse; the holding time is varied, and it is found to depend on material thickness and material properties. The electric field square cycles with 0.3 second holding provide the maximum EC temperature change. The magnitude of the electric field also varied, and the maximum adiabatic temperature of (P(VDF-TrFE-CFE) was obtained at 5.41 K at 100 MV/m. The results suggest that the types of electric pulse, magnitude, and holding time of electric pulse play a crucial role in obtaining maximum ECE at a given operating temperature.

3.1 Introduction

In the past decade, ECE has been determined in various materials and proposed for EC cooling devices[38]. Optimizing existing approaches, such as studying the impact of types of electric pulse on solid-state cooler efficiency, is also a key objective[124, 125]. Most EC research focuses on materials at phase transition temperatures, and indirect methods are used to measure temperature changes. Indirect measurements reveal temperature changes in EC, while direct measurements reveal the cycle form of the ECE due to applied electric fields[73]. In the dielectric model, entropy is proportional to the square of the electric field. This may be deduced from the LGD model by assuming polarization is proportional to the electric field[64]. However, the higher electric fields resulted in EC material's dielectric breakdown[76]. Thus, various electric signals can be used to enhance the ECE. In this direction, the step electric signal is commonly used, and it is symmetrical in terms of field application and switching off[21]. The step electric field and pulses' duration are chosen so that the samples can get into the thermal equilibrium with surounding[77]. The EC temperature change is observed near both the on and off slope[21]. Further, the triangular electric pulse form is also applied to thin ceramic film material at an electric field magnitude of 75 MV/m, but they do not have

any provided holding time[77]. Similarly, in another study, a step electric pulse form (170 MV/m) is used for thin polymer film with no holding time [72]. Moreover, a sinusoidal electric pulse (2.8 MV/m) at 298.15 K is applied to a thick ceramic film without holding time[64]. Starkov *et al.* [64] analyzed ECE cooler efficiency using sinusoidal and rectangular waveforms, finding a 74% efficiency with a frequency of 77.6 for $BaTiO_3$. The optimal waveform varied based on material dimension and holding time. Wang *et al.* [70] correlated a sharp increase in EC effect with temperature-electric field hysteresis loops, observing it with sine waveforms but a butterfly-shaped behavior with pulsed waveforms on PZT. Therefore, numerous available literature works have applied a step, sine, and triangular electric pulse. In contrast, they still need to thoroughly discuss the holding time and other forms of electric pulse effect on ECE. Thus, this chapter discusses an electric pulse/waveform, magnitude and holding time effect of ECE in polyvinylidene fluoride-trifluoro ethylene-chlorotrifluoroethylene terpolymer (P(VDF-TrFE-CFE)) (63.2/29.7/7.1 mol%) and concluding that the rectangular waveform yields the highest EC temperature change. The (P(VDF-TrFE-CFE)) consists of giant ECE and electro-strictive effect with higher room temperature dielectric constant, polarization (0.1 C/m^2), and electric breakdown field (> 400 MV/m)[10]. Further, modern ECE research strives to develop novel materials capable of producing large temperature differences when subjected to an electric field[27]. Thus, P(VDF-TrFE-CFE) was selected as an EC material for analysis in this work.

3.2 Effect of electric field magnitude

A material's adiabatic EC temperature change (ΔT_{ad}) is governed by equation 2.19, as discussed in Chapter 2. This chapter uses the in-built pyroelectricity model of COMSOL software for the EC analysis. It is observed that ΔT_{ad} is directly proportional to the change in an electric field. The effect of electric field magnitude on the ECE varies depending on the specific EC material and its properties. Generally, increasing the magnitude of the electric field tends to enhance the magnitude of the ECE. This is because a higher electric field strength results in a larger change in polarization or dipole orientation within the material, leading to a greater change in temperature. However, this relationship may not always be linear, and there may be optimal electric field strengths beyond which further increases do not significantly increase the magnitude of the ECE[126]. Additionally, excessive electric field magnitudes can lead to nonlinear effects or material degradation, impacting the effectiveness of the ECE[127]. Therefore, EC materials must have strong

dielectric strength to withstand large electric fields and achieve a high $\Delta T_{\mathrm{ad}[27]}$. The variation of the ECE with electric field strength is primarily influenced by the material's intrinsic properties and its response to external electric fields. Different EC materials have unique properties, such as dielectric permittivity, polarization behavior, and thermal conductivity. These properties show how the material responds to changes in the electric field. Therefore, the magnitude of the ECE can vary significantly from one material to another.

At lower electric field strengths, the polarization response of the material may be gradual and linear. As the electric field strength increases, the polarization response may become more nonlinear, leading to saturation effects or phase transitions that affect the ECE magnitude[128]. Some EC materials undergo phase transitions or structural changes in response to increasing electric field strengths[27]. These transitions can significantly alter the material's EC properties, resulting in nonlinear variations in the ECE magnitude. Excessive electric field magnitudes can lead to material degradation, such as breakdown[129]. Consequently, the ECE magnitude may diminish or exhibit unpredictable behaviour at high electric field strengths due to material instability[130].

The hysteresis effect can vary with the magnitude of the electric field and contribute to the overall variability in the ECE response[131]. Figure 3.1 shows the ΔT_{ad} as a function of applied electric field for various literature (experimental work) and equation-based modeling. A. Arvindhan *et al.* [132] and R. Ma *et al.* [102] used EC polymer stack material, as shown in Figure (3.1) inset (i) and inset (ii), respectively. However, S. Lu *et al.* [72] considered a similar model in the present analysis. All three pieces of the literature analysed ECE at 303.15 K; thus, similar results were used for Figure 3.1. Inset (i) and (ii) structures are taken for experimental measurement of the ECE. They found a maximum ΔT_{ad} of 3.5 K and 5.1 K at 99.7 MV/m and 83.2 MV/m, respectively. In the present analysis, P(VDF-TrFE-CFE) and gold (Au) are considered as the EC and electrode material (shown in inset (iii)), and a maximum ΔT_{ad} of 5.1 K is reached at 100 MV/m, which is comparable to experimental studies. Here, a square electric pulse is used for analysis with the holding time and equation (2.30) is used for analysis. The ΔT_{ad} is found as 1.25 K, 1.95 K, 2.6 K, 3.2 K, 3.8 K, 4.5 K and 5.1 K under an electric field of 20 MV/m, 40 MV/m, 50 MV/m, 65 MV/m, 80 MV/m, 90 MV/m, and 100 MV/m, by simulation as shown in Figure 3.1.
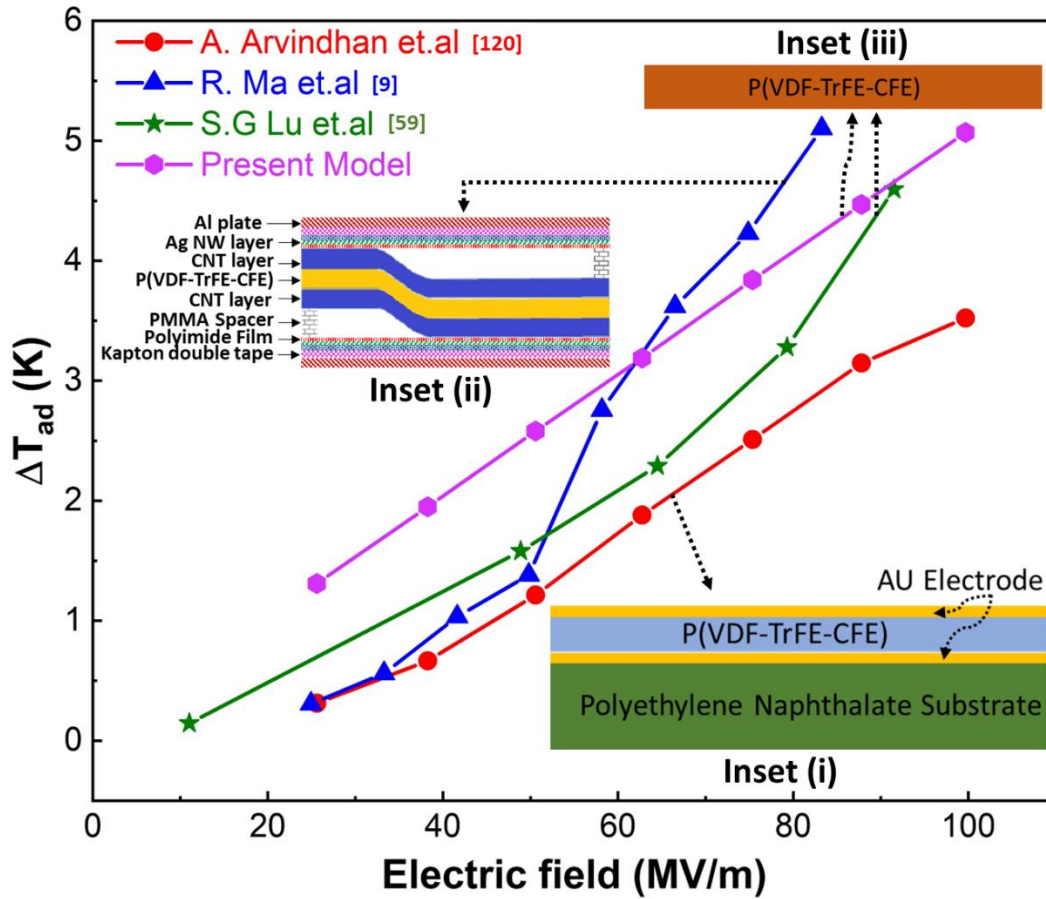
Figure 3.1. Comparison of ΔT_{ad} of P(VDF-TrFE-CFE) EC material as a function of an applied electric field.

The ΔT_{ad} varies linearly with the applied electric field, which agrees with equations 2.19 and 2.30, as shown in Figure 3.1. Here, it should be noted that the equations (2.4 and 2.15) do not accommodate any electric field-dependent phase transition; thus, they offer a linear behaviour only. Further, various studies on P(VDF-TrFE-CFE) suggest that the coercive field is less than or equal to 100 MV/m[133, 134]; thus, a maximum electric field of 100 MV/m is taken for the simulation. Moreover, at 100 MV/m, the present simulation model, using equation 2.30, provides nearly the same ΔT_{ad} measured experimentally; thus, it is used throughout the work. It should be noted that the electric pulse also affects the ΔT_{ad}. Therefore, ΔT_{ad} presented in Figure 3.1 can be varied according to the type of electric pulse and holding time, which is discussed in the next section.

3.3 Effect of types of electric pulse and holding time

The electric field is a crucial parameter for the ECE analysis, as seen from equation 2.19 and is directly proportional to ΔT_{ad}. Hence, electric field effect-based analysis is

performed on the P(VDF-TrFE-CFE) layer with a 7 cm × 3 cm × 0.01 cm. The top and bottom surfaces of P(VDF-TrFE-CFE) were electrodes using gold (thicknesses 0.1 μm). However, the electric pulse can be applied in various ways, such as sinusoidal, square, and triangle, with different holding times. The variation of different electric pulses on EC material temperature is shown in Figure 3.2. The simulation is performed at room temperature (293.15 K) and a fixed electric field of 100 MV/m. Figure 3.2(a), (b) and (c) shows the sinusoidal, triangle and sawtooth electric pulse, where the temperature profile of the EC material also changes according to an applied electric pulse.

The ΔT_{ad} for sinusoidal, triangle and sawtooth pulse is 0.79 K (293.15 K to 292.4 K), 0.52 K (293.15 K to 292.6 K) and 0.26 K (293.15 K to 292.9 K), respectively. Figure 3.2(d) shows the effect of holding time in a triangle pulse, where the P(VDF-TrFE-CFE) layer has a significant time to absorb the heat from the source material, resulting in increased ΔT_{ad} to 0.93 K (293.15 K to 292.2). When an electric field is applied, the temperature increases, and then an exponential decrease in temperature is observed at the applied (constant) electric field, as shown in Figure 3.2(d). It is associated with adiabatic polarisation and isofield heat transfer. Similarly, as the electric field is removed, the temperature falls, corresponding to the adiabatic depolarization phase, followed by the isofield heat transfer to reach the initial temperature and vice versa (see Figure 3.2(d)).

In a further modification, holding time is provided with a rectangular and slant-edge pulse, as depicted in Figures 3(e) and 3(f). The ΔT_{ad} of 0.52 K (293.15 K to 295.6 K) and 0.92 K (293.15 K to 292.2 K) were obtained for rectangular and slant-edge electric pulses, respectively. The last variation shows the combined effect of rectangular and slant edge pulse, where the electric field linearly increases (slant edge) and is kept constant for some time, and then decreases suddenly (sudden drop), as shown in Figure 3.2 (g). The ΔT_{ad} of the slant edge & sudden drop electric pulse is 3.63 K (293.15 K to 289.7 K). Figure 3.2 shows that EC ΔT_{ad} obtained in on/off conditions to find the asymmetry of ECE. The applied electric field can result in significant Joule heating after many EC cycles. To minimize the effect of the applied electric field, it is essential to provide sufficient time for EC materials to relax back to room temperature under the applied electric field. Hence, from all the electric pulses in Figure 3.2, the electric pulse with holding time (i.e., Figure 3.2(g)) is chosen as the most suitable electrical pulse due to enhanced ΔT_{ad} and adequate electrical pulse holding time. However, it is observed from Figure 3.2(d), (e), (f) and (g) that holding time affects the ΔT_{ad}.
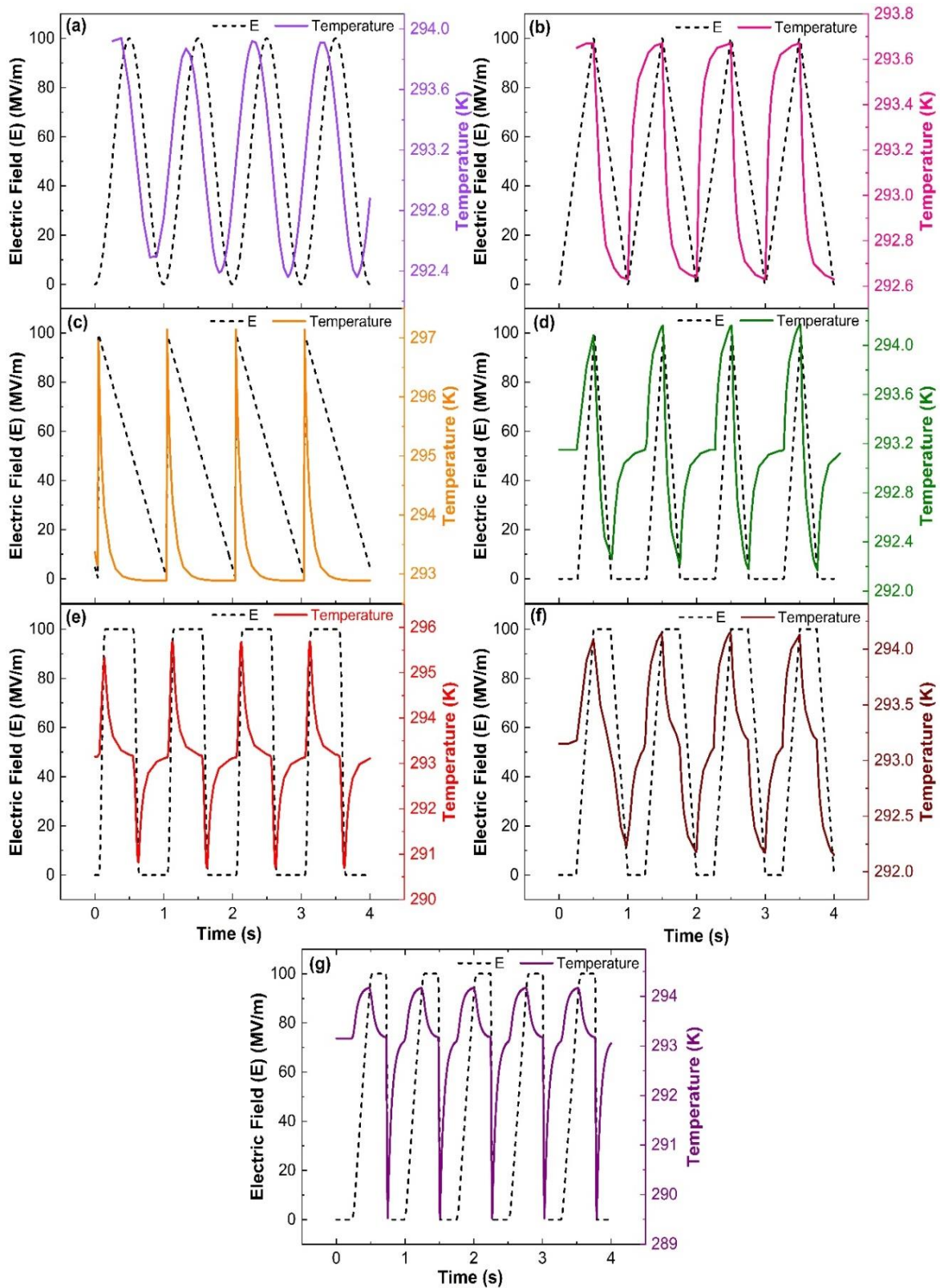
Figure 3.2. Different pulses of the electric field used during the ECE estimation, the electric signal in the form of (a) Sinusoidal, (b) Waveform triangle, (c) Sawtooth, (d) Triangle withholding time, (e) Rectangular, (f) Slant-edge and (g) Slant-edge & Sudden drop.

Thus, the variation in holding time is discussed in Figure 3.3. In Figure 3.3, the holding time is considered half compared to the previous analysis (Figure 3.2) to increase the operation frequency and reduce the total time to cool down the source. The change in ΔT_{ad} is 1.3 K, 2.2 K, 1.5 K, 3.5 K, and 4.9 K for different electric pulses shown in Figure 3.3 (a), (b), (c), (d), and (e), respectively. It is observed that the change in ΔT_{ad} obtained in Figure 3.3 is more than in Figure 3.2 because of the half reduction in holding time. The electric pulse illustrated in Figure 3.3(a) and (b) has the same slope when the electric pulse is applied and removed with and without holding time. However, Figure 3.3(b) shows better cooling due to holding time. Figures 3.3 (c) and (d) demonstrate a favorable impact due to the lower slope.
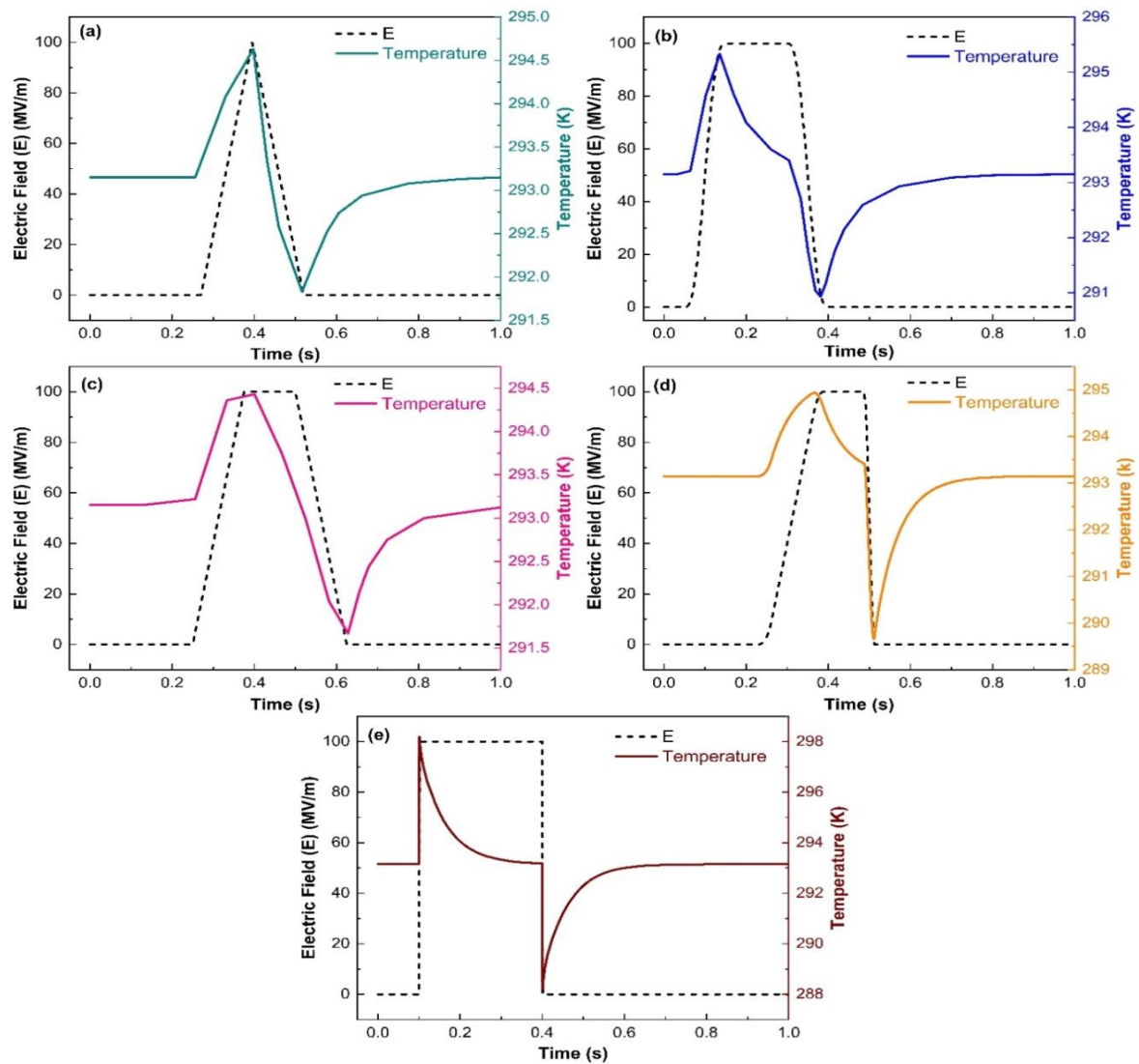
Figure 3.3. Temperature changes correspond to an Electric pulse in the form of (a) Triangle, (b) Rectangular, (c) Slant-edge, (d) Slant-edge & sudden drop and (e) Square with sudden increment & decrement.

The electric pulse should be applied and removed as quickly as feasible to achieve the maximum ECE. These suggestions were carefully reviewed and implemented, as seen in Figure 3.3(e). The holding of the electric field allows the sample temperature to return to room temperature (i.e., thermal relaxation time). The entire duration of holding time can be divided into three categories: (i) holding time (t_h) is more than thermal relaxation time (t_r), (ii) holding time is equivalent to thermal relaxation time, and (iii) holding time is much lesser than thermal relaxation time. When $t_h > t_r$, the long pulses result in the sample being exposed to a very high electric field for a longer duration. This exposure results in the dielectric breakdown of the material after a few cycles[21]. Further, when $t_h \sim t_r$, the EC material cools to room temperature, and the maximum ECE effect is obtained. However, when $t_h < t_r$, the sample does not get enough time to cool down to room temperature, and the on and off electric field spikes start to interfere, i.e., they start to cancel each other and minimal ΔT_{ad} is found[21]. The electric pulse shown in Figure 3.3 (e) $t_h \sim t_r$) gives the highest temperature change of 4.9 K due to the ECE. Moreover, the short pulse can also be used to anneal the frozen-in stresses of sample[21]. The following analysis can explain the effect of holding time.

The electric field variation is considered a rectangular waveform in which cycle time and electric field are denoted by abscissa and ordinate, respectively. The analysis employs an electric field magnitude of 20 MV/m, considered arbitrary. The primary focus lies in observing the effect of holding time exclusively. The time the EC layer is in contact with a heat sink (ambient) under a constant electric field is called holding time. From 0 to 0.1 sec, the EC layer is in touch with the heat source (battery), and an electric field is zero in that time duration, as depicted in Figure 3.4 (a). Moreover, the electric field gradually increases from 0.1 to 0.101 sec. After that, from 0.101 to 0.2 sec, the EC layer is in contact with the heat sink (ambient) and the electric field is kept constant. The electric field gradually decreases in the interval of 0.2 to 0.201 seconds. In the 0.201 to 0.6 sec interval, the EC layer is in contact with the heat source (battery) and an electric field is zero. The process of an electric waveform is the same in all four figures (3.4(a), (b), (c) and (d)) with a change in holding time. The holding time is approximately 0.1 sec, as seen in Figure 3.4 (a).

Similarly, the holding time of Figure 3.4 (b), (c), and (d) is 0.2, 0.3, and 0.4 seconds respectively. Variations are performed to check the adequate ECE holding time. The ΔT_{ad}

is the highest temperature change achieved in a given EC material and electric field, as depicted in Figure 3.5. The corresponding temperature change is shown in Figure 3.5.
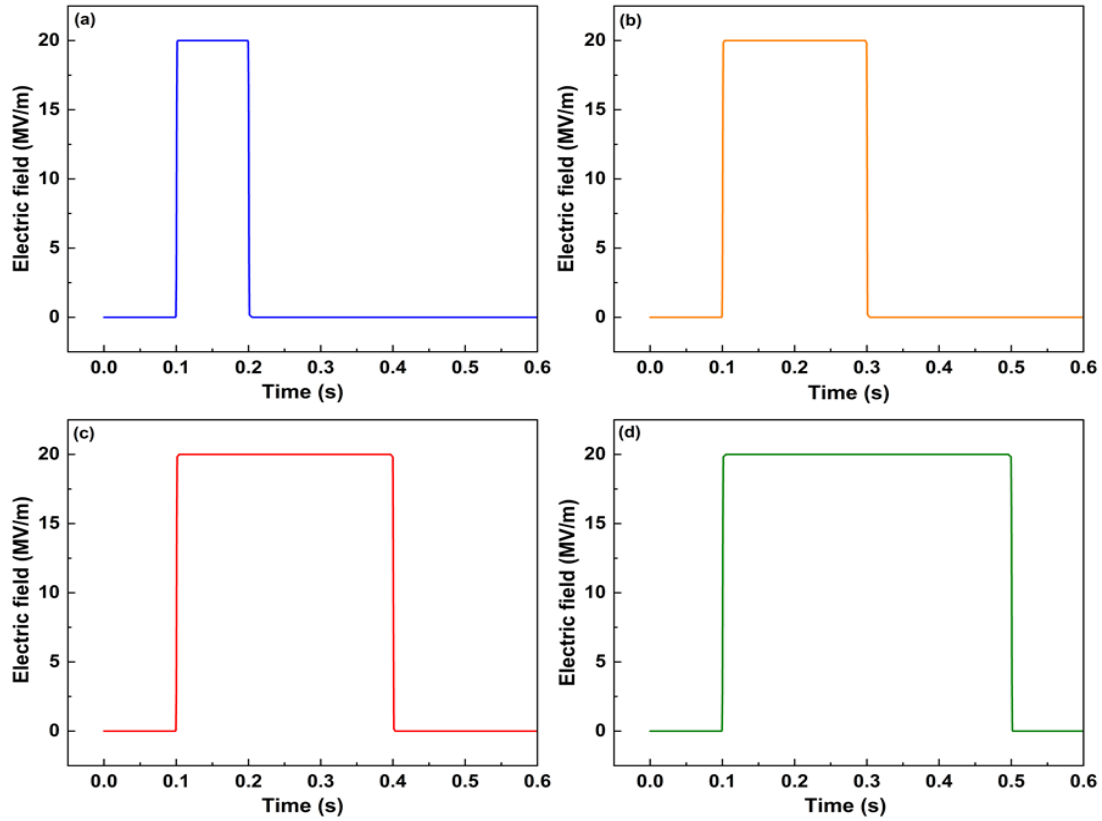
Figure 3.4. The applied electric field (20 MV/m) as a function of time with a variation of holding time (a) 0.1 s, (b) 0.2 s, (c) 0.3 s, and (d) 0.4 s when EC layer temperature is kept as a heat sink (ambient).

The change in adiabatic temperature corresponding to the applied electric field in Figure 3.4 (a) is depicted in Figure 3.5 (a). From 0.1 to 0.101 sec, the dipoles of EC material are aligned in the direction of the electric field and the material becomes more polar ordered. It reduces the entropy associated with polarization and compensates by increasing temperature. Hence, the temperature of the EC material has increased from 293.15 K (room temperature) to 293.55 K, as shown in Figure 3.5 (a). EC material releases heat to the sink (ambient) at a holding time, lowering the temperature from 293.55 K to 293.22 K, above room temperature. Further, the applied electric field fell to zero, then the temperature of the EC material reduced below the room temperature. Here, the temperature drops from 293.22 K to 292.76 K, and the adiabatic temperature change of EC (ΔT_{ad}) is 0.46 K (293.22 K - 292.76 K = 0.46 K) under 20 MV/m as given in Figure 3.4(a). It should be noted that the room temperature is 293.15 K; hence, effective ΔT_{ad} is

0.39 K (293.15 K - 292.76 K = 0.39 K) instead of 0.46 K under 20 MV/m. However, if sufficient holding time is given, it reaches 293.15 K (room temperature), then ΔT_{ad} of 0.46 K can be achieved.
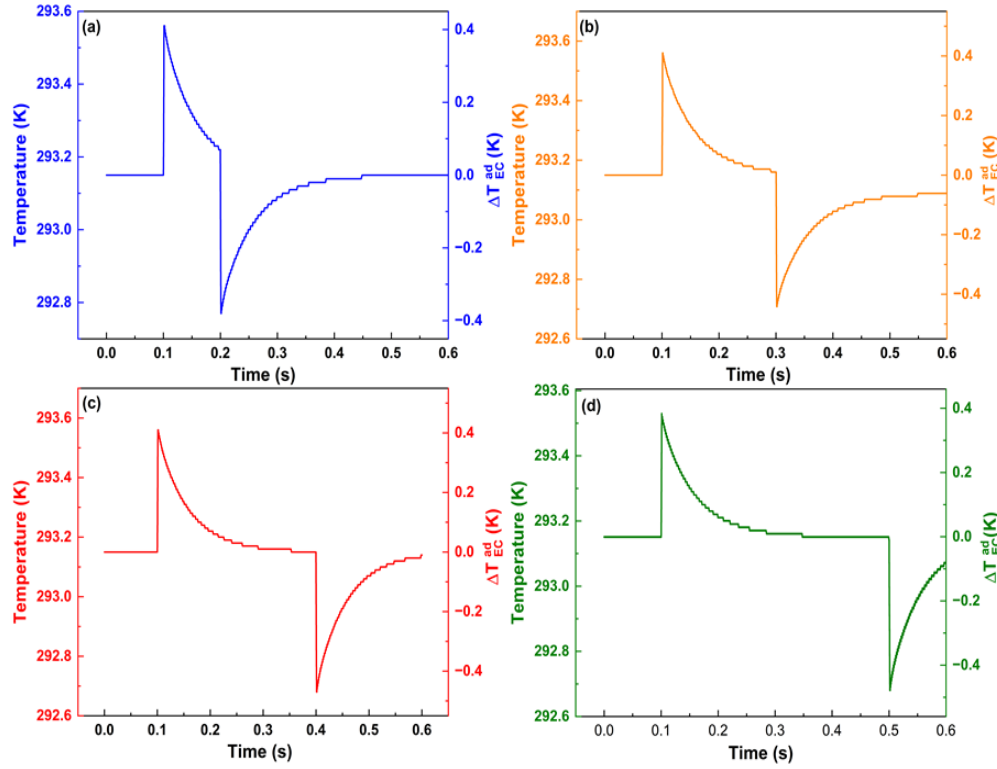
Figure 3.5. The change in adiabatic temperature of electrocaloric material corresponds to the applied electric field (20 MV/m.) in Figure 3.4 with a variation of holding time (a) 0.1 s, (b) 0.2 s, (c) 0.3 s, and (d) 0.4 s. It is assumed that the electric field is applied adiabatically.

Thus, the holding time is increased from 0.1 to 0.2 seconds, as shown in Figure 3.5(b). Suppose a holding time of 0.2 seconds is used. In that case, EC material releases heat to the sink (ambient), which lowers the temperature to 293.17 K. Thus, the temperature change ΔT_{ad} is 0.46 K (293.17 K - 292.71 K = 0.46 K), here the temperature slightly above the room temperature. Hence, the effective ΔT_{ad} is 0.44 K (293.15 K - 292.71 K=0.44 K). The problem with the above two cases, Figure 3.5 (a) and (b), is whenever the EC material releases the heat to the sink (ambient) at that point due to insufficient holding time, it can't be able to cool down to room temperature and ultimately decreases effective ΔT_{ad}. EC material must be cooled down to room temperature to get maximum ΔT_{ad}. Therefore, in Figure 3.5 (c), the holding time is further increased to 0.3 sec, where the EC material releases heat to the sink (ambient) and reaches the room temperature 293.15 K.

Now, the electric field is removed, temperature decreases from 293.15 K to 292.68 K. The ΔT_{ad} is approximately 0.47 K (293.15 K - 292.68 K=0.47 K). Thus, it can be said that to obtain effective ΔT_{ad} under 20 MV/m, a 0.3 second holding is needed; Figure 3.5(c) cycle is recommended. However, the holding time is further increased to 0.4 sec, as shown in Figure 3.5 (d). The EC material cools down to room temperature and remains at room temperature (293.15 K) for some time due to provided excess holding time, which is not required. The effective ΔT_{ad} in this case is also the same as observed in Figure 3.5(c). Hence, whenever EC material cools to room temperature under an applied electric field, it should be removed for a better cycle frequency. The excess holding time decreases the heat transfer frequency. In summary, Figure 3.5(c) shows that the electric field cycle gives the effective ΔT_{ad} with better cycle time; thus, the same is used for further analysis. Initially, the applied electric field magnitude is considered as 20 MV/m. The effect of the applied electric field is analyzed to the maximum possible ECE. Thus, a temperature change is recorded by varying the magnitude of the applied electric field, as depicted in Figure 3.6. Here, it should be noted that the equation-based modeling is used to see the electric field magnitude effect in Figure 3.6. This is because the in-built model used the Maxwell relation, which provides a linear increment of EC with an electric field, as shown in Figure 3.1. However, experimentally, it is observed that P(VDF-TrFE-CFE) consists of nonlinear behavior with applied electric field[8]. Thus, the equation-based model is considered, and results are compared with the in-built model. Figure 3.6 (a), (b), and (c) shows the variation of electric field and adiabatic temperature change over time. The-ΔT_{ad} of P(VDF-TrFE-CFE) is found as 0.47 K, 1.85 K, and 5.41 K under an electric field of 20, 50 and 100 MV/m, respectively, as depicted in Figure 3.6(a), (b) and (c), respectively. The ΔT_{ad} increases with the applied electric field, as seen by equation 2.19. The ΔT_{ad} as a function of the applied electric field is plotted in Figure 3.6(d).

It is assumed that the electric field is applied adiabatically. The maximum ΔT_{ad} obtained under an electric field of 100 MV/m is 5.41 K and 4.91 K by equation-based modeling and inbuilt pyroelectricity modeling, respectively. The built pyroelectricity module yields a slightly lower ΔT_{ad} of 0.5 K than the equation-based modeling approach. This discrepancy arises from utilizing two distinct methods: equation-based and inbuilt pyroelectricity modeling. However, an inbuilt pyroelectricity module is used for further analysis because of the complexity of determining coefficients for different materials in equation-based modeling. Hence, further heat transfer analysis of 100 MV/m electric field

is used for the simulations, as shown in Figure 3.6 (c). The holding time (cycle time) can vary slightly for the 100 MV/m; T_{ad} of 5.41 K requires more time to release and absorb heat from the sink and source, respectively. Many researchers also use a similar electric field magnitude (100 MV/m) for EC analysis.
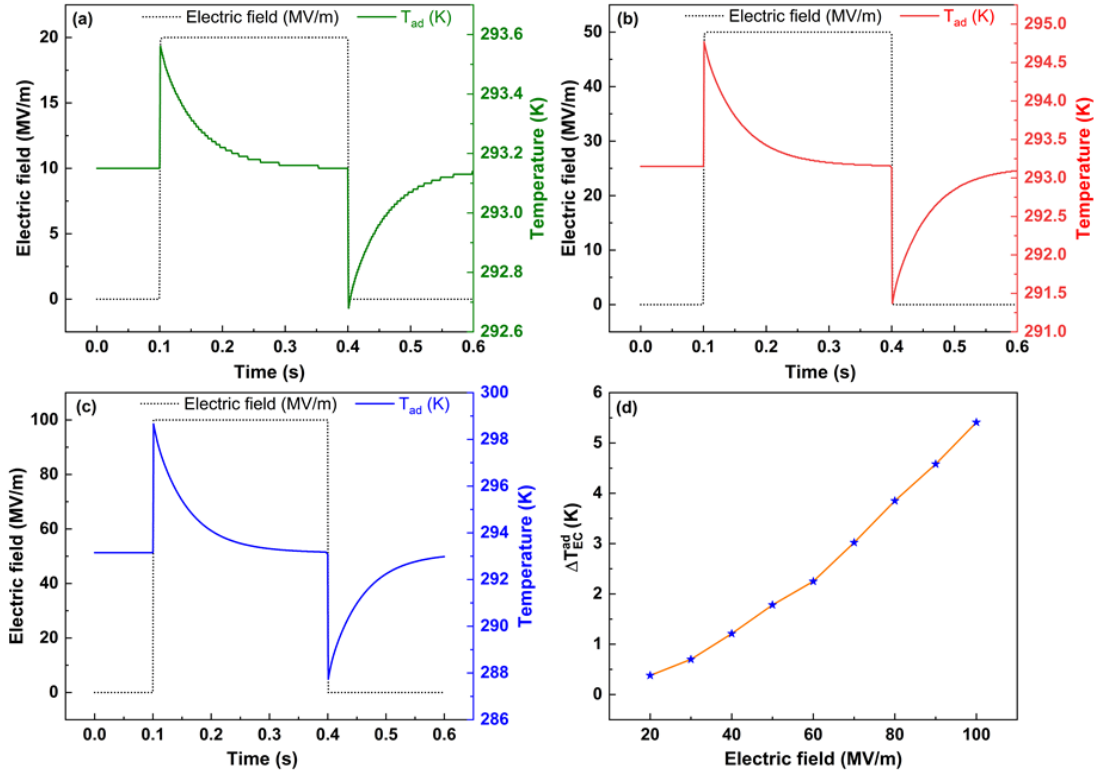
Figure 3.6. Effect of applied electric field on temperature change due to ECE versus time at (a) 20 MV/m, (b) 50 MV/m, and (c) 100 MV/m. (d) change in temperature concerning the electric field when the ambient temperature is kept at 293.15 K during simulation.

Therefore, the electric pulse and its holding time play a vital role in increasing the magnitude of EC and annealing the thin film for EC applications. In this regard, previous work done by Starkov *et al.* [64] used sinusoidal and rectangular waveforms to analyse ECE cooler efficiency. They found that sinusoidal waveforms with a frequency of 77.6 have a relative efficiency of 74% in single-layer BaTiO₃. However, the optimum waveform changed according to the material dimension and waveform holding time. Moreover, Wang *et al.*[70] measured polarization-electric field (*P-E*) hysteresis loops at various temperatures to correlate with a sharp increase in ECE. They used sine and pulsed electric waveforms for direct EC measurement and found that the temperature-electric field hysteresis loop is observed when a sine waveform is used[70]. Conversely, the pulsed waveform applied on PZT shows a butterfly-shaped behavior. However, other

electric waveforms are considered in the present work. It is found that the rectangular waveform is the most optimum waveform with maximum EC temperature change. The effect of different electric pulse forms on ECE with various parameters is given in Table 3.1. P(VDF-TrFE-CFE) has the highest EC temperature change compared to ceramics. For the present analysis, a rectangular step pulse with an electric field of 100 MV/m is used to avoid dielectric breakdown. It is far below the dielectric breakdown strength of thin film P(VDF-TrFE-CFE)[76]. Further, the span time of electrical pulses is significantly longer than the external thermal relaxation time, allowing the sample temperature to be relaxed back to the bath temperature. Hence, a square with sudden increment & decrement pulse can be used. Furthermore, rectangle/square electric waveform is mainly used in literature (see Table 3.1), and the same is considered in this work. Table 3.1 suggests that the chosen electric waveform, holding time, and ΔT_{ad} of the current work are better.

According to the preceding discussion, the square type of electric field pulse is best. However, the holding time should be optimized based on the geometry dimensions and material properties. The effect of materials parameters on ECE considering the square waveform is discussed in Chapter 4. The optimized electric field square pulse three-cycle profile is depicted in Figure 3.7. This square electric pulse consists of 100 MV/m with a holding time of 0.3 seconds and is used for further analysis (Chapters 4 and 5).
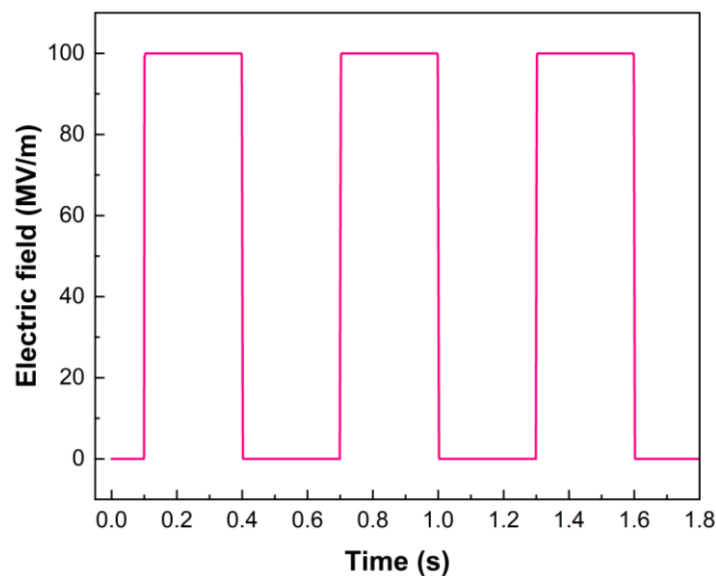
Figure 3.7. The optimized square electric field pulse with a maximum magnitude of 100 MV/m for three cycles.

Table 3.1. Comparing the effect of different electric pulse forms and other properties on electrocaloric.

Material	Material type	thin/bulk/ thick	Pulse form	thickness (mm)	Operating temperature (K)	Voltage (MV/m)	ΔT_{ad} (K)	Holding time (s)	Reference
PZT-5	Ceramic	Thick	Square	0.5	298.15	1.8	0.28	-	[64]
PZT-5	Ceramic	Thick	Sinusoidal	0.5	298.15	2.8	0.15	-	[64]
PZT-5	Ceramic	Thick	Square	0.5	298.15	2.8	0.4	-	[64]
BaTiO$_3$	Ceramic	Thick	Square	0.5025	-	2.8	0.4	5	[70]
P(VDF-TrFE) 55/45 mol %	Polymer	Thin	Square	0.006	340.15	120	12	-	[72]
BaTiO$_3$	Ceramic	Thick	Square	0.5025	-	2.8	0.45	10	[70]
PMN-13% PT ceramic	Ceramic	Bulk	Rectangular	-	303.15	2.4	0.3	6.2	[76]
PMN	Ceramic	Bulk	Step	0.08	289	9	2.5	-	[68]
0.65 PMN 0.35 PT	Ceramic	Thin	Triangular	0.00024	413.15	75	31	0	[77]
P(VDF-TrFE-CFE) + 5 wt % of P(VDF-CTFE)	Polymer	Thin	Step	0.004 to 0.006	-	170	12	-	[72]
P(VDF-TrFE-CFE)*	Polymer	Thin	Triangular	0.1	293.15	100	0.93	0.5	Present
P(VDF-TrFE-CFE)*	Polymer	Thin	Sinusoidal	0.1	293.15	100	0.79	-	Present
P(VDF-TrFE-CFE)*	Polymer	Thin	Sawtooth	0.1	293.15	100	0.26	-	Present

									work
P(VDF-TrFE-CFE)*	Polymer	Thin	Waveform triangle	0.1	293.15	100	0.52	-	Present work
P(VDF-TrFE-CFE)*	Polymer	Thin	Rectangular	0.1	293.15	100	0.52	0.5	Present work
P(VDF-TrFE-CFE)*	Polymer	Thin	Slant-edge	0.1	293.15	100	0.92	0.25	Present work
P(VDF-TrFE-CFE)*	Polymer	Thin	Slant edge & sudden drop	0.1	293.15	100	3.63	0.25	Present work

*P(VDF-TrFE-CFE) (63.2/29.7/7.1 mol %)

3.4 Conclusions

The electric field pulse (sinusoidal, waveform triangle, sawtooth, triangle withholding time, rectangular, slant-edge and slant-edge & sudden drop) has been used to get the maximum ECE. The rectangular electric pulse form provided the highest ECE. Therefore, the electric pulse associated with the rectangular pulse and the change in holding time are also studied. The holding time of electrical pulses is chosen to be significantly longer than the external thermal relaxation time, allowing the relaxing of the sample temperature back to the bath temperature. Thus, an optimum holding time of 0.3 seconds in square waveform provides the maximum EC temperature change. The optimized electric pulse and holding time are kept constant, and the magnitude of the electric field is varied from 10 to 100 MV/m. The maximum adiabatic temperature of an EC material is obtained as 5.41 K at μMV/m by square with sudden increment & decrement electric pulse. The square electric pulse of 100 MV/m with a holding time of 0.3 seconds is used for further analysis.

<div align="right">

Chapter 4

</div>

Effect of operating temperature, electrode, and substrate materials on electrocaloric potential

The present chapter discussed the effect of operating temperature, electrode, and substrate materials on the electrocaloric effect (ECE). The operating temperature is crucial since temperature changes substantially impact the performance of cooling systems. The simulation study also addresses the impact of electrode/substrate thickness and material on the ECE. Further, thermal contact resistance between various layers is considered, as it is vital to efficiently regulate heat flow between the electrode material and the device. Thermal contact resistance is considered based on data from experimental literature to analyse the ECE. The gold (0.1 μm thick) and aluminium (100 μm thick) are found to be better electrode and substrate materials, respectively, at an optimal working temperature of 293.15 K.

4.1 Introduction

The operating temperature considerably impacts adiabatic temperature change (ΔT_{ad}). The electrocaloric effect (ECE) ΔT_{ad} is directly proportional to operating temperature, as in equation 2.19 (Chapter 2). Researchers investigate temperature-dependent features and their effects on the ECE. The ΔT_{ad} in P(VDF-TrFE-CFE) film at different temperatures under a 100 MV/m field is studied[132] . As the operating temperature range rises from 285.9 to 303.1 K, the change in ΔT_{ad} is observed on the P(VDF-TrFE-CFE) (64.8/27.4/7.8 mol %) polymer film increases from 2.138 to 3.6 K [132]. Similarly, the change in ΔT_{ad} is seen from 0.16 to 0.39 K at operating temperature ranges from 320 to 380 K and an electric field range of 1 to 2.15 MV/m[128] . A peak ΔT_{ad} of 3.58 K occurred at 303 K, aligning with the peak of the permittivity's real part[135]. Guo *et al.[136]* studied P(VDF-TrFE-CFE) with limited temperature (293.15 – 313.15 K) and lower field (73 kV/m), observing no significant ΔT_{ad} surge, contrasting findings potentially due to the higher electric field near the permittivity peak. The suitable operating temperature for P(VDF-TrFE-CFE) film is near room temperature (293.15 – 313.15 K) [136]. Hence, the effect of operating temperature is also considered in this work. In addition to operating temperature, electrode and substrate materials are crucial in determining the optimal ECE. Therefore, further investigation into the impact of electrode and substrate materials is conducted to understand their effects. Using interdigitated top electrodes with Pt allows

the application of very strong electric fields in multilayer PST[137]. In another study, both faces 100 nm Au electrodes were sputtered to perform EC measurements[138]. Further, the multilayer capacitors (MLCs) with active $Pb(Mg_{1/3}Nb_{2/3})O_3$ layers around 38 μm thick and 1-2 μm Pd inner electrodes are used for ECE analysis [139]. Different electrode materials are available and used by researchers. However, they have not discussed the effect of electrode materials on the ECE. Hence, the impact of various electrode materials and their effects is discussed in this chapter. A substrate layer is required to support and improve heat transfer in the ECE device's freestanding film-based design. A proper substrate selection can effectively enhance the adiabatic temperature change for cooling or thermoelectric power conversion devices[140]. The $0.7Pb(Mg_{1/3}Nb_{2/3})O_3$-$0.3PbTiO_3$ is a substrate material to find ECE in $PbZr_{0.95}Ti_{0.05}O_3$ films[141]. The high-quality lead-free ferroelectric thin film Mn-doped $BaTiO_3$ on a SiN/p-GaN composite substrate and $Pt(111)/TiO_x/SiO_2/Si(100)$ substrates by the sol-gel method[142].

Therefore, the effect of the substrate materials on the ECE is not discussed, which is undertaken in this chapter. Finally, the contact resistance between the elements is a vital parameter determining the device's performance[143]. Bauer *et al.*[10] demonstrated thin polarization-electric field (P-E) hysteresis loops and low dielectric loss in elements. The existing literature has provided calculations for various losses individually. Yet, it lacks a comprehensive consolidation of all losses in a single study, which is also addressed in the present study.

4.2 Operating temperature effect on ECE

The operating environment of the EC material is not always at room temperature. Thus, the working temperature variation is considered in the EC material performance. Figure 4.1 shows the ECE in P(VDF-TrFE-CFE) material at different operating temperatures under an electric field of 100 MV/m. A square pulse is used for EC analysis, as discussed in Chapter 3. The effect of Joule heating is not found in the present analysis due to the optimized pulse. The ECE at an ambient temperature (298.15 K) is depicted in Figure 4.1(a). The EC (ΔT_{ad}) of 4.91 K is obtained during the cooling cycle operated at 298.15 K. However, it should be noted that losses are not deducted in Figures 4.1 - 4.4 to simplify the explanation and discussion. Similarly, Figure 4.1(b), (c), and (d) depict ΔT_{ad} of 5.3 K, 5.8 K, and 6.0 K when the operating temperature of P(VDF-TrFE-CFE) material is 318.15 K, 343.15 K and 363.15 K respectively. Figure 4.1(e) depicts the ECE ΔT_{ad} as a

function of operating temperature in P(VDF-TrFE-CFE) at an applied electric field of 100 MV/m.
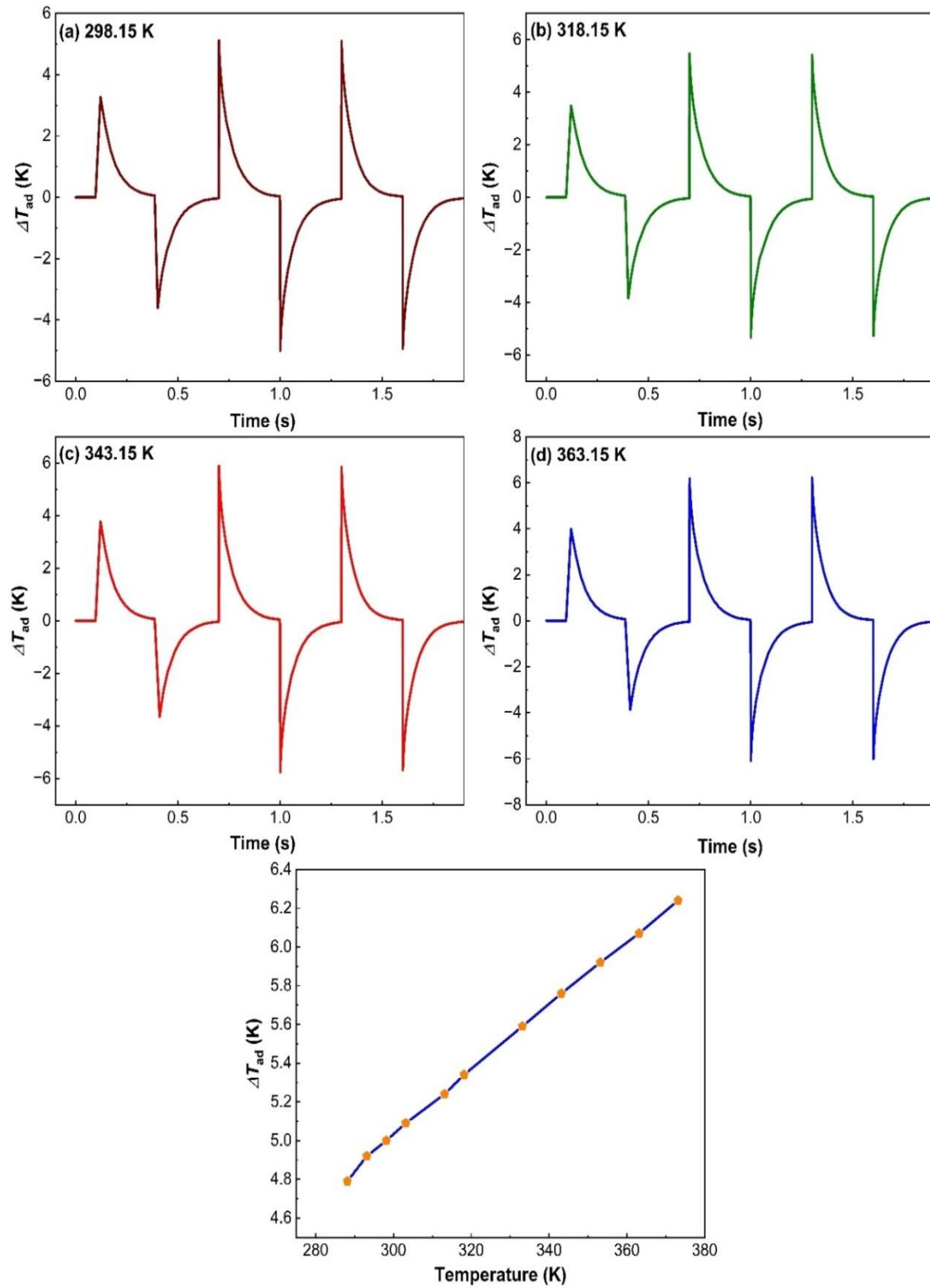

Figure 4.1. The EC ΔT_{ad} of P(VDF-TrFE-CFE) at operating temperatures of (a) 298.15 K, (b) 318.15 K, (c) 343.15 K, (d) 363.15 K and (e) ΔT_{ad} versus operating temperature under at 100 MV/m.

The ΔT_{ad} varies from 4.8 to 6.2 K as the operating temperature varies from 288.15 K to 373.15 K. The ΔT_{ad} increases linearly with temperature, as illustrated in Figure 4.1(e), supported by equations 2.19 and 2.30. Thus, it can be said that as the operating temperature increases, the ΔT_{ad} also increases. Here, it should be noted that the phase transition in the materials at a given temperature is not considered in equation 2.30 (chapter 2); hence, the same is not reflected in the ΔT_{ad}.

Therefore, equation 2.30 is used only for the linear behavior of the P(VDF-TrFE-CFE) properties with temperature. The variation of ΔT_{ad} of P(VDF-TrFE-CFE) with operation temperature is compared with well-known EC materials in Table 4.1. The ΔT_{ad} increases as the operating temperature increases, as given in Table 4.1. The equation 2.19 also suggests that as the operating temperature increases ΔT_{ad} also increases. The maximum ΔT_{ad} is obtained near the Curie temperature of the materials. P(VDF-TrFE-CFE) consists of large EC in the wide temperature range compared to ceramics and other polymer compositions.

Table 4.1. The operating temperature effect on ΔT_{ad} for EC material with literature data.

Material	Type	E-Field $(\frac{MV}{m})$	Operating Temperature (K)	ΔT_{ad} (K)	Reference
P(VDF-TrFE-CFE) (64.8/27.4/7.8 mol %)	Polymer film	100	285.9 to 303.1	2.138 to 3.6	[132]
$Ba_{0.85}Ca_{0.15}Zr_{0.1}Ti_{0.88}O_3$	Ceramic films	1-2.15	320 to 380	0.16 to 0.39	[128]
$Ba_{0.85}Ca_{0.15}Zr_{0.1}Ti_{0.88}Sn_{.02}O_3$	Ceramic films	3.2	353	0.84	[128]
$Ba_{0.7}Sr_{0.3}TiO_3$	Bulk Ceramics film	2.15-2.9	300 to 320	0.37 to 0.49	[144]
$Ba_{0.9}Sr_{0.1}TiO_3$	Bulk Ceramics film	2.15-3.3	360 to 370	0.31 to 0.51	[144]
$Pb(Zr_{0.9}Ti_{0.1})O_3$	Ceramic films	10	330	2.5	[145]
P(VDF-TrFE) (55/45 mol %)	Polymer film	134 - 209	353.15 to 373.15	5 to 12.5	[50]
P(VDF-TrFE-CFE)	Polymer film	100-	303.15 to 313.15	1.67 to	[50]

(59.2/33.6/7.2 mol %)			307		4.9	
$(Ba_{0.85}\ Sr_{0.15})\ (Zr_{0.1}Ti_{0.9})O_3$	Ceramic films	3	347		0.5	[146]
$Ba_{0.7}Sr_{0.3}TiO_3$	Bulk ceramic	3.3	303		0.67	[144]
$BaTiO_3$	single crystal	-	406		4.20	[147]
$PbZr_{0.95}Ti_{0.05}O_3$	Ceramic films	99	400		25	[148]
PZT-5	Polycrystalline ceramics	2.8	303		0.15	[70]
$Pb_{1-3x/2}La_xZr_{0.85}Ti_{0.15}O_3$	Thick film	90	303		7	[148]
P(VDF-TrFE-CFE) (63.2/29.7/7.1 mol %)	Polymer film	100	288.15 to 373.15	4.79 to 6.24	Present work

It should be noted that the EC (ΔT_{ad}) of 4.91 K is observed during the cooling cycle operated at 298.15 K, whereas (ΔT_{ad})$_{effective}$ is 4.01 K (when losses are considered) at 100 MV/m. Here, hysteresis (ΔT_{hys}) and electrode thermal contact resistance (ΔT_{tc}) loss are taken as 0.24 K (5%) and 0.54-0.66 (11-13.5 %) K, respectively (losses are discussed in the next section).

4.3 Electrode/substrate material and thickness effect on ECE

The ECE is obtained by applying an electric pulse, whereas P(VDF-TrFE-CFE) is a dielectric material, and an electric field cannot be directly applied to its surface. Thus, an electrode is needed to apply electric potential between the top and bottom surfaces of the P(VDF-TrFE-CFE). The material's characteristics (electrical conductivity) and thickness are expected to influence the EC performance.

Therefore, the eight most popular electrode materials, gold (Au), copper (Cu), palladium (Pd), silver (Ag), titanium (Ti), carbon nanotubes (CNT), aluminum (Al) and nickel (Ni) are considered for analysis, with variation in thickness from 0.01 μm to 10 μm, as shown in Figure 4.2. The EC ΔT_{ad} is observed for three successive cycles. The schematic diagram given in inset (i) of Figure 4.2(a) is used for simulation and consists of electrode coating on the top and bottom layers of the P(VDF-TrFE-CFE) layer. The electric potential is applied to the top electrode while the bottom layer remains in ground condition.

Figures 4.2(a) and 4.2(b) show the influence of different electrode materials on temperature change owing to the ECE. At all thicknesses from 0.01 μm to 10 μm, all materials provide roughly the same ΔT_{ad} due to small electrode thickness. However, in the practical application, a 0.01 μm thick electrode may not have uniform electrical conductivity; thus, a minimum 0.1 μm thick electrode should be used. Figure 4.2(b) compares the ΔT_{ad} for all electrode materials at various thicknesses.

In this regard, Ju *et al.*[149] also discussed that if electrode thermal conductivity increases, cooling power density also increases. At a fixed electrode thickness and given heat transfer time, the cooling power increases with increasing thermal conductivity. Still, the incremental benefit is reduced for sufficiently high thermal conductivity values. If it is above 130 W/mK, then the effect of thermal conductivity on cooling power density is negligible [149]. Similarly, Kar-Narayan *et al.* [150] have also shown the effect of electrode materials on multilayer capacitors-based EC cooling. Therefore, the electrode material effect on the EC is negligible (see Figure 4.2) due to their sufficiently high thermal conductivity values. However, a large difference in thermal conductivity is expected to vary ECE.
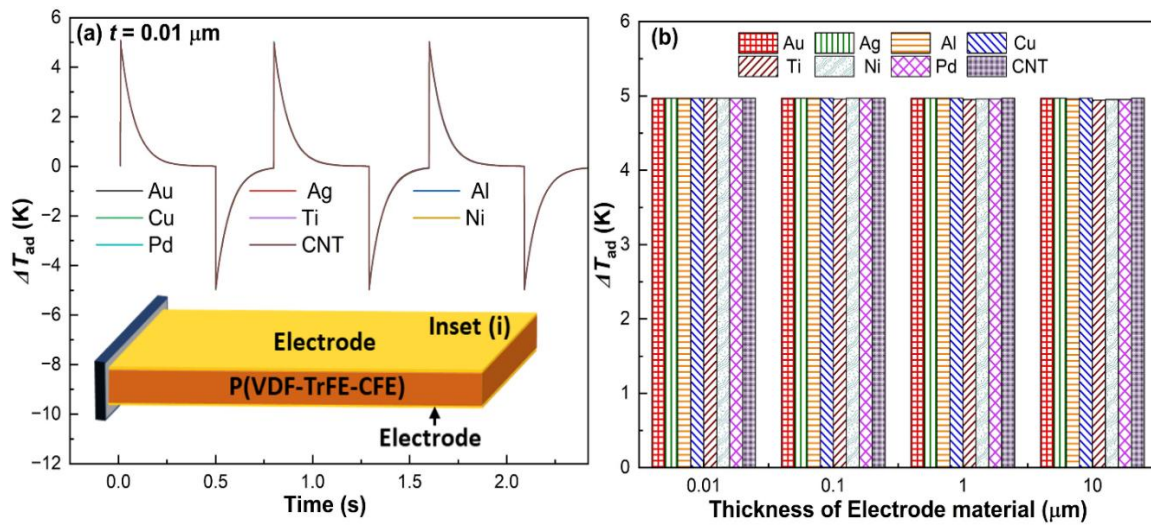
Figure 4.2. Effect on the EC ΔT_{ad} for different electrode materials and their thickness of (a) 0.01 μm, (b) Comparison of ΔT_{ad} of various electrode material thickness.

In addition, the effect of interfacial resistance also plays a vital role in the heat transfer between substrate/electrode and EC material. A material's thermal resistance (R) can be calculated as $R = x/(k \cdot A)$, where x is the thickness of the material, k is thermal conductivity and A is the surface area. The Au and CNT electrode materials' thermal conductivity is 314 and 6600 W/mK, respectively, with a length and area of 0.1 μm and

0.00021 m². The calculated thermal resistances for Au and CNT electrodes are approximately 0.1502 and 0.00721 µK/W, respectively. The change in ΔT_{ad} is negligible in thin electrodes due to the small resistance (order of ~10^{-6}). Thus, for the small thickness of electrode material (as 100 nm in the present analysis), Au and CNT have similar ECE. In the present EC device, the top Au/CNT layer and bottom substrate layer are in continuous contact with air and heat sources for heat rejection and absorption, respectively, and no switching takes place. However, heat transfers between Au/CNT and air (atmosphere) limit device efficiency. As discussed above, the CNT has lower thermal interface resistance than Au. Hence, CNT is always a better choice for practical application as an electrode material for maximum device efficiency due to the least thermal resistance. Ma *et al*. [8] also used carbon nanotube electrodes to reduce the interfacial thermal resistance. Therefore, in the present work, Au is used as an electrode because an Au electrode of 0.1 µm thick can be easily obtained by sputtering, which is highly durable, resilient, and corrosion-proof[151] . The Au-based sputtering electrode has the additional benefit of high melting points [152], does not oxidize [153] and low resistance [154]. In addition, Kar-Narayan *et al*. [150] showed that expensive materials are not required, and EC device performance can be enhanced via geometrical improvements.

A substrate layer is necessary for support and better heat transfer to the ECE device's freestanding film-based design. The ECE is demonstrated in Figure 4.3 considering different substrate materials (Al, brass, steel, polyethylene terephthalate (PET) and polydimethylsiloxane (PDMS)) and thicknesses (10 to 500 µm). The substrate materials are chosen based on their flexibility, heat capacity and low cost. Figure 4.3(a) illustrates the influence of substrate material on ΔT_{ad} with a thickness of 10 µm. Inset (i) of Figure 4.3(a) shows the EC device module used. Inset (ii) in Figure 4.3(a) provides a zoom-in portion of peaks, which makes it easier to understand the effect of substrate materials on ECE. As all insets demonstrate, polymers have the lowest ΔT_{ad} compared to metals since polymers are covalently bonded materials and metals are metallic bonded materials. As a result, covalent bonds do not let atoms exchange electrons as metallic bonds [155]. Therefore, polymers have a higher heat capacity than metals. The highest ΔT_{ad} of 4.97 K is achieved in the Al substrate. The thickness of the substrate material is increased to 50 µm, 100 µm and 500 µm, and the effect on EC is presented in Figure 4.3(b), (c) and (d), respectively. Insets of Figures 4.3(b), (c) and (d) show that PDMS and PET consist of the

approximately same ΔT_{ad}. Further, as substrate thickness increases to 500 μm, the Al substrate has the highest ΔT_{ad} among all substrate materials (see Figure 4.3(d). The ΔT_{ad} of the EC device is reduced with increasing substrate material thickness, as seen in Figure 4.4.
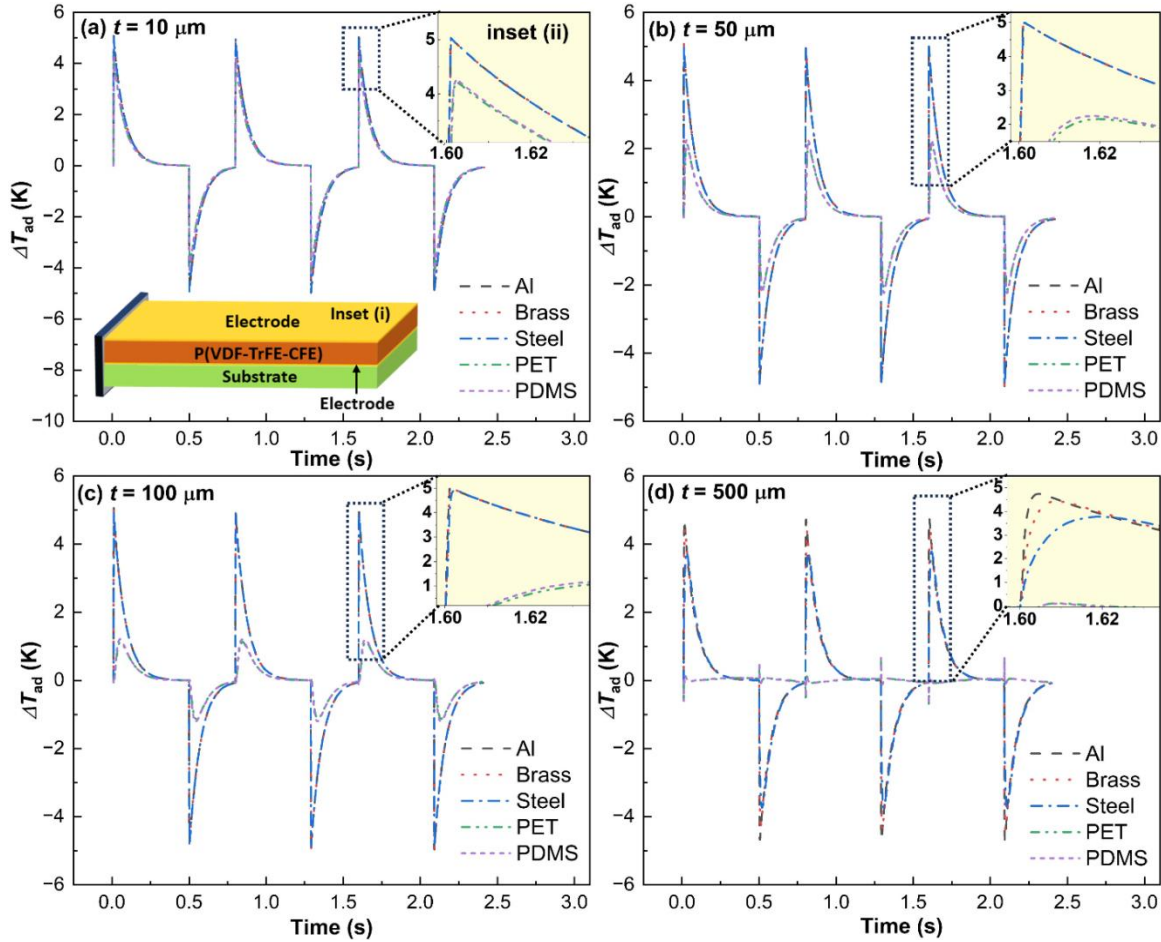
Figure 4.3. Substrate thickness and material effect on EC ΔT_{ad} at an electric field of 100 MV/m when substrate thickness is (a) 10 μm, (b) 50 μm, (c) 100 μm, and (d) 500 μm.

This can be explained by considering the heat (Q_{ec}) associated with ΔT_{ad} is given by,

$$Q_{ec} = mc_p\Delta T_{ad} \tag{4.1}$$

where m and c_p are the EC material's mass and specific heat capacity. This heat flux is transferred to electrode material having a thickness of 100 nm; therefore, the electrode material's associated heat loss is small. Assuming the heat flux loss through the electrode is negligible, temperature across the electrode can be considered the same as EC material ΔT_{ad}. In this regard, the variation of temperature of the substrate due to heat flux generated by EC material can be given by (considering the 1D heat flow across the EC) [156]

$$Q_{\text{ec}} = mc_p\Delta T_{\text{ad}} = k \cdot A\frac{dT}{dx} \qquad\qquad (4.2)$$

where *k*, *A* and *x* are substrate material thermal conductivity, cross-sectional surface area and thickness, respectively. The thermal time constant (τ_{th}) of the material is defined as the amount of time required to reach 63.2 % of the initial temperature difference between EC material and substrate and can be given as[157]

$$\tau_{\text{th}} = \frac{mc_p}{\frac{kA}{x}} \qquad\qquad (4.3)$$

The *m*, c_p and *A* are constant. Thus, τ_{th} can be written as $\tau_{th} \propto \frac{x}{k}$. Further, with the increase in the thickness of the substrate material (*x*), τ_{th} also increases. Hence, the time required by the substrate to attain the ΔT_{ad} also increases, and the same is observed in Figures 4.3 and 4.4, where the increasing thickness of the substrate has less ΔT_{ad} for a given period. To look in-depth, Al and PET having maximum and minimum *k* of 237 W/mK and 0.15 W/mK, respectively, are considered to analyze τ_{th}. The τ_{th} is found as 1.21×10^{-5} sec and 0.0192 sec for Al and PET under 10 μm substrate thickness, where τ_{th} increases to 6.07×10^{-4} sec and 0.96 sec, respectively, when thickness increases to 500 μm. Thus, the material with a higher *k* requires a lower time constant and heats up faster.

However, the effect of *k* is less pronounced at smaller thickness (10 μm) due to low thermal capacity and more at higher thickness (500 μm). The same is reflected in the comparison of ΔT_{ad} for various substrate materials along with thickness, as depicted in Figure 4.4. Moreover, a further in-depth study is needed to examine the effect of τ_{th} on the ECE, considering the fixed thickness and material conductivity, which is out of the scope of the present work. The EC materials and electrode (Au) thickness are kept fixed throughout the simulation at 100 μm and 0.1 μm. Hence, as the substrate layer thickness increases, the ECE decreases. However, PDMS and PET's shortcomings are their low thermal conductivity (~0.18 W/m.K), which results in inefficient heat transfer or reduced EC cyclic frequency [158]. Hence, aluminium is a better solution as a substrate material with higher thermal conductivity and low cost. Literature suggests that the substrate material thickness should be 100 μm; thus, Al substrate thickness is considered 100 μm for further analysis [8, 132].
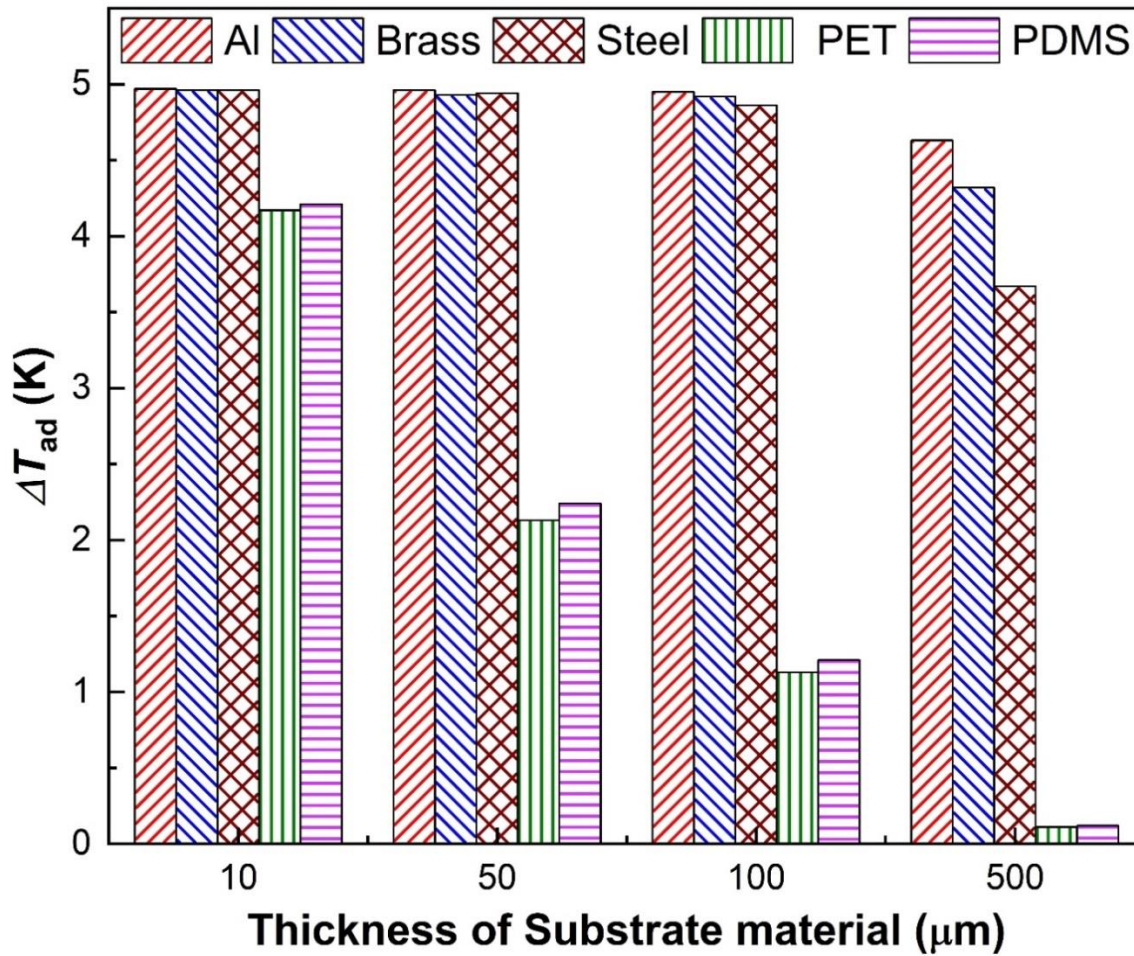
Figure 4.4. Comparison of ΔT_{ad} for various substrate materials along with thickness.

The simulation performed till now provides the necessary materials and operating parameters to use it for practical application. In the first step of the simulation study, the electric field (100 MV/m) and its cycle (slant rise, holding, and sudden drop) are obtained as discussed in Chapter 3, and later, the electrode materials (Au) and thickness (0.1 μm) are fixed. Finally, the substrate materials (Al) and thickness (100 μm) are determined. These parameters are used for further practical analysis of battery cooling. The cyclic cooling power density of the ECE device depends on the heat transfer during the heat absorption and dissipation to air/atmosphere. The heat transfer during the heat absorption can be given by [149]

$$Q_{ad} = cx\Delta T_{av}/\tau_c \qquad\qquad (4.4)$$

Where c, x, and τ_c are volumetric heat capacity, the thickness of the electrode assembly, and the cycle period. The ΔT_{av} is the average temperature change of the ECE device in the heat absorption process. In order to found effective heat transfer, two-time scales, (i) heat diffusion time and (ii) RC thermal time constant, need to be considered [149]. A detailed

discussion on both time scales has been done by Ju *et al.* [149] and predicted cooling power density versus τ_c variation for different thermal conductivity and electrode assembly. As to this point, the effect of the electrode and substrate material on ECE is discussed in detail in the form of adiabatic temperature change (ΔT_{ad}). Generally, the EC material is usually coated with electrode material on the top and bottom sides. These layers are connected, as shown in Figure 4.3 (a) inset (i). electrode, EC, and substrate material are connected, and there is interfacial thermal resistance, which directly affects the EC device performance. The same is discussed below in detail.

The interface thermal resistance plays a vital role, and a significant temperature drop occurs at the interface due to the difference in the conductivity. However, with the application of an electric field, the electrostatic attraction binds the interface more rigidly than mechanical forces [8]. Hence, to accurately predict the values of temperature loss, the temperature drops across the thermal contact, denoted as $\Delta T_{tc,}$ is expressed as the product of the heat flux (Q) and the thermal contact resistance (R_{th}), given by

$$\Delta T_{tc} = Q \times R_{th} \tag{4.5}$$

The thermal contact resistance (the inverse of thermal interface conductance) values for various materials are obtained from literature data and simulation is performed. The thermal contact resistance for P(VDF-TrFE-CFE) and Au is 1×10^{-4} m^{2}K/W[118] ($ec - electro$), Au and Al is 1.2×10^{-8} m^{2}K/W[119, 120] ($electro - sub$), and same for Al(substrate) and Al (heat source) is 4×10^{-5} m^{2}K/W[121, 122] ($sub - source/sink$). The experiment data for thermal contact resistance between P(VDF-TrFE-CFE) – Au and Au and Al are unavailable; hence, polymer-metal [118] and metal-metal [119, 120] values are considered. Here, it should be noted that the polymer-metal and metal-metal thicknesses are thin compared to the present work. The ΔT_{tc} is losses due to various thermal contact resistances that occur at interfaces (EC material-electrode ($\Delta T_{ec-electro}$), electrode-substrate ($\Delta T_{electro-sub}$), substrate-heat source/sink ($\Delta T_{sub-source}$) or electrode-source/sink ($\Delta T_{elec-sink}$)). The total ΔT_{tc} can be written as

$$\Delta T_{tc} = \Delta T_{ec-electro} + \Delta T_{electro-sub} + \Delta T_{sub-source/sink} \; or \; \Delta T_{electro-source/sink} \tag{4.6}$$

The temperature loss due to contact between different layers is given by equation 4.5, as shown in Figure 4.5. The graph in Figure 4.5 depicts the simulation result using the experimentally measured resistance value. The $\Delta T_{ec-electro}$, $\Delta T_{electro-sub}$, and $\Delta T_{sub-source}$ were found as 0.51 K, 1.66 $\times10^{-5}$ K, and 0.05 K, respectively.

Figure 4.5. The temperature loss (ΔT_{tc}) due to thermal contact resistance (experimental values taken for simulation) between (a) EC material and electrode, (b) electrode and substrate, and (c) substrate and source.

The total ΔT_{tc} is 0.56 K (11.4%) of ΔT_{ad} = 4.91 K. Further, theoretical calculations are conducted on the thermal contact resistance obtained from experimental results. The theoretical calculation done by Mikic *et al.*[159] was also used to calculate the thermal contact resistance. The thermal conductance (h_c) can be given by [159]

$$h_c = 1.13 \frac{m_s k_s}{\sigma} \left(\frac{p}{H_c}\right)^{0.94} \tag{4.7}$$

where m_s is the effective mean asperity slope, k_s is the effective thermal conductivity, p is the contact pressure, σ is the Stefan Boltzmann constant, H_C is the microhardness-taking the material property shown in Table 4.2. Thus, the calculated thermal contact resistance for P(VDF-TrFE-CFE) and Au is 3.95×10^{-4} m²K/W ($ec - electro$), Au and Al is 2.73×10^{-6} m²K/W ($electro - sub$), and the same for Al(substrate) and Al (heat source) is 1.4×10^{-4} m²K/W ($sub - source/sink$).

Table 4.2. Properties used to calculate material thermal conductance[13, 17-19, 112].

Material	Thermal conductivity (W/mK)	RMS Surface Roughness (μm)	Asperity slope	Micro-Hardness (MPa)
P(VDF-TrFE-CFE)	0.2	1.23	0.20	40
Au	430	0.12	0.03	700
Al	210.07	0.12	0.03	1400

The loss in temperature due to contact between different layers can be given by equation 4.5, which is simulated, as shown in Figure 4.6.
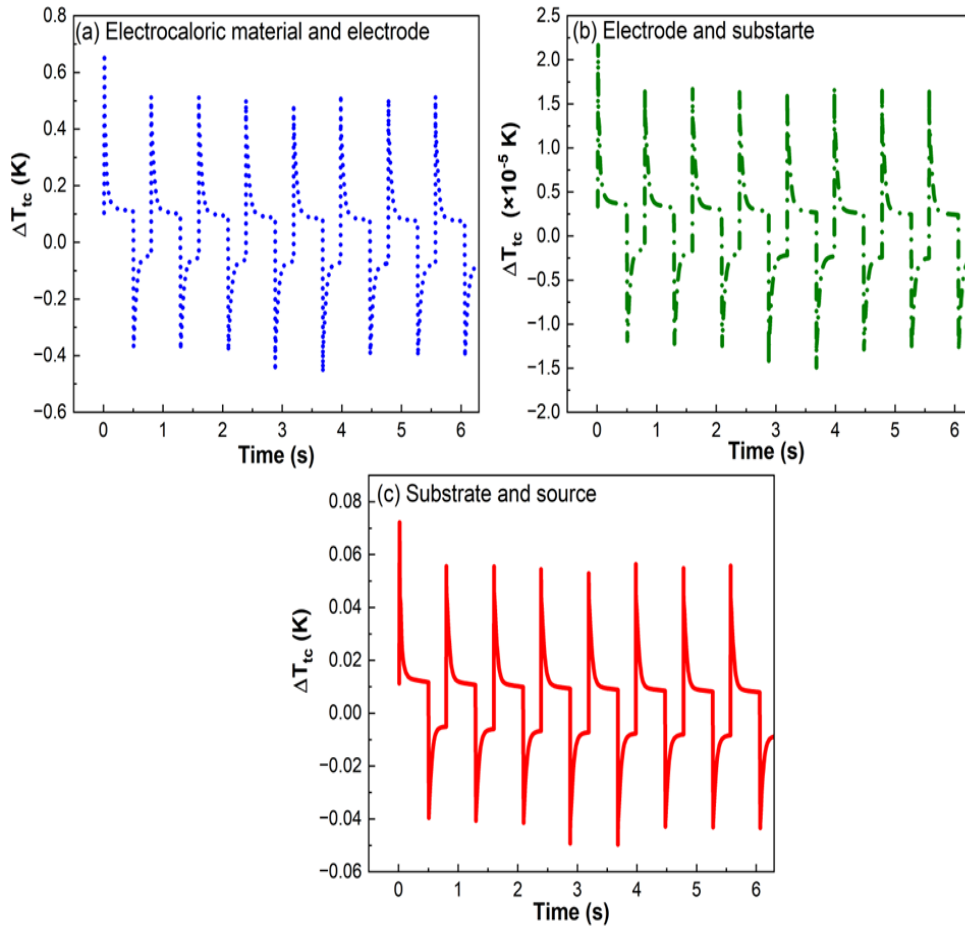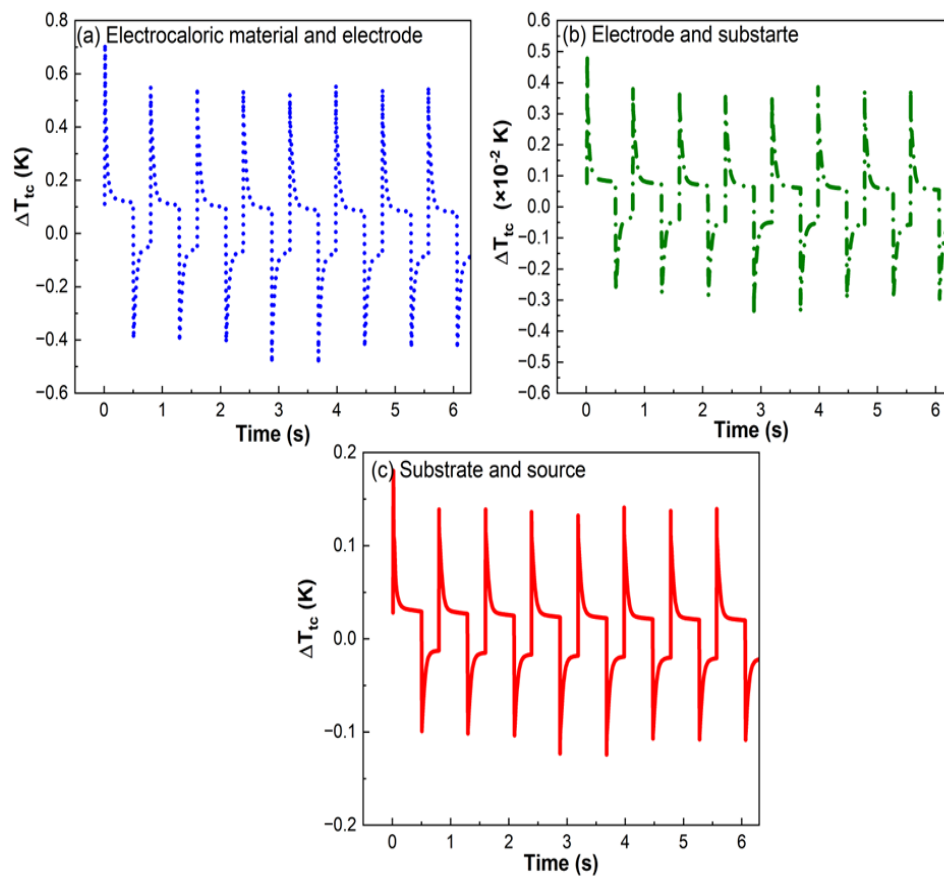

Figure 4.6. The temperature loss (ΔT_{tc}) due to thermal contact resistance (theoretical values taken for simulation) between (a) EC material and electrode, (b) Electrode and substrate, and (c) substrate and source.

The graph in Figure 4.6 shows the simulation result using the theoretical measured resistance value. The motive of Figure 4.5 and 4.6 is to justify that the modeling that is being used in the present analysis is correct because the values of ΔT_{tc} is nearly comparable for both experimental and theoretical study. The $\Delta T_{ec-electro}$, $\Delta T_{electro-sub}$,

and $\Delta T_{sub-source}$ were calculated as 0.53 K, 0.37×10^{-2} K, and 0.13 K. The total ΔT_{tc} is 0.66 K (~13.5% of ΔT_{ad} = 4.91 K), equivalent to experimentally estimated ΔT_{tc} (0.56 K=11.4%). In summary, the working temperature, electrode (Au)/substrate (Al) materials, and thickness effect are evaluated and used for further analysis. The battery cooling and performance of the EC device are further examined in Chapter 5.

4.4 Conclusions

The study varied operating temperatures from 293.15 K to 373.15 K for ECE estimation. For ECE analysis, the electrode material thickness ranges from 0.01 to 10 µm for various materials (Au, Ag, Al, Cu, Ti, Ni, Pd, CNT). Similarly, the substrate material Al, Brass, Steel, PET, and PDMS thickness varied from 10 to 500 µm for ECE analysis. The optimal working temperature, electrode, and substrate materials are 293.15 K, Au (0.1 µm), and Al (100 µm), respectively, and the same is used for further investigation (chapter 5). The thermal contact (ΔT_{tc}) loss between layers is 0.66 K, or approximately 13.5% of the total ΔT_{ad} = 4.91 K, equivalent to the ΔT_{tc} obtained experimentally.

<div align="right">**Chapter 5**</div>

Battery Cooling by Electrocaloric Effect

A smartphone battery's surface (7 cm × 3 cm) is considered for cooling by the proposed electrocaloric (EC) device design. The same battery is also used to provide the necessary input voltage. The performance of an EC device is assessed by comparing the battery cooled by air, the battery and the EC device in contact (E=0, without ECE), and the battery and the EC device in contact cooling (E=100 MV/m, with ECE). The simulation study shows that the battery's surface/source temperature dropped from 313.15 K to ~298 K, ~297.5 K, and ~293.5 K when air cooling, the EC device in contact with the battery (no ECE, E=0) and EC device in contact with battery (with ECE, E =100 MV/m), respectively in ~6.5 seconds. The impact of the operating temperature source on the cooling process is also explored. The high-voltage application setup using the mobile battery is described thoroughly. The study shows that the battery cools quicker than air when using the ECE device. The proposed EC device design can provide new insight for mobile or other electronic cooling applications.

5.1 Introduction

The increasing prevalence of portable devices and electronic gadgets poses a significant cooling challenge[160]. Traditional compression refrigeration technology is inadequate for meeting current demands, leading to a growing interest in EC cooling technology as the most promising solution[160]. The motivation to tackle smartphone battery cooling with the ECE lies in its promise of energy-efficient cooling, enabling longer battery life and reduced energy consumption[161]. This approach also supports miniaturization efforts, which are crucial for compact devices[161]. Additionally, it offers environmentally friendly cooling solutions, mitigating the environmental impact of traditional methods while fostering innovation in the electronics industry[162]. In this direction, P(VDF-TrFE-CFE) polymer stack on both sides and electrostatically actuated in an "s" shape between the heat source and heat sink is used as the active EC device[8]. The battery was cooled by air and an EC device (66.7 MV/m at 0.8 Hz), and the battery's temperature decreased by 3 K and 8 K in 50 s, respectively[8]. The temperature ranges from 1.7 K to 5 K when the electric field increases from 50 MV/m to 100 MV/m[96]. Under an electric field of 40 MV/m at 1 Hz, the nanocomposite's average cooling heat flux can reach 293.14 W/m^2 at 298 K. The EC cooling device has a specific cooling

power of 0.96 W/g and a coefficient of performance (COP) of 3.6[160]. According to numerical models, when COP > 10, cooling power densities larger than 10 W/cm^2 may be achieved across ΔT_{ad} of 10 K [149]. When exposed to an electric field of 100 MV/m, EC fibers' maximum cooling temperature (ΔT) is approximately 0.7 K. The peak heat flow recorded for a 0.8 cm long fiber is 4 mW[163]. At 1.0 Hz and 60 MV/m, A four-layer cascade device may reach a maximum temperature lift of 8.7 K under no-load conditions when operating in an EC electric field with a ΔT_{ad} of 3.0 K[42]. A simulation suggests an 8-layer device can reach 20 K at a higher frequency[42]. This cascade device has a tiny volume and minimum driving apparatus, making it suitable for managing heat in compact electronics[42]. No tests were undertaken at 100 MV/m to study the EC module's dielectric breakdown[96].

Ma *et al.*[8] did considerable work to address the issue of smartphone batteries. In an experiment, they demonstrated how the ECE cools batteries by showing a rapid 8 K (325.5 to 317.5 K) drop in temperature in the first 10 seconds, followed by a drop in temperature to 4 K (317.5 to 313.5 K) in the final 40 seconds[8]. The reasons for the initial 10 seconds substantial drop in temperature are not explained[8]. Moreover, they used a single electric waveform, two layers of EC material and fixed battery thickness. Many applications, including microelectronics and medical technology devices, need high cooling power, a large temperature span, and high efficiency[96]. The literature did not focus on how they would apply such a high electric field. The simulation methodology or the software's detail, geometry specification, and material parameters are not provided.

The present study describes the step-by-step modeling procedure. It includes all geometrical dimensions and material properties. In contrast, optimized waveform, one layer of EC material, and variation in battery thicknesses are studied in this work. An EC device cools a smartphone battery made up of an electrode, an EC, and a substrate material. The performance of the EC device with air cooling, EC device without ECE, and EC device with ECE is then compared. Finally, an experimental setup consisting of a 5 V battery has been used to generate an output voltage of 10 kV (100 MV/m) for practical EC device operation, which is lacking in the previous literature. Thus, the proposed experimental setup can be used for the real-time application of EC devices and pave the way for its commercial application.

5.2 Battery cooling

The operating temperature of batteries significantly influences their performance, safety, and lifespan. Maintaining batteries within the recommended temperature range ensures optimal efficiency and longevity. A simple battery can generate the required voltage using the booster circuit, as discussed in section 5.3. As a result, the same battery used to cool can also provide the necessary voltage. The present analysis considers the heat source of a mobile phone battery with a 7 cm × 3 cm surface area. The EC device is made up of an electrode (Au, 0.1 μm thick), EC (P(VDF-TrFE-CFE), 100 μm thick), and a substrate (Al, 100 μm thick) material. Further, when the electric field is applied to the P(VDF-TrFE-CFE), it undergoes deformation or changes in shape due to the electrostriction effect. The electrostriction can be utilized to deflect a cantilever beam between the heat source and the sink. An extensive analysis was conducted to finalize the EC device design based on stress and deflection. The EC device design is also crucial because it will transfer heat from the source to the sink by effectively contacting them. Thus, a cantilever beam made of electrostrictive–/EC material is considered, as shown in Figure 5.1. When an electric field is applied to a cantilever beam, the material experiences strain (electrostriction). This means that the material changes shape or dimensions due to the reorientation of electric dipoles within the material. Thus, the beam deflects or bends.

The direction and magnitude of the deflection depend on applied electric field strength and direction, electrostrictive properties, and geometry. The deflection of the beam can be precisely manipulated by controlling the applied electric field and direction, as shown in Figure 5.1. The cantilever EC material coated with electrode deflects in up and downward directions as the electric field changes; see Figure 5.1 inset (I) and inset (II). The maximum deflection is ~881 μm under 100 MV/m electric pulse. The displacement diagram is also in pulse shape, as depicted by the green-colored line in Figure 5.1. As the electric field increases, the EC material deflects upwards; after that, the electric field is held in place for some time, at which the position of the EC material is displayed in the inset (I). The EC material comes into contact with the heat sink; the applied electric field reaches its maximum. The electric field decreases from $E = E_{max}$ to $E = 0$. The EC material also deflects downward; the position of an EC device is illustrated in the inset (II). Currently, the EC material is in contact with the heat source, which is held in place for a while. This single cycle lasted from time $t = 0$ to 1.2 seconds. The cycle repeats

itself, and deflection can be investigated experimentally. However, in the current study, simulation modeling was performed using the COMSOL Multiphysics software, which makes it extremely difficult to build such a deflecting EC material system for transferring heat from the heat source to the heat sink.
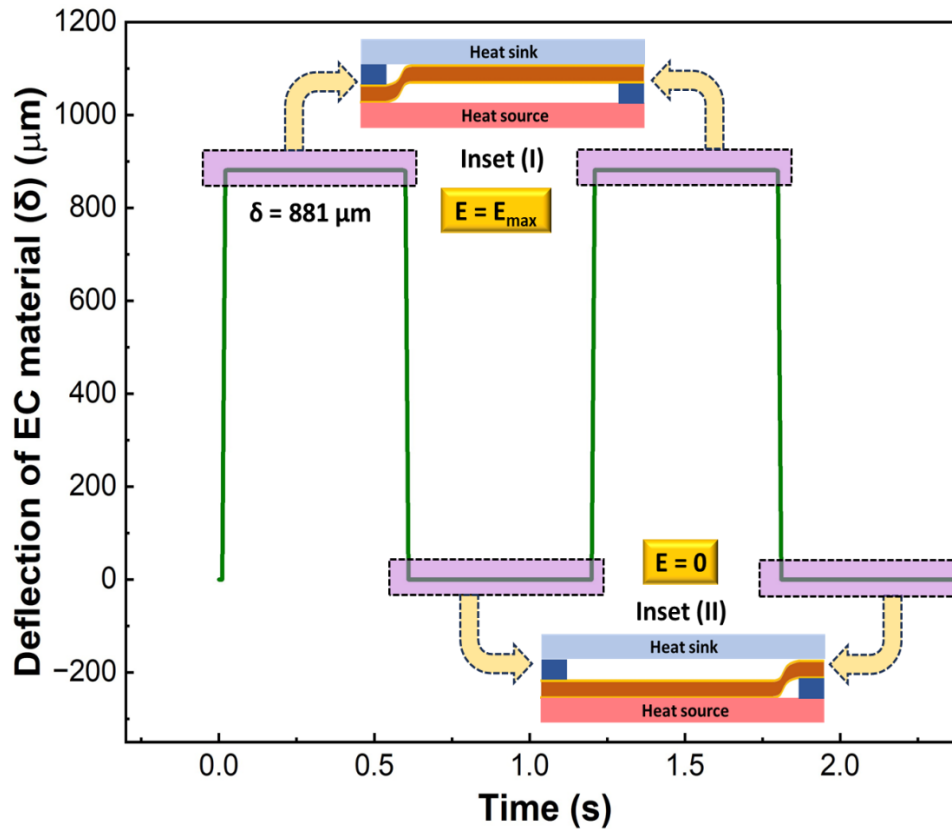

Figure 5.1. Deflection of EC material with positioned schematic diagram of EC device.

As a result, the assumption is made that the EC device only comes into contact with the battery source when it is overheated, and the EC device is withdrawn when it reaches room temperature. Whenever the battery overheats, the EC device comes into contact with it. So, taking these factors into account, the current study was conducted.

A comparison has been made between battery cooling in (i) air (top surface of source/ battery is exposed to air), (ii) source/battery and EC device are in contact, but ECE is not used ($E = 0$) ($E = 0$, the top surface of EC device is exposed to air and cooling is done), and (iii) source/battery and EC device are in contact where ECE is used ($E = 100$ MV/m), the top surface of EC device is exposed to air), see Figure 5.2(a) inset. The source/battery in air cooling, in contact without ECE and with ECE are depicted in Figure 5.2 (a) as inset (i), inset (ii) (without ECE, E=0) and inset (ii) (with ECE, $E = 100$ MV/m), respectively.
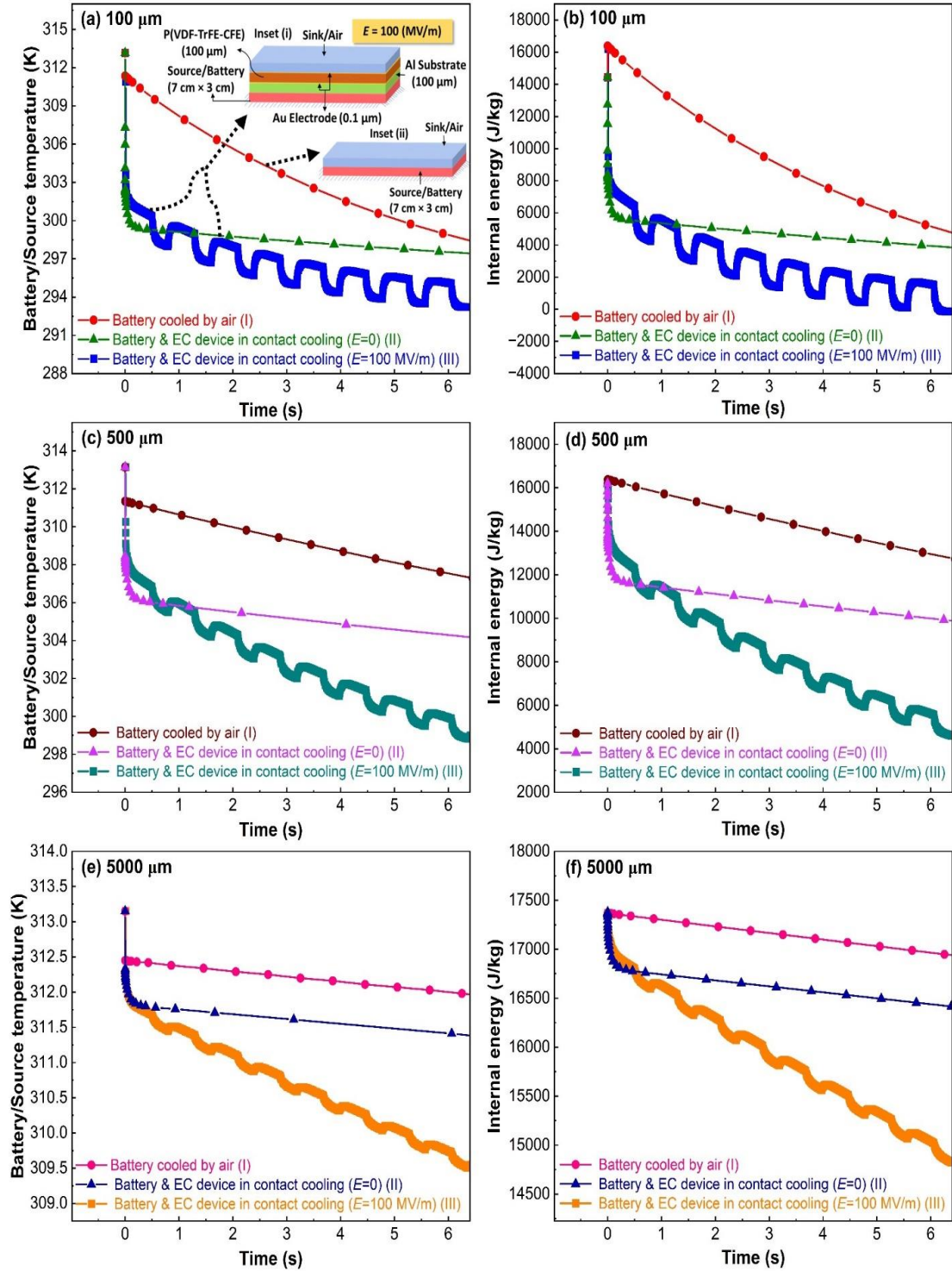
Figure 5.2. Performance of EC device: comparison between battery/source temperature when air cooling, battery/source and EC device are in contact (with $E = 0$) and battery/source and EC device is in contact with ($E = 100$ MV/m) when battery/source thickness is (a) 100 μm, (c) 500 μm, and (e) 5000 μm, respectively. The corresponding internal energy variation when battery/source thickness (b) 100 μm, (d) 500 μm, and (f) 5000 μm, respectively.

The battery/source and air temperature are kept at 313.15 K and 293.15 K, as shown in Figure 5.2 (a) and exposed to the environment for air-based cooling. The EC device surface area is considered the same as the source and the thickness of P(VDF-TrFE-CFE) used is 100 μm. Figure 5.2(a) presents the decrease in temperature versus the time required to cool down the battery/source surface naturally. It is found that source temperature decreases from 313.15 K to approximately 298 K (air cooling), 297.6 K (with contact, $E = 0$) and 293 K (with ECE, E=100 MV/m) in 6.5 seconds. The corresponding change in internal energy of the source with air cooling, with ECE device in contact ($E = 0$), and with ECE device in contact (E = 100 MV/m) is shown in Figure 5.2(b), considering source thickness of 100 μm. Internal energy is proportional to temperature, decreasing due to the cooling process.

The internal energy was calculated per unit weight to compare the results of different source thicknesses. Air-based battery cooling takes more time than cooling a battery by an ECE device. A sharp decrease in battery temperature is observed in the initial few seconds due to the contact of the ECE device with the battery. Hence, this effect is obtained when the ECE device and source are in contact without ECE and with ECE. However, it is essential to note that this sharp decrement results from the conduction heat transfer by the device. This sharp decrease in temperature is beneficial in the case of overheating of the battery, as the source must dissipate a large amount of heat quickly. It is assumed that the EC device only comes in contact with the battery during overheating. When the temperature decreases, the EC device will not be in contact with the battery. Further, the thickness of the source increases to 500 μm which the battery/source temperature drops down to 307.3 K (air cooling), 304.2 K (EC device in contact without ECE, $E = 0$), and 299 K (EC device in contact with ECE, $E = 100$ MV/m) as shown in Figure 5.2(c). Moreover, if the thickness of the source increased to 5000 μm, then the battery/source temperature falls to 311.9 K (air cooling), 311.3 K (EC device in contact without ECE, $E = 0$ and 309.5 K (EC device in contact with ECE, $E = 100$ MV/m). Figures 5.2(d) and (f) show the corresponding change in internal energy for source thickness of 500 and 5000 μm, respectively. The temperature drops slowly as the source thickness increases because more internal heat is available in a thicker battery/source. If the thickness increases, it will give less ΔT_{ad}, which can be observed from the source's internal energy (see Figure 5.2 (e). The simulation study shows that in 6.5 seconds, the battery can cool 20 K (100 μm thick source), 14 K (500 μm thick source), and 3.6 K

(5000 μm thick source), whereas Ma *et al*. [8] experimental work, it takes 50 s to cool 11.8 K (325.5 K to 313.5 K) for 5000 μm thick source. Here, it should be noted that the cooling time depends on the contact area, electrode and substrate materials, the thickness of EC material and the heat source. Apart from the surface area, only conduction heat transfer will be observed in a shorter time scale (0-1 sec), as shown in Figure 5.2(a). Thus, the present work uses a larger time scale of 6.5 sec to analyze the conduction heat transfer and EC effect. To understand the heat transfer process in the ECE cycle, pictorial representation has been done in Figure 5.3. In contrast, the middle layers are P(VDF-TrFE-CFE) (in contact with air and substrate) and substrate (in contact with the source and P(VDF-TrFE-CFE)).

In the same way, at the initial state $t = 0$ sec, the source, ECE device and air are kept as ~313.15 K, 293.15 K and 293.15 K, respectively. Now, at $t = 0.01$ sec, air and the EC device are in contact with the source, and heat is transferred, as shown in Figures 5.3(a) and (e). Figure 5.3(a-d) shows the heat transfer between the battery and air layer, which consists of the continuous decreasing behavior of source temperature as observed in Figure 5.2(a). Figures 5.3(e-l) show contour plots of the EC cycle utilized for cooling for the first three cycles ranging from 0 to 2.3 sec, the same electric cycle used in the analysis depicted in Figure 5.2(a). Figures 5.3(f) and (g) show a plot when holding time at $E = E_{max}$ and holding time at $E = 0$, respectively. Figures 5.3(h) and (i) show the contour plots when the electric field is applied and an electric field is removed, respectively. Figures 5.3(j) and (l) show the contour plots when holding time at $E = E_{max}$ and holding time at $E = 0$, respectively.

The temperature with time of the device can also be seen in Figure 5.2(a); the contour plots (e-l) show the corresponding temperature profile in the different layers. Further, at $t = 2.3$ sec, Figures 5.3(b) and (l) show that the source temperature decreased to 304 K and 295 K, respectively. It suggests that within 2.3 sec, the ECE device can cool the battery sources to 295 K, whereas the air can cool it to 304 K, as seen in Figure 5.3. Hence, it is concluded that the source cooled in the air takes longer than the source cooled with an EC device. Thus, ECE can be an efficient alternative to battery cooling techniques. The analysis considers the battery/source temperature to be 313.15 K, whereas the source temperature can vary in practical applications. The operating temperature of the source is not fixed because it depends on the heat dissipation capacity of different devices.

Therefore, the time required for cooling to reach a specific temperature while the battery (source) has other operating temperature conditions is further analyzed.
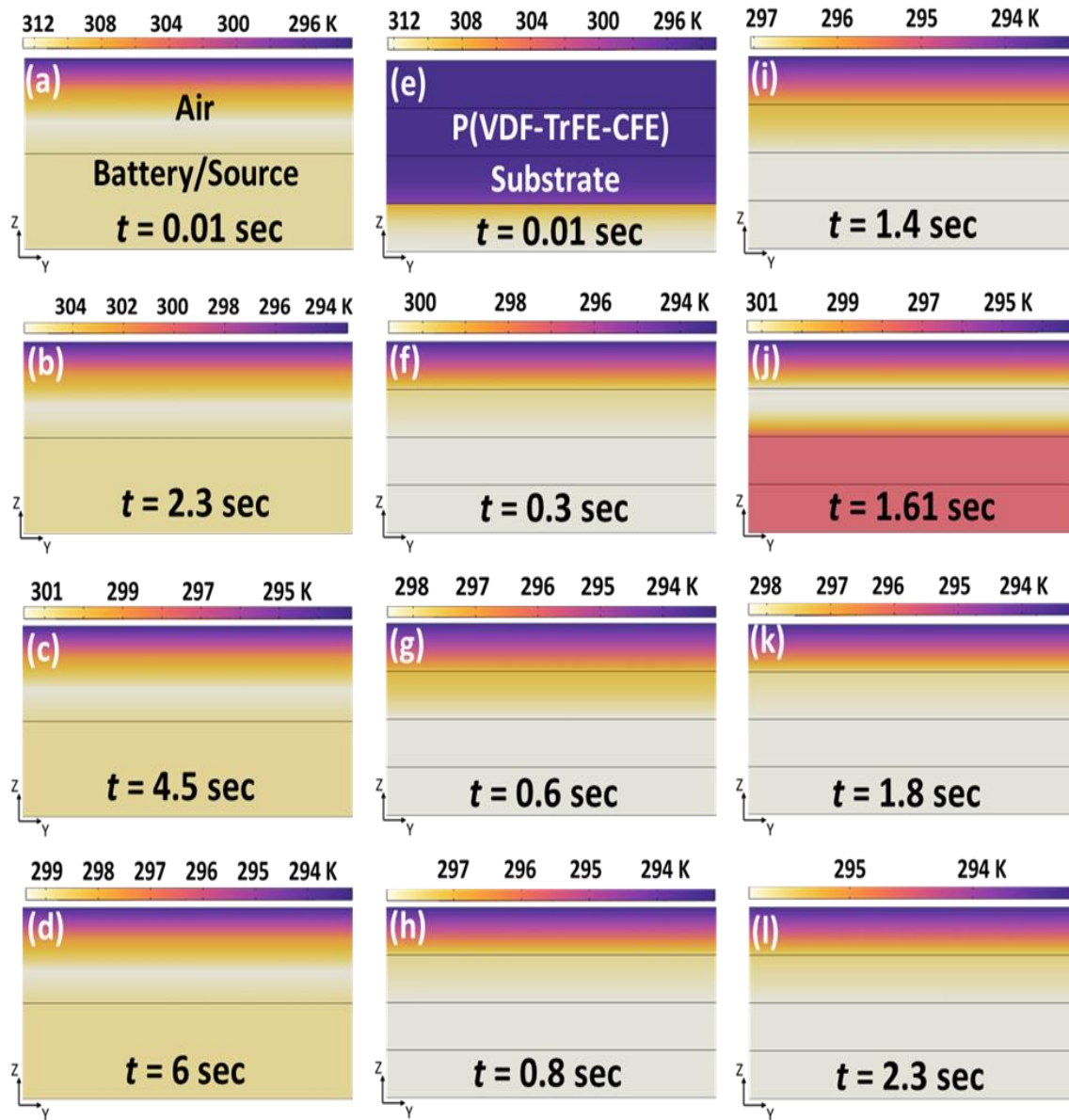
Figure 5.3. Temperature contour plots at various times with (a-d) battery cooling by air and (e-l) battery cooling by EC device (E =100 MV/m) correspond to Figure 5.2(a).

Figure 5.3 depicts the heat transfer inside the material as a function of time. Figures 5.3 (a), (b), (c) and (d) illustrate the battery surface/source with air cooling. Figures 5.3 (e), (f), (g), (h), (i), (j), (k) and (l) depicted the source with ECE device in contact (with ECE). Figure 5.3 (a), (b), (c) and (d) shows two layers (the bottom sources and the top layer is air); at the initial state $t = 0$ sec, the source and air temperature is as ~313.15 K and 293.15 K. Similarly, Figures 5.3 (e), (f), (g), (h), (i), (j), (k) and (l) shows that source is in

contact with ECE device, where bottom and top layer are source and air. As no direct method is available in COMSOL Multiphysics to incorporate ΔT_{tc}, the effective EC temperature change $(\Delta T_{ad})_{effective}$ is obtained using equation 2.31 in section 2.2 of chapter 2. Here, it should be noted that the ΔT_{hys} and ΔT_{tc} losses are not accounted for in the reported temperature change in Figures 5.2 and 5.3. Further, in Figures 5.4 and 5.5, the ΔT_{hys} and ΔT_{tc} losses have been incorporated.
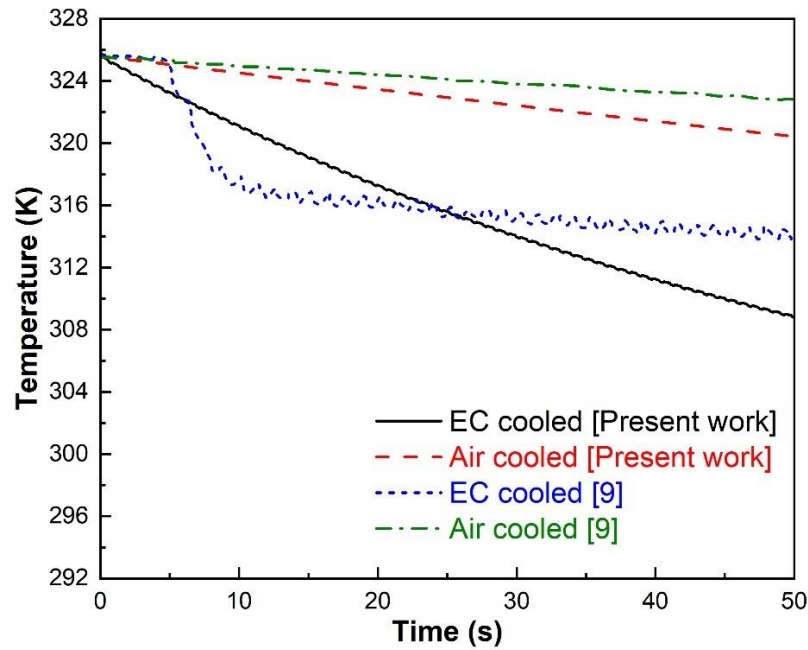

Figure 5.4. Comparison of air and EC cooling of source by Ma *et al.* [8] and present work. From [Ma R, Zhang Z, Tong K, Huber D, Kornbluh R, Ju Y S, and Pei Q 2017 Highly efficient EC cooling with electrostatic actuation *Science* 357(6356) p. 1130-1134.] Reprinted with permission from AAAS.

Therefore, Figure 5.4 compares battery cooling by Ma *et al.* [8] experimental work and present simulation taking the $(\Delta T_{ad})_{effective}$ as 4.01 K (considering 5% and 13.5 % losses due to ΔT_{hys} and ΔT_{tc}). Figure 5.4 displays the battery cooling in the air by current work, and Ma *et al.*'s [8] experiments consisted of an almost similar temperature decrease in 50 seconds. The slight variation in battery cooling in the air by Ma *et al.*'s [8] and present work occurs due to insufficient data, such as air velocity, electric waveform, environment temperature, etc. The present work shows that the EC device performed better cooling than the work of Ma *et al.* [8]. They experimentally showed the EC effect for battery cooling, a sharp decrease in temperature of 9 K (325.5 to 317.5 K) in the initial 10 sec and the remaining 40 sec temperature decreases to 4 K (317.5 to 313.5 K) only. The reasons behind the initial 10 sec sharp decrease in the temperature are not mentioned.

However, in the present work, a similar trend is observed and explained as an effect of conduction (contact between the battery and the EC device). Thus, Ma *et al*. [8] have EC cooling of 4 K in 40 s, whereas the present work shows 12 K cooling in 40 sec, see Figure 5.4. It should be noted that in the current work, the EC element is modeled without considering thermal switches at the interfaces.
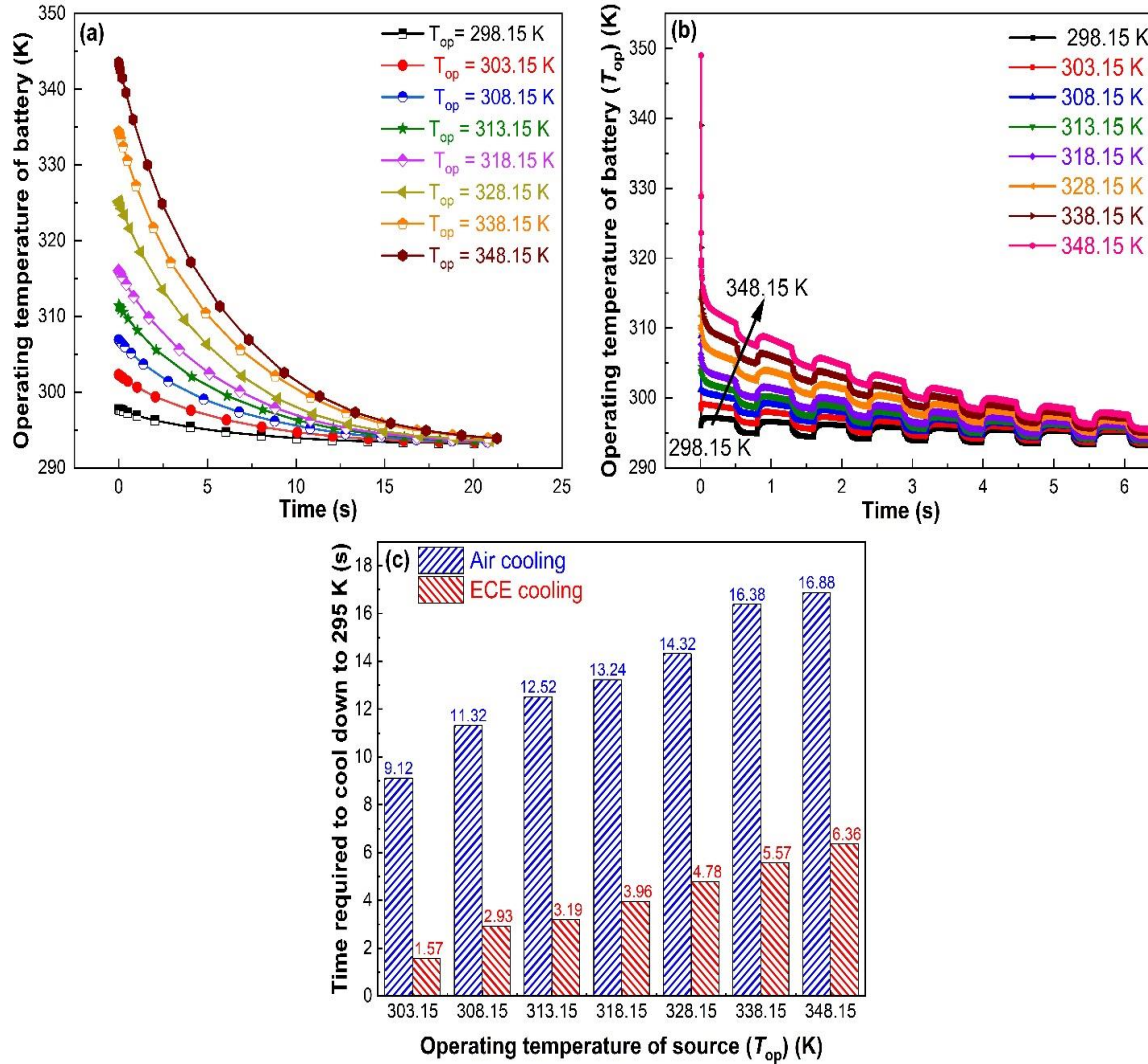
Figure 5.5. The effect of the operating temperature of the source. (a) air cooling, (b) EC device cooling, and (c) a comparison between air and EC device cooling in the context of cooling time.

Nevertheless, Ma *et al*. [8] considered thermal switches, which electrostatically actuate the EC element between the heat source and heat sink. The present simulation performed better EC cooling than Ma *et al*. [8]. The impact of battery operating temperature (source) on the amount of time needed to cool down is shown in Figure 5.5. The cool-down temperature is set as 295 K to observe the effect only.

The battery's operating temperature ranges from 298.15 K to 348.15 K, and the battery is exposed to environmental conditions and air-cooled to 295 K, as represented in Figure 5.5(a). Figure 5.5(b) depicts source cooling with an EC device (E =100 MV/m) while considering the same operational temperature range. Additionally, the outcome of Figures 5.5(a) and (b) are depicted in Figure 5.5(c), as the source has a higher operating temperature, and it takes more time to cool down. As a battery's operating temperature rises, it takes longer to drop to 295 K. The direct comparison between the source cooled by air and the EC device concerning cooling time is described in Figure 5.5(c). It shows that EC device-based battery cooling is an effective technique for portable devices. The simulation results suggest that it can be easily integrated into the mobile or portable electronic device as the thickness of the proposed device is 200.2 μm. However, further research is needed to see the effect of cycle contact on sources and EC devices.

5.3 Battery as electric field source for ECE

The EC device needed an electric field of 100 MV/m; thus, one must explore the option of applying high electric fields. The electric field source plays a vital role in maintaining the battery temperature in the EC device. It is typically provided by an external power supply or generator capable of generating the required electric field strength. The source must deliver a stable, controllable, directional electric field with a higher magnitude. Additionally, the electric field source must be compatible with the experimental setup or device in which the ECE is being utilized. Various types of electric field sources, such as DC power supplies or function generators, may be employed depending on the application's specific requirements. Overall, the electric field source is the driving force behind the ECE, enabling precise control and manipulation of temperature within the material for diverse applications. The need for a high electric field in EC devices has constrained their practical application. However, it can be achieved by reducing the thickness of EC materials up to a few micrometers or using a device that can produce a high electric field (such as a booster circuit). The first method is more reliable and practical compared to the second method. Nevertheless, the thin film heat carrying capacity ($Q = mc_p\Delta T_{\text{ad}}$) is small; therefore, to overcome this issue, a thin multilayer is needed[156, 164]. Using a thin multilayered EC material stack reduces the need for a high electric field and increases thermal mass due to the packing of several layers[143]. The multilayer also provides high electrical breakdown fields due to their reduced single-layer

thickness and effective heat transfer [150]. A detailed discussion on multilayer capacitors based on PVDF-TrFE cooling power is discussed by Kar-Narayan *et al*. [150].

The second method (booster circuit to obtain a high voltage) is used in the current study with an input electric source of 5 V. In this direction, Bauer *et al*.[10] also used an amplifier circuit to amplify the voltage up to 2.3 kV, which dropped to zero in 3 seconds. Hence, the proposed booster circuit can enhance the voltage up to 10 kV using a 3 V and 1.5 A power source. The following method can be used for real-time applications of high electric field miniaturized electronic systems and limited space constraints (see Figure 5.6). The applied electric field is 100 MV/m, corresponding to 10 kV for an EC material thickness of 100 µm. Several techniques are available for high-voltage applications, including a DC poling unit, a DC power supply, and a booster circuit. The poling unit can supply a voltage of up to 15 kV, but it is bulky and costly, so it cannot be employed for EC device-based thermal management of electronic devices. Using a DC power source is an additional, less bulky option, but there is still a cost concern. A booster circuit readily available in the market is an even more compact and reasonably priced option. Thus, a setup comprising a DC power source or mobile battery, a high-voltage booster, and a custom-built program has been used to obtain such a high voltage, as shown in the schematic diagram in Figure 5.6.
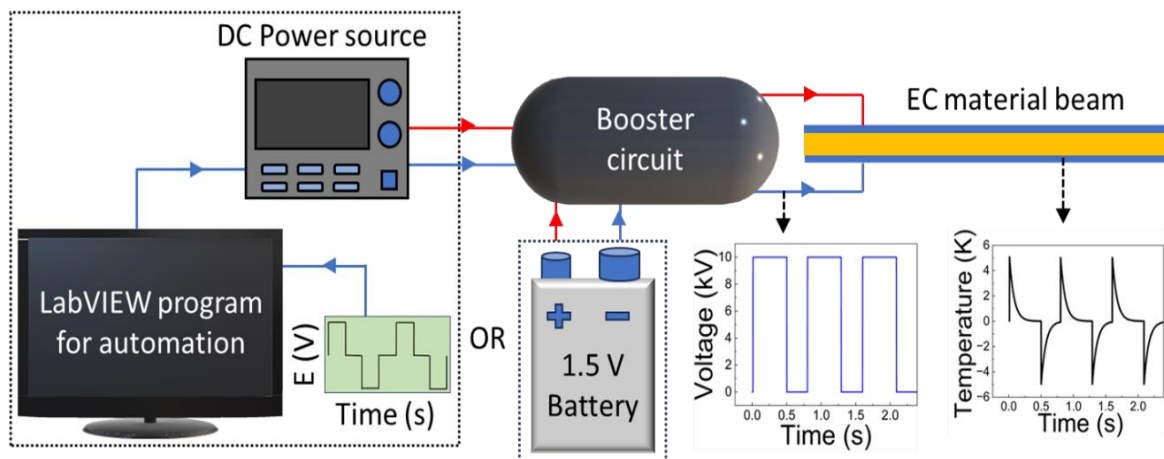
Figure 5.6. Schematic diagram of high voltage application setup

The booster circuit first boosts the low voltage supplied by batteries to a much higher voltage using a boosting stage. This increased voltage is then fed into an oscillator circuit, which generates high-frequency alternating current (AC) pulses typically ranging from tens of kilohertz to a few megahertz. These AC pulses are further amplified using a voltage multiplier circuit, such as a Cockcroft-Walton multiplier, consisting of diodes and

capacitors arranged in a ladder-like configuration. The amplified high-voltage pulses are then applied at the required place. When an electric potential is used, it completes the circuit, allowing the high-voltage pulses to pass through the material. This design efficiently converts low battery voltage into high-voltage pulses. The DC power source or battery provides an output voltage of 3 V power and 0.8 A current to the booster circuit, which boosts the voltage around 300 to 400 kV. This is a similar kind of high-voltage booster circuit used in teaser circuits. Figure 5.7(a) shows the experimental setup where a DC power source of 3 V and 1.2 A is passed to the booster circuit. The same outcome can be attained using a battery supply rather than a DC power source.

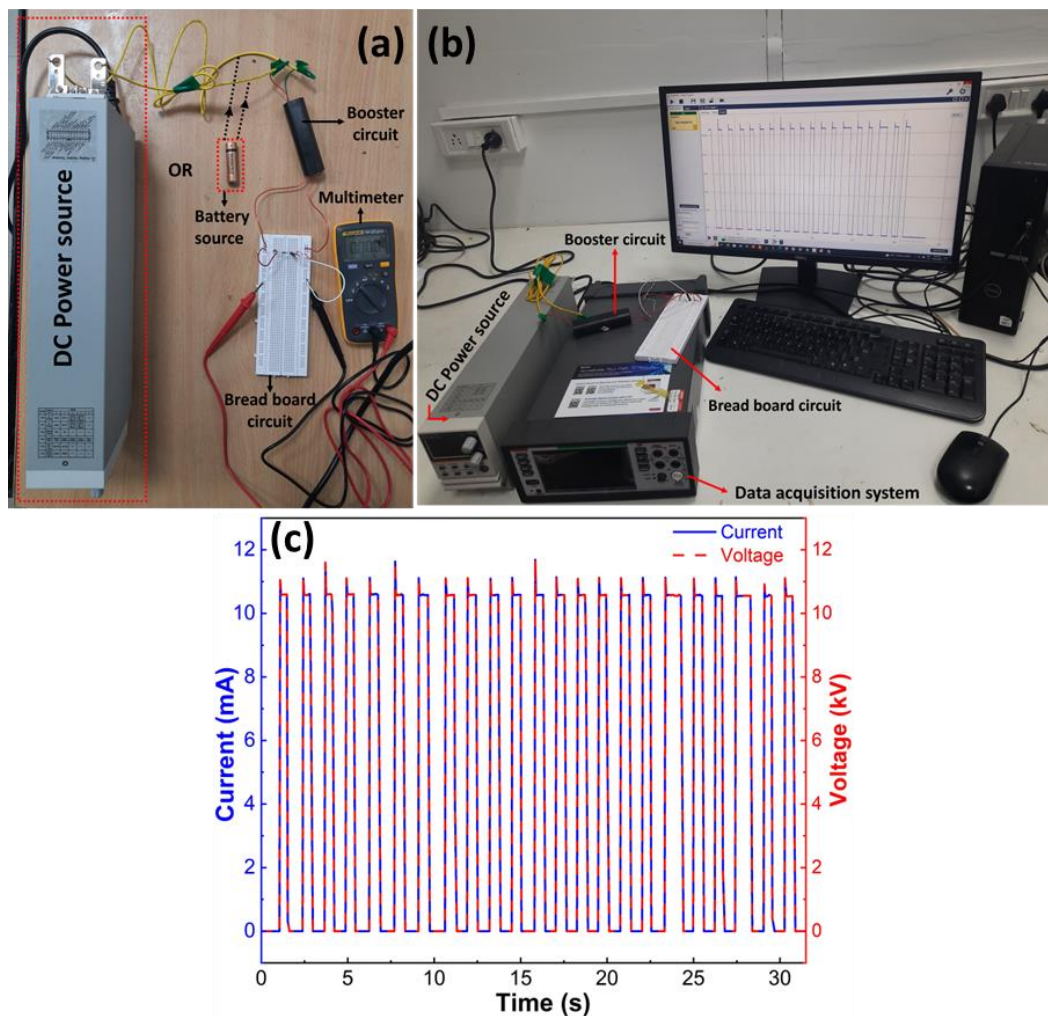
Figure 5.7. High voltage application setup (a) Experimental setup to measure current via multimeter, (b) Experimental setup to measure current via data acquisition system and (c) The corresponding value of current and voltage

The voltage is on and off in equal intervals of time or to give electric pulses (E(V) vs Time (s)), a LabVIEW program is used. This LabVIEW program communicates with the

DC power source and gives up the voltage as a square pulse. A similar result can be obtained using a pencil battery of 1.5 V (instead of a DC power source) to generate square pulses of electric field and voltage when passed via the booster circuit. The output current of 10 mA is measured across a 1 MΩ resistance using Keithley DAQ6510 and Kickstart software (Figure 5.7(b)). The corresponding current and voltage are shown in Figure 5.7(c). The voltage and current readings are roughly 10 kV and 10 mA, respectively. Therefore, applying such a high voltage in real life is possible. As indicated in the schematic Figure 5.6, this booster circuit is directly connected to the electrodes of an EC material, which causes temperature change over time. In the practical application, the input voltage (3 V) and current (1.2 A) can be easily provided by the mobile battery, and the EC device can be operated using the booster circuit. The simulation results presented can be easily implemented for mobile or electronic cooling. However, the use of booster circuits may be associated with less reliability and repeatability problems for practical application. Hence, an experimental analysis is required before considering booster circuits for practical applications.

5.4 Conclusion

The smartphone battery's surface area of 7 cm × 3 cm is considered for cooling to see the effectiveness of the EC device. The same smartphone battery is regarded as a power source for applying electric potential to the electrode. The battery/source surface was cooled by air, with contact of EC device $E = 0$ and with contact of EC device $E = 100$ MV/m from 313.15 K to ~298 K, 297.5 K, and 298.5 K, respectively, within 6.5 seconds. The time required to cool the battery to room temperature increases as the battery/source thickness increases. A booster circuit provides a compact, cost-effective, and practical solution that is readily available in the market as an electric field source for EC devices. The proposed booster circuit can be used to obtain a high electric field of 10 kV, which can enhance the practical applicability of the EC device. The proposed simulation study of an EC device can overcome issues of battery overheating and increased life, and it can also be used for wearable gadgets, microelectronics circuits, and other appliances.

<div align="right">

Chapter 6

</div>

<div align="center">

Conclusions and Future Outlook

</div>

6.1 Conclusions

Electrocaloric (EC) cooling emerges as a promising alternative to traditional cooling methods, offering significant advantages in terms of energy efficiency, environmental friendliness, and cost-effectiveness. The P(VDF-TrFE-CFE) terpolymer has higher EC temperature change, flexibility, scalability, and environmental friendliness, enhancing its suitability for EC applications. The COMSOL Multiphysics simulation is used for the EC analysis, considering P(VDF-TrFE-CFE) as an EC material. Equation-based modeling and the in-built module in COMSOL are compared for EC estimation, and the in-built pyroelectricity module is recommended for more accurate analysis. The electric field pulse (sinusoidal, waveform triangle, sawtooth, triangle withholding time, rectangular, slant-edge and slant-edge & sudden drop) and holding time have been used to get the maximum electrocaloric effect (ECE). A holding time of 0.3 seconds in square waveform provides the maximum EC temperature change. The optimized electric pulse and holding time are kept constant, and the electric field varies from 10 to 100 MV/m. The maximum adiabatic temperature of an EC material is obtained as 5.41 K at 100 MV/m by square with sudden increment & decrement electric pulse. The operating temperature also varied from 293.15 K to 373.15 K for ECE estimation. The electrode material thickness ranges from 0.01 to 10 μm for various materials (Au, Ag, Al, Cu, Ti, Ni, Pd, CNT) are considered for ECE analysis. Similarly, the substrate material Al, Brass, Steel, PET, and PDMS thickness varied from 10 to 500 μm for ECE analysis. The optimal working temperature, electrode, and substrate materials are 293.15 K, Au (0.1 μm), and Al (100 μm. The thermal contact (ΔT_{tc}) loss between various layers is found to be 0.66 K, or approximately 13.5% of the total $\Delta T_{ad} = 4.91$ K, equivalent to the ΔT_{tc} obtained experimentally. Lastly, the smartphone battery's surface area of 7 cm × 3 cm is considered for cooling to see the effectiveness of the EC device. The same smartphone battery is regarded as a power source for applying electric potential using a booster circuit, which enhances the practical applicability of the EC device. The battery/source surface was cooled by air, with contact of EC device $E = 0$ and with contact of EC device $E = 100$ MV/m from 313.15 K to ~298 K, 297.5 K, and 298.5 K, respectively, within 6.5 seconds. The time required to cool the battery to room temperature increases as the battery/source thickness increases. The proposed simulation study of an EC device can

overcome issues of battery overheating and increased life, and it can also be used for wearable gadgets, microelectronics circuits, and other appliances.

6.2 Limitation/assumption behind the proposed simulation work

- The assumption is made that the EC device only comes into contact with the battery source when it is overheated, and the EC device is withdrawn when it reaches room temperature. Whenever the battery overheats, the EC device comes into contact with it. So, taking these factors into account, the current study was conducted.

- All sides except the top layer are assumed to be insulated, and the heat will only be released from the top layer.

- The heat transfer is assumed to be only through conduction.

- To simplify the simulation, the present work assumed that 5% of losses occur due to hysteresis ($\Delta T_{hys} = 5\%$) in the reported EC ΔT_{ad}.

- The present analysis does not consider the phase transition in the materials at a given temperature.

- In EC devices, the electrocaloric material is a thin film only, which is ideal where space is constrained and can quickly dissipate heat.

6.3 Future Outlook

Increasing the isothermal heat and adiabatic temperature change over a broad temperature range under a relatively small electric field is the main obstacle to constructing a successful solid-state cooling system. Moreover, EC materials with improved mechanical, thermal, and functional fatigue resistance are needed for real-time device applications. Further, the scalability and adaptability of EC materials suggest broad integration possibilities, facilitating energy-efficient solutions across various devices. Creating thermal diodes or heat switches for quick and effective heat transfer is also crucial. Solid-state cascade structures use a separate design and have long lagged behind technological advances, mainly in solving the problems of parasitic heat loss and multi-body anti-phase ECE/activation synchronization. In essence, the future trajectory of the ECE promises a paradigm shift in thermal management practices and cooling system design. Hence, research must now be directed and expanded to include:

1. Optimization of engineering design-for example, efficient and reliable thermal switching from source to sink under each cycle-is needed.

2. Optimization of materials into prototype devices should be explored.

3. Cascade devices designed with high-temperature range and good energy efficiency

4. Various losses need to be considered during any device design

5. Desirable characteristics of effective and efficient materials are:

(i) Large adiabatic temperature and entropy change with small input electric field requirement

(ii) Improved mechanical, thermal and functional fatigue resistance of EC material

(iii) Operational temperature-independent caloric behavior

(iv) Small interfacial resistance

References

1. Cline, W.R. (1992), The economics of global warming, Institute for International Economics, Washington, DC, 399.
2. Correia, T. and Q. Zhang, 2013, *Electrocaloric Materials: New Generation of Coolers*, in *Electrocaloric Materials: New Generation of Coolers*, Springer, p. 1-15.
3. Vortec, 2014, https://www.vortec.com/en-us/electronic-equipment-failures-cause-effect-and-resolution, *Electrocnics equipment failures: cause, effect and resolution*.
4. Li, X., S.-G. Lu, X.-Z. Chen, H. Gu, X.-s. Qian and Q. Zhang (2013), Pyroelectric and electrocaloric materials, Journal of Materials Chemistry C, 1(1), 23-37.
5. Mali, V., R. Saxena, K. Kumar, A. Kalam and B. Tripathi (2021), Review on battery thermal management systems for energy-efficient electric vehicles, Renewable and Sustainable Energy Reviews, 151 (111611.
6. Dilshad, S., A.R. Kalair and N. Khan (2020), Review of carbon dioxide (CO_2) based heating and cooling technologies: Past, present, and future outlook, International Journal of Energy Research, 44(3), 1408-1463.
7. Phan, M.-H. and S.-C. Yu (2007), Review of the magnetocaloric effect in manganite materials, Journal of Magnetism and Magnetic Materials, 308(2), 325-340.
8. Valant, M. (2012), Electrocaloric materials for future solid-state refrigeration technologies, Progress in Materials Science, 57(6), 980-1009.
9. Ma, R., Z. Zhang, K. Tong, D. Huber, R. Kornbluh, Y.S. Ju and Q. Pei (2017), Highly efficient electrocaloric cooling with electrostatic actuation, Science, 357(6356), 1130-1134.
10. Liu, Y., J.F. Scott and B. Dkhil (2016), Direct and indirect measurements on electrocaloric effect: Recent developments and perspectives, Applied Physics Reviews, 3(3), 031102.
11. Brown, J.S. and P.A. Domanski (2014), Review of alternative cooling technologies, Applied Thermal Engineering, 64(1-2), 252-262.
12. Moya, X., S. Kar-Narayan and N.D. Mathur (2014), Caloric materials near ferroic phase transitions, Nature materials, 13(5), 439-450.
13. Zhao, D. and G. Tan (2014), A review of thermoelectric cooling: Materials, modeling and applications, Applied thermal engineering, 66(1-2), 15-24.
14. Ossmer, H., F. Wendler, M. Gueltig, F. Lambrecht, S. Miyazaki and M. Kohl (2016), Energy-efficient miniature-scale heat pumping based on shape memory alloys, Smart Materials and Structures, 25(8), 085037.
15. Tušek, J., K. Engelbrecht, D. Eriksen, S. Dall'Olio, J. Tušek and N. Pryds (2016), A regenerative elastocaloric heat pump, Nature Energy, 1(10), 1-6.
16. Franco, V., J. Blázquez, J. Ipus, J. Law, L. Moreno-Ramírez and A. Conde (2018), Magnetocaloric effect: From materials research to refrigeration devices, Progress in Materials Science, 93(112-232.
17. Li, Q., G. Zhang, X. Zhang, S. Jiang, Y. Zeng and Q. Wang (2015), Relaxor ferroelectric-based electrocaloric polymer nanocomposites with a broad operating temperature range and high cooling energy, Advanced Materials (Deerfield Beach, Fla.), 27(13), 2236-2241.
18. Gutfleisch, O., M.A. Willard, E. Brück, C.H. Chen, S. Sankar and J.P. Liu (2011), Magnetic materials and devices for the 21st century: stronger, lighter, and more energy efficient, Advanced materials, 23(7), 821-842.
19. Fujita, A., S. Fujieda, Y. Hasegawa and K. Fukamichi (2003), Itinerant-electron metamagnetic transition and large magnetocaloric effects in La(Fe$_x$Si$_{1-x}$)$_{13}$ compounds and their hydrides, Physical Review B, 67(10), 104416.

20. Shi, J., D. Han, Z. Li, L. Yang, S.-G. Lu, Z. Zhong, J. Chen, Q. Zhang and X. Qian (2019), Electrocaloric cooling materials and devices for zero-global-warming-potential, high-efficiency refrigeration, Joule, 3(5), 1200-1225.
21. Pakhomov, O., S. Karmanenko, A. Semenov, A. Starkov and A. Es' kov (2010), Thermodynamic estimation of cooling efficiency using an electrocaloric solid-state line, Technical Physics, 55(1155-1160.
22. Zimm, C., A. Jastrab, A. Sternberg, V. Pecharsky, K. Gschneidner, M. Osborne and I. Anderson (1998), Description and performance of a near-room temperature magnetic refrigerator, Advances in cryogenic engineering, 1759-1766.
23. Kumar, A., A. Thakre, D.-Y. Jeong and J. Ryu (2019), Prospects and challenges of the electrocaloric phenomenon in ferroelectric ceramics, Journal of Materials Chemistry C, 7(23), 6836-6859.
24. Meng, Y., Z. Zhang, H. Wu, R. Wu, J. Wu, H. Wang and Q. Pei (2020), A cascade electrocaloric cooling device for large temperature lift, Nature Energy, 5(12), 996-1002.
25. Scott, J. (2011), Electrocaloric materials, Annual Review of Materials Research, 41(229-240.
26. Kutnjak, Z., B. Rožič and R. Pirc (1999), Electrocaloric effect: theory, measurements, and applications, Wiley encyclopedia of electrical and electronics engineering, 1-19.
27. Mischenko, A., Q. Zhang, J. Scott, R. Whatmore and N. Mathur (2006), Giant electrocaloric effect in thin-film $PbZr_{0.95}Ti_{0.05}O_3$, Science, 311(5765), 1270-1271.
28. Greco, A. and C. Masselli (2020), Electrocaloric cooling: A review of the thermodynamic cycles, materials, models, and devices, Magnetochemistry, 6(4), 67.
29. Schwartz, D.E. (2021), Thermodynamic cycles and electrical charge recovery in high-efficiency electrocaloric cooling systems, International Journal of Refrigeration, 131(970-979.
30. Zhang, J., X. Hou, Y. Zhang, G. Tang and J. Wang (2021), Electrocaloric effect in ferroelectric materials: From phase field to first-principles based effective Hamiltonian modeling, Materials Reports: Energy, 1(3), 100050.
31. Correia, T., S. Kar-Narayan, J. Young, J. Scott, N. Mathur, R.W. Whatmore and Q. Zhang (2011), PST thin films for electrocaloric coolers, Journal of Physics D: Applied Physics, 44(16), 165407.
32. Neese, B., B. Chu, S.-G. Lu, Y. Wang, E. Furman and Q. Zhang (2008), Large electrocaloric effect in ferroelectric polymers near room temperature, Science, 321(5890), 821-823.
33. Lines, M.E. and A.M. Glass, 2001, *Principles and applications of ferroelectrics and related materials*, Oxford university press.
34. Valasek, J. (1921), Piezo-electric and allied phenomena in Rochelle salt, Physical review, 17(4), 475.
35. Valasek, J. (1927), Note on the piezo-electric effect in Rochelle salt crystals, Science, 65(1679), 235-236.
36. Bowen, C., H. Kim, P. Weaver and S. Dunn (2014), Piezoelectric and ferroelectric materials and structures for energy harvesting applications, Energy & Environmental Science, 7(1), 25-44.
37. Ožbolt, M., A. Kitanovski, J. Tušek and A. Poredoš (2014), Electrocaloric refrigeration: thermodynamics, state of the art and future perspectives, International journal of refrigeration, 40(174-188.
38. Damjanovic, D. (1998), Ferroelectric, dielectric and piezoelectric properties of ferroelectric thin films and ceramics, Reports on progress in physics, 61(9), 1267.

39. Peláiz-Barranco, A., F. Calderón-Piñar, O. García-Zaldívar and Y. González-Abreu (2012), Relaxor behaviour in ferroelectric ceramics, Advances in Ferroelectrics, 85-107.

40. Jin, L., F. Li and S. Zhang (2014), Decoding the fingerprint of ferroelectric loops: comprehension of the material properties and structures, Journal of the American Ceramic Society, 97(1), 1-27.

41. Ožbolt, M., A. Kitanovski, J. Tušek and A. Poredoš (2014), Electrocaloric vs. magnetocaloric energy conversion, International journal of refrigeration, 37(16-27.

42. Qian, X.S., H.J. Ye, Y.T. Zhang, H. Gu, X. Li, C. Randall and Q. Zhang (2014), Giant electrocaloric response over a broad temperature range in modified $BaTiO_3$ ceramics, Advanced Functional Materials, 24(9), 1300-1305.

43. Kobeko, P. and J. Kurtschatov (1930), Dielektrische eigenschaften der seignettesalzkristalle, Zeitschrift für Physik, 66(192-205.

44. Li, X., 2013, Electrocaloric Effect in Relaxor Ferroelectric Materials, PhD Dissertation, The Pennsylvania State University.

45. Sanlialp, M., C. Molin, V.V. Shvartsman, S. Gebhardt and D.C. Lupascu (2016), Modified differential scanning calorimeter for direct electrocaloric measurements, IEEE transactions on ultrasonics, ferroelectrics, and frequency control, 63(10), 1690-1696.

46. Mischenko, A., Q. Zhang, R.W. Whatmore, J. Scott and N. Mathur (2006), Giant electrocaloric effect in the thin film relaxor ferroelectric $0.9PbMg_{1/3}Nb_{2/3}O_{3-0.1}PbTiO_3$ near room temperature, Applied Physics Letters, 89(24), 242912.

47. Plaznik, U., A. Kitanovski, B. Rožič, B. Malič, H. Uršič, S. Drnovšek, J. Cilenšek, M. Vrabelj, A. Poredoš and Z. Kutnjak (2015), Bulk relaxor ferroelectric ceramics as a working body for an electrocaloric cooling device, Applied physics letters, 106(4), 043903.

48. Hegenbarth, E. (1961), Studies of the electrocaloric effect of ferroelectricceramics at low temperatures, Cryogenics, 1(4), 242-243.

49. Chukka, R., J.W. Cheah, Z. Chen, P. Yang, S. Shannigrahi, J. Wang and L. Chen (2011), Enhanced cooling capacities of ferroelectric materials at morphotropic phase boundaries, Applied Physics Letters, 98(24), 242902.

50. Sternberg, A., L. Shebanovs, V. Zauls and K. Kundzins (2003), Ceramics and Thin Films of Some New Pb $(B^{3+},Nb)TiO_3$-$PbTiO_3$ Systems, Ferroelectrics, 286(1), 327-334.

51. Starkov, I.A., A.S. Anokhin and A.S. Starkov (2020), Pulse shape effects in electrocaloric cooling, IEEE Transactions on Ultrasonics, Ferroelectrics, and Frequency Control, 68(3), 865-871.

52. Jian, X.-D., B. Lu, D.-D. Li, Y.-B. Yao, T. Tao, B. Liang, J.-H. Guo, Y.-J. Zeng, J.-L. Chen and S.-G. Lu (2018), Direct Measurement of Large Electrocaloric Effect in $Ba(Zr_xTi_{1-x})O_3$ Ceramics, ACS applied materials & interfaces, 10(5), 4801-4807.

53. Thacher, P. (1968), Electrocaloric effects in some ferroelectric and antiferroelectric $Pb(Zr,Ti)O_3$ compounds, Journal of applied physics, 39(4), 1996-2002.

54. Tuttle, B. and D. Payne (1981), The effects of microstructure on the electrocaloric properties of $Pb(Zr,Sn,Ti)O_3$ ceramics, Ferroelectrics, 37(1), 603-606.

55. Rožič, B., B. Malič, H. Uršič, J. Holc, M. Kosec and Z. Kutnjak (2011), Direct measurements of the electrocaloric effect in bulk $PbMg_{1/3}Nb_{2/3}O_3$ (PMN) ceramics, Ferroelectrics, 421(1), 103-107.

56. Rožič, B., B. Malič, H. Uršič, J. Holc, M. Kosec, B. Neese, Q. Zhang and Z. Kutnjak (2010), Direct measurements of the giant electrocaloric effect in soft and solid ferroelectric materials, Ferroelectrics, 405(1), 26-31.

57. Wang, J., T. Yang, K. Wei and X. Yao (2013), Temperature-electric field hysteresis loop of electrocaloric effect in ferroelectricity-Direct measurement and analysis of electrocaloric effect., Applied Physics Letters, 102(15), 152907.

58. Bai, Y., G.-P. Zheng and S.-Q. Shi (2011), Abnormal electrocaloric effect of $Na_{0.5}Bi_{0.5}TiO_3$–$BaTiO_3$ lead-free ferroelectric ceramics above room temperature, Materials Research Bulletin, 46(11), 1866-1869.

59. Lu, S., B. Rožič, Q. Zhang, Z. Kutnjak, R. Pirc, M. Lin, X. Li and L. Gorny (2010), Comparison of directly and indirectly measured electrocaloric effect in relaxor ferroelectric polymers, Applied Physics Letters, 97(20), 202901.

60. Neese, B., S. Lu, B. Chu and Q. Zhang (2009), Electrocaloric effect of the relaxor ferroelectric poly (vinylidene fluoride-trifluoroethylene-chlorofluoroethylene) terpolymer, Applied Physics Letters, 94(4), 042910.

61. Ramana, E.V., N.M. Ferreira, A. Mahajan, D.M. Tobaldi, I. Bdikin, B. Rožič, Z. Kutnjak and M.A. Valente (2021), Processing mediated enhancement of ferroelectric and electrocaloric properties in $Ba(Ti_{0.8}Zr_{0.2})O_3$–$(Ba_{0.7}Ca_{0.3})TiO_3$ lead-free piezoelectrics, Journal of the European ceramic society, 41(13), 6424-6440.

62. Rožič, B., Z. Kutnjak, B. Neese, S.-G. Lu and Q. Zhang (2010), Electrocaloric effect in the relaxor ferroelectric polymer composition $P(VDF–TrFE–CFE)_{0.90}$–$P(VDF–CTFE)_{0.10}$, Phase Transitions, 83(10-11), 819-823.

63. Hagberg, J., A. Uusimäki and H. Jantunen (2008), Electrocaloric characteristics in reactive sintered $0.87Pb(Mg_{1/3}Nb_{2/3})O_3$-$0.13PbTiO_3$, Applied Physics Letters, 92(13), 132909.

64. Saranya, D., A.R. Chaudhuri, J. Parui and S. Krupanidhi (2009), Electrocaloric effect of PMN-PT thin films near morphotropic phase boundary, Bulletin of Materials Science, 32(259-262.

65. Qian, X.S., S.G. Lu, X. Li, H. Gu, L.C. Chien and Q. Zhang (2013), Large electrocaloric effect in a dielectric liquid possessing a large dielectric anisotropy near the isotropic–nematic transition, Advanced Functional Materials, 23(22), 2894-2898.

66. Lawless, W. (1977), Specific heat and electrocaloric properties of $KTaO_3$ at low temperatures, Physical Review B, 16(1), 433.

67. Zhao, Y., J. Du, J. Yang, L. Zhu, Y. Wang, Y. Li and X. Hao (2022), Large room-temperature electrocaloric response realized in potassium-sodium niobate by a relaxor enhancement effect and multilayer ceramic construct, ACS Applied Materials & Interfaces, 14(9), 11626-11635.

68. Bradeško, A., L. Fulanović, M. Vrabelj, A. Matavž, M. Otoničar, J. Koruza, B. Malič and T. Rojac (2021), Multifunctional Cantilevers as Working Elements in Solid-State Cooling Devices, Actuators, 10(3), 58.

69. Bai, Y., G. Zheng and S. Shi (2010), Direct measurement of giant electrocaloric effect in $BaTiO_3$ multilayer thick film structure beyond theoretical prediction, Applied Physics Letters, 96(19),

70. Bai, Y., G.-P. Zheng, K. Ding, L. Qiao, S.-Q. Shi and D. Guo (2011), The giant electrocaloric effect and high effective cooling power near room temperature for $BaTiO_3$ thick film, Journal of applied physics, 110(9), 094103.

71. Nouchokgwe, Y., P. Lheritier, C.-H. Hong, A. Torelló, R. Faye, W. Jo, C.R. Bahl and E. Defay (2021), Giant electrocaloric materials energy efficiency in highly ordered lead scandium tantalate, Nature communications, 12(1), 3298.

72. Nair, B., T. Usui, S. Crossley, S. Kurdi, G. Guzmán-Verri, X. Moya, S. Hirose and N. Mathur (2019), Large electrocaloric effects in oxide multilayer capacitors over a wide temperature range, Nature, 575(7783), 468-472.

73. Koruza, J., H. Liu, M. Höfling, M.-H. Zhang and P. Veber (2020), (K, Na)NbO$_3$-based piezoelectric single crystals: Growth methods, properties, and applications, Journal of Materials Research, 35(8), 990-1016.

74. Costa, C.M., V.F. Cardoso, P. Martins, D.M. Correia, R. Gonçalves, P. Costa, V. Correia, C. Ribeiro, M.M. Fernandes and P.M. Martins (2023), Smart and multifunctional materials based on electroactive poly (vinylidene fluoride): Recent advances and opportunities in sensors, actuators, energy, environmental, and biomedical applications, Chemical reviews, 123(19), 11392-11487.

75. Qian, X., S. Wu, E. Furman, Q. Zhang and J. Su (2015), Ferroelectric polymers as multifunctional electroactive materials: recent advances, potential, and challenges, MRS communications, 5(2), 115-129.

76. Bae, J.-H. and S.-H. Chang (2019), PVDF-based ferroelectric polymers and dielectric elastomers for sensor and actuator applications: a review, Functional Composites and Structures, 1(1), 012003.

77. Ducharme, S. (2009), An inside-out approach to storing electrostatic energy, ACS nano, 3(9), 2447-2450.

78. Chu, B., X. Zhou, K. Ren, B. Neese, M. Lin, Q. Wang, F. Bauer and Q. Zhang (2006), A dielectric polymer with high electric energy density and fast discharge speed, Science, 313(5785), 334-336.

79. Chang, C., V.H. Tran, J. Wang, Y.-K. Fuh and L. Lin (2010), Direct-write piezoelectric polymeric nanogenerator with high energy conversion efficiency, Nano letters, 10(2), 726-731.

80. Voet, V.S., D. Hermida-Merino, G. ten Brinke and K. Loos (2013), Block copolymer route towards poly (vinylidene fluoride)/poly (methacrylic acid)/nickel nanocomposites, RSC advances, 3(21), 7938-7946.

81. Lu, S.-G., B. Rožič, Q. Zhang, Z. Kutnjak and B. Neese (2011), Enhanced electrocaloric effect in ferroelectric poly (vinylidene-fluoride/trifluoroethylene) 55/45 mol% copolymer at ferroelectric-paraelectric transition, Applied Physics Letters, 98(12), 122906.

82. Lu, S.G. and Q. Zhang (2009), Electrocaloric materials for solid-state refrigeration, Advanced Materials, 21(19), 1983-1987.

83. Gu, H., X. Qian, X. Li, B. Craven, W. Zhu, A. Cheng, S. Yao and Q. Zhang (2013), A chip scale electrocaloric effect based cooling device, Applied Physics Letters, 102(12), 122904.

84. Bauer, F., E. Fousson and Q. Zhang (2006), Recent advances in highly electrostrictive P(VDF-TrFE-CFE) terpolymers, IEEE Transactions on Dielectrics and Electrical Insulation, 13(5), 1149-1154.

85. Sebald, G., L. Seveyrat, J.-F. Capsal, P.-J. Cottinet and D. Guyomar (2012), Differential scanning calorimeter and infrared imaging for electrocaloric characterization of poly (vinylidene fluoride-trifluoroethylene-chlorofluoroethylene) terpolymer, Applied Physics Letters, 101(2), 022907.

86. Rabadiya, R.A., N. Saurabh and S. Patel (2024), Simulation study on the effect of operating and materials parameters on electrocaloric device for battery cooling, Physica Scripta, 99(4), 045915.

87. Ponomareva, I. and S. Lisenkov (2012), Bridging the macroscopic and atomistic descriptions of the electrocaloric effect, Physical review letters, 108(16), 167604.

88. Rose, M.C. and R.E. Cohen (2012), Giant electrocaloric effect around T_c, Physical review letters, 109(18), 187604.

89. Chen, X. and C. Fang (2013), Study of electrocaloric effect in barium titanate nanoparticle with core–shellmodel, Physica B: Condensed Matter, 415(14-17.

90. Ma, Y.-B., C. Molin, V.V. Shvartsman, S. Gebhardt, D.C. Lupascu, K. Albe and B.-X. Xu (2017), State transition and electrocaloric effect of $BaZr_xTi_{1-x}O_3$: Simulation and experiment, Journal of Applied Physics, 121(2), 024103.

91. Herchig, R., C.-M. Chang, B. Mani and I. Ponomareva (2015), Electrocaloric effect in ferroelectric nanowires from atomistic simulations, Scientific Reports, 5(1), 17294.

92. Zhang, J. (2020), Electrocaloric effects in monolayer germanium sulfide: A study by molecular dynamics simulations and thermodynamic analyses, Journal of Applied Physics, 127(17), 175105.

93. Li, Z., J. Li, H.-H. Wu, J. Li, S. Wang, S. Qin, Y. Su, L. Qiao, D. Guo and Y. Bai (2020), Effect of electric field orientation on ferroelectric phase transition and electrocaloric effect, Acta Materialia, 191(13-23.

94. Abdullahi Hassan, Y., L. Chen, X. Geng, Z. Jiang, F. Zhang, S. Luo and H. Hu (2021), Electrocaloric Effect of Structural Configurated Ferroelectric Polymer Nanocomposites for Solid-State Refrigeration, ACS Applied Materials & Interfaces, 13(39), 46681-46693.

95. Uršič, H., M. Hrovat, J. Holc, M. Santo Zarnik, S. Drnovšek, S. Maček and M. Kosec (2008), A large-displacement $65Pb(Mg_{1/3}Nb_{2/3})O_3–35PbTiO_3$/Pt bimorph actuator prepared by screen printing, Sensors and Actuators B: Chemical, 133(2), 699-704.

96. Rožič, B., H. Uršič, J. Holc, M. Kosec and Z. Kutnjak (2012), Direct measurements of the electrocaloric effect in substrate-free PMN-0.35PT thick films on a platinum layer, Integrated Ferroelectrics, 140(1), 161-165.

97. Guo, D., J. Gao, Y.-J. Yu, S. Santhanam, A. Slippey, G.K. Fedder, A.J. McGaughey and S.-C. Yao (2014), Design and modeling of a fluid-based micro-scale electrocaloric refrigeration system, International Journal of Heat and Mass Transfer, 72(559-564.

98. Akcay, G., S. Alpay, G. Rossetti and J. Scott (2008), Influence of mechanical boundary conditions on the electrocaloric properties of ferroelectric thin films, Journal of Applied Physics, 103(2), 024104.

99. Cui, H., W. He, Q. Pei and R. Ma (2022), Electrocaloric effects in ferroelectric polymers, Organic Ferroelectric Materials and Applications, 535-570.

100. Dos Santos, W., C. Iguchi and R. Gregorio Jr (2008), Thermal properties of poly (vinilidene fluoride) in the temperature range from 25 to 210°C, Polymer testing, 27(2), 204-208.

101. Gu, H. (2014), Chip-scale cooling devices based on electrocaloric effect, PhD Dissertation on Chip-scale cooling devices based on electrocaloric effect in Pennsylvania State University, The Graduate School College of Engineering,

102. Chen, X., S. Li, X. Jian, Y. Hambal, S.-G. Lu, V.V. Shvartsman, D.C. Lupascu and Q. Zhang (2021), Maxwell relation, giant (negative) electrocaloric effect, and polarization hysteresis, Applied Physics Letters, 118(12), 122904.

103. Xu, H., J. Zhong, X. Liu, J. Chen and D. Shen (2007), Ferroelectric and switching behavior of poly (vinylidene fluoride-trifluoroethylene) copolymer ultrathin films with polypyrrole interface, Applied Physics Letters, 90(9), 092903.

104. Bharadwaja, S., M. Olszta, S. Trolier-McKinstry, X. Li, T. Mayer and F. Roozeboom (2006), Fabrication of high aspect ratio ferroelectric microtubes by vacuum infiltration using macroporous silicon templates, Journal of the American Ceramic Society, 89(9), 2695-2701.

105. Viehland, D. and J. Li (2001), Investigations of electrostrictive $Pb(Mg_{1/3}Nb_{2/3})O_3–PbTiO_3$ ceramics under high-power drive conditions: Importance of compositional fluctuations on residual hysteresis, Journal of Applied Physics, 89(3), 1826-1835.

106. Rajagopal, M.C., T. Man, A. Agrawal, G. Kuntumalla and S. Sinha (2020), Intrinsic thermal interfacial resistance measurement in bonded metal–polymer foils, Review of Scientific Instruments, 91(10), 104901.

107. Chen, Z., W. Jang, W. Bao, C. Lau and C. Dames (2009), Thermal contact resistance between graphene and silicon dioxide, Applied Physics Letters, 95(16), 161910.

108. Koh, Y.K., M.-H. Bae, D.G. Cahill and E. Pop (2010), Heat conduction across monolayer and few-layer graphenes, Nano letters, 10(11), 4363-4368.

109. Feng, X., C. King and S. Narumanchi (2016), General multilayer heat transfer model for optical-based thermal characterization techniques, International Journal of Heat and Mass Transfer, 93(695-706.

110. Chen, J., W. Zhang, Z. Feng and W. Cai (2014), Determination of thermal contact conductance between thin metal sheets of battery tabs, International Journal of Heat and Mass Transfer, 69(473-480.

111. López, C., E. Ramos, M. Muñoz, S. Kar-Narayan, N. Mathur and J.L. Prieto (2017), Influence of the thermal contact resistance in current-induced domain wall depinning, Journal of Physics D: Applied Physics, 50(32), 325001.

112. Sebald, G., E. Lefeuvre and D. Guyomar (2008), Pyroelectric energy conversion: optimization principles, IEEE transactions on ultrasonics, ferroelectrics, and frequency control, 55(3), 538-551.

113. Kwon, B., I.-J. Roh, S.-H. Baek, S. Keun Kim, J.-S. Kim and C.-Y. Kang (2014), Dynamic temperature response of electrocaloric multilayer capacitors, Applied Physics Letters, 104(21), 213902.

114. Qian, X., D. Han, L. Zheng, J. Chen, M. Tyagi, Q. Li, F. Du, S. Zheng, X. Huang and S. Zhang (2021), High-entropy polymer produces a giant electrocaloric effect at low fields, Nature, 600(7890), 664-669.

115. M'nassri, R., M.M. Nofal, E.M. Dannoun and H. Rahmouni (2022), Analysis of the electric field dependence on the electrocaloric properties on $BaHf_{0.11}Ti_{0.89}O_3$ ferroelectric ceramics, Applied Physics A, 128(11), 997.

116. Patel, S., P. Sharma and R. Vaish (2016), Enhanced electrocaloric effect in $Ba_{0.85}Ca_{0.15}Zr_{0.1}Ti_{0.9-x}Sn_xO_3$ ferroelectric ceramics, Phase Transitions, 89(11), 1062-1073.

117. Ali, F., A. Abbas, G. Wu, M. Daaim, A. Akhtar, K.H. Kim and B. Yang (2022), Novel Fluorite-Structured Materials for Solid-State Refrigeration, Small, 18(23), 2200133.

118. Cheng, X., F. Weyland, N. Novak and Y. Li (2019), Indirect electrocaloric evaluation: Influence of polarization hysteresis measurement frequency, physica status solidi (a), 216(24), 1900684.

119. Li, Z., H.-H. Wu, J. Li, S. Wang, S. Qin, J. He, C. Liu, Y. Su, L. Qiao and T. Lookman (2022), Effects of thermal and electrical hysteresis on phase transitions and electrocaloric effect in ferroelectrics: A computational study, Acta Materialia, 228(117784.

120. Aravindhan, A., P. Lheritier, A. Torelló, U. Prah, Y. Nouchokgwe, A. El Moul, X. Chevalier, F.D. Dos Santos, E. Defay and V. Kovacova (2023), Direct measurement of electrocaloric effect in P(VDF-TrFE-CFE) film using infrared imaging, Journal of Materiomics, 9(2), 256-260.

121. Shehzad, M. and T. Malik (2018), Antiferroelectric behavior of P(VDF-TrFE) and P(VDF-TrFE-CTFE) ferroelectric domains for energy harvesting, ACS Applied Energy Materials, 1(6), 2832-2840.

122. Chen, Q., K. Ren, B. Chu, Y. Liu, Q. Zhang, V. Bobnar and A. Levstik (2007), Relaxor ferroelectric polymers–fundamentals and applications, Ferroelectrics, 354(1), 178-191.

123. Basso, V., F. Russo, J.-F. Gerard and S. Pruvost (2013), Direct measurement of the electrocaloric effect in poly(vinylidene fluoride-trifluoroethylene-chlorotrifluoroethylene) terpolymer films, Applied Physics Letters, 103(20), 202904.

124. Guo, D., J. Gao, Y.-J. Yu, S. Santhanam, G.K. Fedder, A.J. McGaughey and S. Yao (2014), Electrocaloric characterization of a poly (vinylidene fluoride-trifluoroethylene-chlorofluoroethylene) terpolymer by infrared imaging, Applied Physics Letters, 105(3), 031906.

125. Kovacova, V., S. Glinsek, S. Girod and E. Defay (2022), High Electrocaloric Effect in Lead Scandium Tantalate Thin Films with Interdigitated Electrodes, Sensors, 22(11), 4049.

126. Marathe, M., D. Renggli, M. Sanlialp, M.O. Karabasov, V.V. Shvartsman, D.C. Lupascu, A. Grünebohm and C. Ederer (2017), Electrocaloric effect in $BaTiO_3$ at all three ferroelectric transitions: Anisotropy and inverse caloric effects, Physical Review B, 96(1), 014102.

127. Faye, R., T. Usui, A. Torello, B. Dkhil, X. Moya, N.D. Mathur, S. Hirose and E. Defay (2020), Heat flow in electrocaloric multilayer capacitors, Journal of Alloys and Compounds, 834(155042.

128. Cao, H.-X. and Z.-Y. Li (2009), Electrocaloric effect in $BaTiO_3$ thin films, Journal of Applied Physics, 106(9), 094104.

129. Zuo, Z., B. Chen, B. Wang, H. Yang, Q. Zhan, Y. Liu, J. Wang and R.-W. Li (2015), Strain assisted electrocaloric effect in $PbZr_{0.95}Ti_{0.05}O_3$ films on $0.7Pb(Mg_{1/3}Nb_{2/3})O_{3-0.3}PbTiO_3$ substrate, Scientific Reports, 5(1), 16164.

130. Chen, J., B. Peng and W. Sun (2022), Pure negative electrocaloric effect achieved by SiN/p-GaN composite substrate, Nano Energy, 97(107195.

131. Bradeško, A., Đ. Juričić, M. Santo Zarnik, B. Malič, Z. Kutnjak and T. Rojac (2016), Coupling of the electrocaloric and electromechanical effects for solid-state refrigeration, Applied Physics Letters, 109(14), 143508.

132. Srikanth, K., S. Patel and R. Vaish (2018), Electrocaloric behavior and temperature dependent scaling of dynamic hysteresis of $Ba_xSr_{1-x}TiO_3$ (x= 0.7, 0.8 and 0.9) bulk ceramics, Journal of the Australian Ceramic Society, 54(439-450.

133. Qiu, J. and Q. Jiang (2008), Effect of electric field on electrocaloric effect in $Pb(Zr_{1-x}Ti_x)O_3$ solid solution, Physics Letters A, 372(48), 7191-7195.

134. Patel, S., A. Chauhan and R. Vaish (2016), Large room temperature electrocaloric strength in bulk ferroelectric ceramics: an optimum solution, Phase Transitions, 89(10), 1019-1028.

135. Wu, H.-H., J. Zhu and T.-Y. Zhang (2015), Pseudo-first-order phase transition for ultrahigh positive/negative electrocaloric effects in perovskite ferroelectrics, Nano Energy, 16(419-427.

136. Zhao, Y., X. Hao and Q. Zhang (2014), Energy-Storage Properties and Electrocaloric Effect of $Pb_{(1-3x/2)}La_xZr_{0.85}Ti_{0.15}O_3$ Antiferroelectric Thick Films, ACS applied materials & interfaces, 6(14), 11633-11639.

137. Ju, Y.S. (2010), Solid-state refrigeration based on the electrocaloric effect for electronics cooling, Journal of Electronic Packaging, 132(4), 041004.

138. Kar-Narayan, S. and N. Mathur (2009), Predicted cooling powers for multilayer capacitors based on various electrocaloric and electrode materials, Applied Physics Letters, 95(24), 242903.

139. Zhao, Y., S.-H. Li, J. Chu, Y.-P. Chen, W.-W. Li, H.-Q. Yu, G. Liu, Y.-C. Tian and Y. Xiong (2012), A nano-sized Au electrode fabricated using lithographic technology for electrochemical detection of dopamine, Biosensors and Bioelectronics, 35(1), 115-122.

140. Goodman, P. (2002), Current and future uses of gold in electronics, Gold bulletin, 35(21-26.

141. Bennett, T.D., C.P. Grigoropoulos and D.J. Krajnovich (1995), Near-threshold laser sputtering of gold, Journal of applied physics, 77(2), 849-864.

142. Thomson, R. and J. Moreland (1995), Development of highly conductive cantilevers for atomic force microscopy point contact measurements, Journal of Vacuum Science & Technology B: Microelectronics and Nanometer Structures Processing, Measurement, and Phenomena, 13(3), 1123-1125.

143. Skorjanc, T., D. Shetty and M. Valant (2021), Covalent organic polymers and frameworks for fluorescence-based sensors, ACS sensors, 6(4), 1461-1481.

144. Liu, H. (2020), Electrocaloric effect enhanced thermal conduction of a multilayer ceramic structure, Chinese Physics B, 29(8), 087701.

145. Bäckman, P., M. Bastos, D. Hallén, P. Lönnbro and I. Wadsö (1994), Heat conduction calorimeters: time constants, sensitivity and fast titration experiments, Journal of biochemical and biophysical methods, 28(2), 85-100.

146. Waheed, S., J.M. Cabot, N.P. Macdonald, U. Kalsoom, S. Farajikhah, P.C. Innis, P.N. Nesterenko, T.W. Lewis, M.C. Breadmore and B. Paull (2017), Enhanced physicochemical properties of polydimethylsiloxane based microfluidic devices and thin films by incorporating synthetic micro-diamond, Scientific Reports, 7(1), 15109.

147. Mikić, B. (1974), Thermal contact conductance; theoretical considerations, International journal of heat and mass transfer, 17(2), 205-214.

148. Bahrami, M., M. Yovanovich and E. Marotta (2006), Thermal joint resistance of polymer-metal rough interfaces, Journal of electronic Packaging, 128(1), 23-29.

149. Salam, M.A.-E., G. Elkomy, H. Osman, M. Nagy and F. El-Sayed (2012), Structure–electrical conductivity of polyvinylidene fluoride/graphite composites, Journal of Reinforced Plastics and Composites, 31(20), 1342-1352.

150. Puértolas, J., J. García-García, F.J. Pascual, J.M. González-Domínguez, M. Martínez and A. Ansón-Casaos (2017), Dielectric behavior and electrical conductivity of PVDF filled with functionalized single-walled carbon nanotubes, Composites Science and Technology, 152(263-274.

151. Bajpai, R., V. Mishra and S. Datt (1992), Microhardness measurements of poly (methyl methacrylate) and poly (vinylidene fluoride) polyblends, Polymer testing, 11(5), 387-391.

152. Kang, X., S. Jia, J. Peng, H. Yu and X. Zhou (2021), Electromagnetic-driven electrocaloric cooling device based on ternary ferroelectric composites, Composites Part B: Engineering, 227(109391.

153. Cazorla, C. (2019), Novel mechanocaloric materials for solid-state cooling applications, Applied Physics Reviews, 6(4), 041316.

154. Lu, Y., X. Sun, M. Zhao, S. Jiao, D. Li, P. Chen, W. Zhang, K. Ye, L. Xu and Q. You (2023), Enhanced Electrocaloric Effect of Lead Scandium Tantalate by Zirconium Doping, ACS Applied Materials & Interfaces, 15(44), 51252-51261.

155. Wang, H., Y. Meng, Z. Zhang, M. Gao, Z. Peng, H. He and Q. Pei (2020), Self-Actuating Electrocaloric Cooling Fibers, Advanced Energy Materials, 10(12), 1903902.

156. Molin, C., P. Neumeister, H. Neubert and S.E. Gebhardt (2018), Multilayer ceramics for electrocaloric cooling applications, Energy Technology, 6(8), 1543-1552.